

การจำลองโมเดลเชิงคำนวณโหนดคอมพิวเตอร์ไร้สายสำหรับเซลล์
แสงอาทิตย์แบบไวต่อสีอ่อน: ระบบพอลิเอทิลีนออกไซด์/
โพลีเอทิลีนไอกไซด์/โพลีเอทิลีนออกไซด์

นางสาวพรทิพย์ สี่มา

วิทยานิพนธ์นี้เป็นส่วนหนึ่งของการศึกษาตามหลักสูตรปริญญาวิทยาศาสตรมหาบัณฑิต
สาขาวิชาเคมี
มหาวิทยาลัยเทคโนโลยีสุรนารี
ปีการศึกษา 2551

**COMPUTATIONAL MOLECULAR MODELING OF
NANOCOMPOSITE ELECTROLYTES FOR DYE-
SENSITIZED SOLAR CELLS: POLY(ETHYLENE
OXIDE)/POTASSIUM IODIDE/TITANIUM
DIOXIDE SYSTEMS**

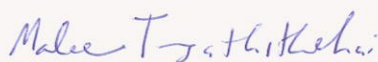
Porntip Seema

**A Thesis Submitted in Partial Fulfillment of the Requirements for
the Degree of Master of Science in Chemistry
Suranaree University of Technology
Academic Year 2008**

**COMPUTATIONAL MOLECULAR MODELING OF
NANOCOMPOSITE ELECTROLYTES FOR DYE-SENSITIZED
SOLAR CELLS: POLY(ETHYLENE OXIDE)/POTASSIUM
IODIDE/TITANIUM DIOXIDE SYSTEMS**

Suranaree University of Technology has approved this thesis submitted in partial fulfillment of the requirements for a Master's Degree.

Thesis Examining Committee



(Assoc. Prof. Dr. Malee Tangsathitkulchai)

Chairperson



(Asst. Prof. Dr. Visit Vao-Soongnern)

Member (Thesis Advisor)



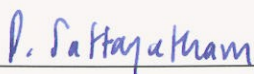
(Assoc. Prof. Dr. Jatuporn Wittayakun)

Member



(Assoc. Prof. Dr. Anan Tongraar)

Member



(Prof. Dr. Pairote Sattayatham)

Vice Rector for Academic Affairs



(Assoc. Prof. Dr. Prapan Manyum)

Dean of Institute of Science

พรทิพย์ สีม่า : การจำลองโมเลกุลเชิงคำนวณนาโนคอมโพสิตอเล็กโทรไลต์สำหรับเซลล์
แสงอาทิตย์แบบไวต่อสีข้อม: ระบบพอลิเอทรีนออกไซด์/โพแทสเซียมไอโอไดด์/ไทเท-
เนียมไดออกไซด์ (COMPUTATIONAL MOLECULAR MODELING OF
NANOCOMPOSITE ELECTROLYTES FOR DYE-SENSITIZED SOLAR CELLS:
POLY(ETHYLENE OXIDE)/POTASSIUM IODIDE/TITANIUM DIOXIDE
SYSTEMS) อาจารย์ที่ปรึกษา : ผู้ช่วยศาสตราจารย์ ดร.วิสิทธิ์ แวสูงเนิน, 199 หน้า.

วัตถุประสงค์ของงานวิจัยนี้คือการศึกษาผลการเติมเกลือ KI และสารเติมแต่ง TiO_2 ต่อ
สมบัติของพอลิเมอร์อเล็กโทรไลต์แข็ง (SPEs) ที่มี PEO เป็นพอลิเมอร์ตัวกลาง ด้วยเทคนิค
โมเลกูลาร์ไดนามิกส์ (MD) ที่ 300 เคลวินโดยใช้ COMPASS forcefield งานวิจัยนี้เริ่มจากการนำ
เทคนิค MD มาศึกษาโครงสร้างของระบบโพแทสเซียมไอออนและไอโอไดด์ไอออนในน้ำ และ
โพแทสเซียมไอออนใน tetraglyme ($\text{K}^+/\text{H}_2\text{O}$, $\text{I}^-/\text{H}_2\text{O}$ และ $\text{K}^+/\text{tetraglyme}$ ตามลำดับ) ระบบเหล่านี้
เป็นระบบอย่างง่ายของ SPEs พบว่าข้อมูลเชิงโครงสร้างได้แก่ ระยะระหว่างอะตอมและจำนวน
อะตอมที่ล้อมรอบไอออนสอดคล้องกับผลการศึกษาที่มีรายงานไว้แล้ว นอกจากนี้ได้ใช้วิธีของ
อะตอมใน MD (MD trajectories) รวมกับการจำลองการกระเจิงของอิเล็กตรอน (electron scattering
simulation) สร้างสเปกตรัม EXAFS สเปกตรัมที่ได้จาก MD สอดคล้องกับสเปกตรัมที่ได้จากการ
ทดลอง ลำดับต่อไปได้นำเทคนิค MD มาศึกษาระบบ KI/tetraglyme ซึ่งมีอัตราส่วนโมลของ
ออกซิเจนและ K^+ เป็น 10:1 ($\text{EO}:\text{K} = 10:1$) พบว่าการเกิดสารเชิงซ้อนระหว่าง K^+ และออกซิเจนมี
ผลทำให้โมเลกุล tetraglyme มีขนาดเล็กลงและการเคลื่อนที่ของ K^+ ช้ากว่า I^- ลำดับต่อไปได้นำ
เทคนิค MD มาศึกษาระบบ PEO/ TiO_2 และ PEO/KI/ TiO_2 ($\text{EO}:\text{K} = 10:1$) พบว่าอันตรกิริยาแบบ
ดึงดูดระหว่างพื้นผิว TiO_2 และ PEO ทำให้ PEO บริเวณใกล้พื้นผิวหนาแน่นมากกว่าบริเวณ bulk
และบริเวณที่ไม่มีพื้นผิว (free surface) และผลของพื้นผิวต่อความหนาแน่นของ PEO นี้ครอบคลุม
บริเวณจนถึงประมาณ 15 อังสตรอมจากพื้นผิว เนื่องจาก PEO ที่บริเวณพื้นผิวมีความหนาแน่นสูง
และเคลื่อนที่ได้น้อย จึงทำให้ไอออนส่วนใหญ่อยู่บริเวณไกลจากพื้นผิว (มากกว่า 15 อังสตรอมจาก
พื้นผิว) ไอออนที่อยู่ไกลจากพื้นผิวเคลื่อนที่ได้เร็วกว่าไอออนในระบบที่ไม่มี TiO_2 และไอออนที่อยู่
ใกล้พื้นผิว ตามลำดับ

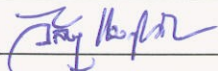
สุดท้ายได้ศึกษาสมบัติเชิงโครงสร้าง สมบัติเชิงพลวัต และกระบวนการเกิดผลึกของระบบ
พอลิเมอร์นาโนคอมโพสิตที่ประกอบด้วย PE ($\text{C}_{40}\text{H}_{82}$) และพื้นผิวแบบเป็นกลาง แบบจุด และแบบ
ผลึก ที่ 473 เคลวิน ด้วยเทคนิค Monte Carlo (MC) โดยใช้ coarse-grained polymer model on a
high coordination lattice จากการศึกษาพบว่าสมบัติเชิงโครงสร้างและสมบัติเชิงพลวัตขึ้นอยู่กับ

อันตรกิริยาระหว่าง PE และพื้นผิว การศึกษากระบวนการเกิดผลึกโดยการลดอุณหภูมิจาก 473 เคลวิน มาที่ 298 เคลวิน ผลที่ได้คือพอลิเมอร์นาโนคอมสิตมีโครงสร้างแบบทรานส์ (*trans* conformation) เพิ่มขึ้นจนถึงค่าคงที่ที่ ~73% สำหรับระบบพื้นผิวแบบจุด และ ~82% สำหรับพื้นผิวแบบกลางและแบบผลึก ซึ่งน้อยกว่าค่าที่คำนวณจากเทคนิคเดียวกันของระบบที่ไม่มีพื้นผิว (~85%)

สาขาวิชาเคมี

ปีการศึกษา 2551

ลายมือชื่อนักศึกษา พรทิพย์ สี่มา

ลายมือชื่ออาจารย์ที่ปรึกษา 

PORNTIP SEEMA : COMPUTATIONAL MOLECULAR MODELING OF NANOCOMPOSITE ELECTROLYTES FOR DYE-SENSITIZED SOLAR CELLS: POLY(ETHYLENE OXIDE)/POTASSIUM IODIDE/TITANIUM DIOXIDE SYSTEMS. THESIS ADVISOR : ASST. PROF. VISIT VAO-SOONGNERN, Ph.D. 199 PP.

MOLECULAR DYNAMICS/MONTE CARLO/NANOCOMPOSITE ELECTROLYTES/PEO/KI/TIO₂

The objective of this research is to study the effect of adding KI salt and TiO₂ nanofiller on the properties of PEO based solid polymer electrolytes (SPEs) by using Molecular Dynamics (MD) simulations with COMPASS forcefield at 300 K. Firstly, the solvation structures of K⁺ and I⁻ in water, and K⁺ in tetraglyme as model complexes for the SPEs were determined. The structural properties *i.e.* pair distances and coordination numbers are in very good agreement with literatures. Moreover, MD trajectories were coupled to electron scattering simulations to generate MD-EXAFS spectra. EXAFS spectra from MD simulations are consistent with those from experiments. Next, MD was performed on KI/tetraglyme system with tetraglyme oxygen:K⁺ mole ratio of 10:1 (EO:K = 10:1). MD results indicated that the complexation between K⁺ and oxygens causes tetraglyme chains become more compact, and K⁺ is slightly slower than I⁻. Next, MD were performed on PEO/TiO₂ and PEO/KI/TiO₂ (EO:K = 10:1) nanocomposites. MD results revealed that an attractive interaction between TiO₂ and PEO results in a highly dense PEO layer near the interface that persists up to ~15 Å from the interface with further than that the

PEO density profile becomes flat and then drops at free surface region. A slow mobility of the highly dense PEO expels most of the ions to the region away from the interface. The mobilities of ions away from the interface are remarkably faster than those in filler-free system and those away from the interface, respectively.

Finally, the structures, dynamics, and crystallization of PE nanocomposites composed of *n*-tetracontane ($C_{40}H_{82}$) mixed with a neutral, attractive and repulsive flat interface were investigated by using Monte Carlo (MC) method of a coarse-grained polymer model on a high coordination lattice at 473 K. The results revealed that the chain structures and dynamics changed according to energetic. For crystallization simulated by quenching the structure from 473 K to 298 K, chains adopt more *trans* conformation, and then the fraction of *trans* approaches a limiting value ~73% for the attractive interface system, and ~82% for the neutral and repulsive interface systems. These values are smaller than the value of the crystallization in the bulk (~85%) by the same MC method.

School of Chemistry

Academic Year 2008

Student's Signature พรทิพย์ สี่มา

Advisor's Signature วิศิต วิชาญ

ACKNOWLEDGMENTS

I am grateful to my thesis advisor, Asst. Prof. Dr. Visit Vao-Soongnern, for his valuable advices, comments for my thesis, for kindness, and suggestions about positive thinking. I am also very thankful for thesis examining committee members for their efforts throughout the entire process. These include Assoc. Prof. Dr. Malee Tangsathitkulchai, Assoc. Prof. Dr. Jatuporn Wittayakun, and Assoc. Prof. Dr. Anan Tongraar. I thank all professors at School of Chemistry, Suranaree University of Technology (SUT) for their kind attitude and providing me valuable knowledge. I would like to pay special thanks to Prof. Dr. Iwao Watanabe at Ritsumeikan University, Kusatsu, Shiga, Japan who gave me a kind suggestion and provided the EXAFS experimental data for iodide anion in aqueous solution.

The gratitude is for all lecturers at Department of Chemistry, Khon Kaen University who gave me valuable advices and knowledge when I did bachelor's degree.

I am thankful to all members in Laboratory of Computational and Applied Polymer Science (LCAPS), and all graduate students at School of Chemistry, SUT for their support, encouragement and made this a fun time. Special thanks for Miss Jittima Chaodumrongsakul who is a kind colleague and provided the EXAFS experimental data for potassium cation in tetraglyme solution.

I would like to thank the Development and Promotion of Science and Technology Talents Project (DPST), and Synchrotron Light Research Institute (Public Organization) for financial support.

Last, but certainly not least, it is my pleasure to thank my beloved family for their support, believe, and encouragement.

Porntip Seema

CONTENTS

	Page
ABSTRACT IN THAI	I
ABSTRACT IN ENGLISH	III
ACKNOWLEDGEMENTS	V
CONTENTS	VII
LIST OF TABLES	XII
LIST OF FIGURES	XIII
LIST OF ABBREVIATIONS	XXI
CHAPTER	
I INTRODUCTION	1
II LITERATURE REVIEW	9
2.1 Dye-Sensitized Solar Cell (DSSC).....	9
2.2 Solid Polymer Electrolytes (SPEs).....	12
2.3 Poly(ethylene oxide), PEO.....	17
2.4 PEO-Salt Electrolytes.....	22
2.5 Enhancement Conductivity of SPEs	25
2.6 PEO-TiO ₂ Nanocomposite for DSSC.....	26
III COMPUTATIONAL MOLECULAR MODELING	31
3.1 Computational Chemistry.....	31
3.2 Molecular Dynamics (MD).....	32

CONTENTS (Continued)

	Page
3.2.1 The Simulation Method	32
3.2.2 Forcefields for MD Simulations.....	36
3.2.3 Periodic Boundary Conditions and Other Requirements.....	38
3.2.4 Structure and Dynamics from MD Simulations.....	41
3.2.5 MD vs. Experiment.....	46
3.3 Monte Carlo (MC).....	47
3.3.1 Computer Simulations for Polymers and Polymer Surfaces....	48
3.3.1.1 Computer Simulations of Polymers	48
3.3.1.2 Computer Simulations of Polymer Surfaces.....	55
3.3.2 Monte Carlo Simulation on a High Coordination Lattice.....	59
3.3.2.1 Coarse Graining into Rotational Isomeric State (RIS) Model.....	60
3.3.2.2 Further Coarse Graining.....	62
3.3.2.3 Conventional RIS Formalism.....	64
3.3.2.4 RIS Formalism for 2nd Chain.....	67
3.3.2.5 Long-range Interactions	69
3.3.2.6 Applications of the Method	72

CONTENTS (Continued)

	Page
IV MOLECULAR SIMULATION ANALYSIS AND X-RAY ABSORPTION MEASUREMENT OF POTASSIUM AND IODIDE IONS IN AQUEOUS SOLUTION AND POTASSIUM ION IN TETRAGLYME SOLUTION	73
4.1 Introduction.....	73
4.2 Background of MD-EXAFS	77
4.3 EXAFS Experimental Details	80
4.4 Computational Details.....	80
4.5 Results and Discussion.....	81
4.5.1 Radial Distribution Functions	81
4.5.2 MD-EXAFS and Experiments	85
4.6 MD-EXAFS Method for K ⁺ /Tetraglyme System.....	92
4.6.1 EXAFS Experimental Details	92
4.6.2 Computational Details.....	92
4.6.3 Results of EXAFS Experiment and MD-EXAFS	93
4.7 Conclusions.....	97

CONTENTS (Continued)

		Page
V	MOLECULAR DYNAMICS SIMULATION OF TETRAGLYME:POTASSIUM IODIDE ELECTROLYTES	99
	5.1 Introduction.....	99
	5.2 Computational Details.....	102
	5.3 Results and Discussion.....	103
	5.3.1 Radial Distribution Functions	103
	5.3.2 Chain Conformation and Dimension	109
	5.3.3 Mean Square Displacement and Diffusion Coefficient	116
	5.4 Conclusions.....	117
VI	MOLECULAR SIMULATIONS OF POLY(ETHYLENE OXIDE)- POTASSIUM IODIDE-TITANIUM DIOXIDE NANOCOMPOSITES.....	118
	6.1 Introduction.....	118
	6.2 MD Simulation Methodology and System Description.....	120
	6.3 Results and Discussion for PEO/TiO ₂ Nanocomposites.....	122
	6.3.1 Structural Properties.....	122
	6.3.2 Interaction Energy.....	124
	6.3.3 Dynamical Properties.....	129
	6.4 Results and Discussion for PEO/KI/TiO ₂ Nanocomposites	130
	6.4.1 Structural Properties.....	130

CONTENTS (Continued)

	Page
6.4.2 Dynamical Properties.....	139
6.5 Monte Carlo Simulations for Polymer Nanocomposites.....	142
6.5.1 Materials and Methods	142
6.5.2 Results and Discussion of Polymer-Wall Interface	145
6.5.2.1 Structures and Dynamics	145
6.5.2.1.1 Density Profile.....	145
6.5.2.1.2 Rotational Diffusion of Chains	149
6.5.2.2 Bond Conformation for Crystallization	150
6.5.2.3 Bond Ordering for Crystallization	152
6.6 Conclusions	154
VII SUMMARY	157
REFERENCES	161
APPENDICES	183
CURRICULUM VITAE.....	199

LIST OF TABLES

Table		Page
2.1	Polymer hosts generally studied	14
3.1	Long-range interaction shell energy obtained from the averaging process	71
4.1	Parameters characterizing the first peak of RDFs determined from MD at 300 K for K ⁺ /H ₂ O and I/H ₂ O systems	84
4.2	Parameters characterizing the first peak of RDFs determined from MD at 300 K for K ⁺ cation in tetraglyme.....	94
5.1	Parameters characterizing the first peak of RDFs determined from MD at 300 K for tetraglyme:KI systems	108
6.1	Partial charges of atoms in MD simulations of PEO/TiO ₂ interface.....	125
6.2	The first RDFs peak positions for all pair interactions in the PEO/KI/TiO ₂ system at 300 K.....	136
6.3	The pair distances (R _{K-I} , R _{K-O}) and the coordination numbers (CN _I , CN _O) for the first coordination shell of the PEO/KI (filler-free) and the PEO/KI/TiO ₂ systems at 300 K.....	139
6.4	Long-range interaction (kJ/mol) of coarse-grained C ₂ H ₄ units at various temperatures	145

LIST OF FIGURES

Figure	Page
1.1 Schematic representation of dye-sensitized solar cells	4
2.1 Schematic representation of a dye-sensitized TiO ₂ solar cell and the electron transfer processes involved in energy conversion	12
2.2 Solvation of a salt by a PEO chain. The primary interaction is between the ether oxygens and the cation	19
2.3 Cartoon of ion motion in a polymer host	19
2.4 The structure of DME: CH ₃ -O-CH ₂ -CH ₂ -O-CH ₃	20
2.5 A segment of a PEO chain	20
2.6 Schematic representation of crystalline PEO unit cell.....	21
2.7 The helical structure of PEO.....	21
2.8 A regular helix model of the crystalline PEO complex (a) below the melting transition temperature (b) above the melting transition temperature.....	23
2.9 Top view AFM picture of the binary PEO/titania electrolyte.....	29
3.1 Periodic boundary conditions in molecular dynamics	40
3.2 Geometry of a simple chain molecule, illustrating the definition of interatomic distance r_{23} , bend angle θ_{234} , and torsion angle ϕ_{1234}	44
3.3 The time and length regimes for various simulation methods.....	50

LIST OF FIGURES (Continued)

Figure	Page
3.4	Basic elementary moves based on the standard Verdier-Stockmayer type model..... 54
3.5	Collective moves (a) reptative move (b) end-bridge move (c) concerted rotation 54
3.6	Five kinds of polymer interfaces and surfaces: (a) polymer-polymer interface, (b) polymer-small molecules interface, (c) polymer confined between two substrates, (d) polymer confined between a substrate and an air or vacuum surface, and (e) free-standing polymer thin film..... 56
3.7	Example of the mapping of a real chain into lattice by coarse graining. The degree of coarse graining increases from (a) to (c). (a) continuous space, (b) space available with a single bond length, tetrahedral bond angle, and $\phi = 180^\circ, \pm 60^\circ$, (c) rejection of alternate sites from (b) 62
3.8	The 2nd lattice. The gray spheres represent the possible twelve coordination lattice sites around a central bead (open circle)..... 63
3.9	The rotational states of a linear chain and corresponding statistical weights (a) independent bond (b) interdependent bond..... 66
3.10	The coarse graining of <i>n</i> -heptane with 4 rotors to a single rotor in 2nd lattice: (a) <i>n</i> -heptane (b) 2nd chain equivalent to <i>n</i> -heptane..... 69

LIST OF FIGURES (Continued)

Figure	Page
4.1	The fundamental quantities of ion solvation structure, coordination number N_0 (<i>area under curve</i>), Debye–Waller factor (half-width) σ^2 , center of peak, R_0 75
4.2	Atomistic models of (a) $\text{K}^+/\text{H}_2\text{O}$ and (b) $\text{I}^-/\text{H}_2\text{O}$ 83
4.3	RDFs for K^+-O (solid line) and K^+-H (dashed line)..... 83
4.4	RDFs for $\text{I}^- - \text{O}$ (solid line) and $\text{I}^- - \text{H}$ (dashed line)..... 84
4.5	Comparison of potassium EXAFS k^2 -weighted $\chi(k)$ plots for K^+ in aqueous solution from experiment (<i>solid line</i>) and MD simulation (<i>dotted line</i> : hydrogens are included, <i>dash-dot line</i> : hydrogens are excluded)..... 87
4.6	The $ \tilde{\chi}(R) $ plots corresponding to the Fourier transformed $k^2\chi(k)$ as shown in Figure 4.5. The distances were not corrected for phase shifts. The unphysical peak at 0.9\AA is an artifact of the multi-electron excitations 88
4.7	$\text{K}^+(\text{H}_2\text{O})_n$ ($n = 5, 6, 7$) clusters extracted from MD configurations. The upper figures show hydrogen atoms while the lower figures do not display hydrogen atoms 88
4.8	Comparison of iodide EXAFS k^3 -weighted $\chi(k)$ plots for iodide in aqueous solution from experiment (<i>solid line</i>) and MD-EXAFS (<i>dotted line</i> : hydrogens are included, <i>dash-dot line</i> : hydrogens are excluded)..... 90

LIST OF FIGURES (Continued)

Figure	Page
4.9	Comparisons of the R -space EXAFS spectra from experiments and MD simulations with including and excluding hydrogens 91
4.10	The structures extracted from MD configurations for the first hydration shell of Γ^- anion. Upper figures show six to eight water molecules surrounding one Γ^- anion while lower figures show only H and O that fell within the first minima of the Γ^- -H ($\leq 3 \text{ \AA}$) and Γ^- -O ($\leq 4 \text{ \AA}$) RDFs peaks, respectively..... 92
4.11	RDFs for (a) K^+ and all tetraglyme atoms, (b) K^+ -O (<i>solid line</i>), (c) K^+ -C (<i>dash-dot line</i>), and (d) K^+ -H (<i>dotted line</i>) 94
4.12	Potassium EXAFS k^2 -weighted $\chi(k)$ plots for K^+ /tetraglyme system 96
4.13	Comparison of the R -space EXAFS spectra from simulation and experiment for K^+ /tetraglyme system 96
4.14	Clusters of PEO chains within a 6 \AA radius of K^+ extracted from MD configurations 97
5.1	RDFs between (a1, a2) K^+ and all species, (b1, b2) K^+ and ether oxygens, and (c1, c2) K^+ and Γ^- in the tetraglyme:KI systems with EO:K = 10:1 (labeled by '1') and EO:K = 40:1 (labeled by '2') at 300 K 106
5.2	Comparison of the RDFs and CN of both tetraglyme:KI systems shown in (a) for K^+ -O pairs and (b) for K^+ - Γ^- pairs..... 107

LIST OF FIGURES (Continued)

Figure	Page
5.3 The coordination around K^+ of the EO:K =10:1 system. Some structures extracted from MD configurations are exemplified: (a) and (b) show the coordination number (CN) frequently found of five (from two ether oxygens and three iodide anions); (c) to (e) display CN = 6; and (f) shows CN = 7.....	108
5.4 The coordination around K^+ of the EO:K =40:1 system	109
5.5 Time-average population density distributions of tetraglyme backbone torsions along C–C and C–O bonds in pure tetraglyme and tetraglyme:KI at 300 K: (a) total dihedral distribution functions of interest, and (b) shift in dihedral angles along C–C bonds of tetraglyme:KI system from those of pure tetraglyme.....	111
5.6 The torsional angles (φ) along C–C bonds	112
5.7 The scheme of the torsional angles along C–C bonds for (a) the more stretched chains with the longer distance (d_1) between the adjacent oxygens and (b) the more compacted chains with the shorter distance (d_2) between the adjacent oxygens.....	112
5.8 The $\langle S^2 \rangle^{1/2}$ distribution of tetraglyme:KI with EO:K = 10:1 (<i>dotted line</i>), and EO:K = 40:1 (<i>dashed line</i>) compared with that of pure tetraglyme (<i>solid line</i>) at 300 K	114

LIST OF FIGURES (Continued)

Figure	Page	
5.9	Tetraglyme chains from MD simulations of pure tetraglyme and tetraglyme:KI at 300 K. The torsional angles along C–C bonds and the radius of gyration, S for each chain are presented. Figures (a) and (b) show some representative conformations of the stretched and the compacted chains, respectively.....	115
5.10	Mean square displacement of K^+ and I^- in tetraglyme:KI at 300 K.....	116
6.1	Snapshots of (a) PEO and (b) PEO/KI confined one side to TiO_2 surface and the other side to vacuum from NVT-MD simulations at 300 K. There are three regions: (i) PEO/ TiO_2 interface, (ii) PEO bulk, and (iii) PEO/vacuum surface.....	121
6.2	The total density profile of all PEO atoms (a) from TiO_2 interface to free surface, (b) near the TiO_2 interface, and (c) near the free surface. Vertical dashed lines in Figure (b) indicate division into interfacial layers	123
6.3	The MD snapshot of PEO/ TiO_2 system. The PEO at the TiO_2 interface is divided into three interfacial layers with dense packing and ordering	124
6.4	RDFs of (a) Ti atoms and PEO atoms with C, H, ether oxygen (O_{et}), and (b) TiO_2 oxygen atoms (O_{ti}) and C, H, O_{et}	126
6.5	XRD patterns of (a) pure PEO, (b) and (c) PEO/ TiO_2 nanocomposites with 5 and 10 wt. % TiO_2 nanoparticles, respectively.....	128

LIST OF FIGURES (Continued)

Figure	Page	
6.6	Backbone atom MSDs for each PEO layer (<i>dashed line, dash-dot line, dash-dot-dot line, solid line, and dotted line</i> for the 1 st layer, 2 nd layer, 3 rd layer, > 3 rd layer, and free surface, respectively) and for bulk PEO (<i>solid line with circle</i>).....	129
6.7	The PEO divided into five layers: 1 st layer (blue), 2 nd layer (green), 3 rd layer (pink) with ~4 Å thickness for each, more than 3 rd layer and less than free surface (red), and free surface (yellow) with ~10 Å thickness.....	130
6.8	The PEO (<i>solid line</i>), K ⁺ (<i>dotted line</i>), and I ⁻ (<i>dash-dot line</i>) density profiles from TiO ₂ interface to free surface of the PEO/KI/TiO ₂ composite at 300 K. Vertical dashed lines indicate the division into three interfacial PEO layers	132
6.9	The PEO density profile of the PEO/KI/TiO ₂ nanocomposite (<i>dotted line</i>) compared with that of the PEO/TiO ₂ nanocomposite (<i>solid line</i>).....	132
6.10	RDFs between (a) Ti atoms and PEO/KI species (<i>i.e.</i> C, H, O _{et} , K ⁺ , and I ⁻), and (b) O _{ti} atoms and PEO/KI species at 300 K.....	134
6.11	Comparison of the RDFs between TiO ₂ atoms (Ti, O _{ti}) and PEO atoms (C, H, O _{et}) of PEO/TiO ₂ nanocomposites with added KI (<i>solid lines</i>) and without added KI (<i>dotted lines</i>).....	135

LIST OF FIGURES (Continued)

Figure	Page
6.12	RDFs and CN for (a) $K^+ - I^-$, and (b) $K^+ - O_{et}$ for PEO/KI with EO:K = 10:1 (filler-free), and TiO_2 slab in PEO/KI with EO:K = 10:1 138
6.13	MSDs of (a) K^+ , (b) I^- , and (c) both K^+ and I^- for each region (near TiO_2 interface, away from TiO_2 interface, and free surface) compared with those of bulk..... 141
6.14	MSDs of PEO backbone atoms for each region: near TiO_2 , away from TiO_2 interface, and free surface compared with those of bulk..... 142
6.15	Snapshots of the final conformations of nanocomposites with various PE-filler interactions (neutral, attractive, and repulsive) at (a) 473 K, and (b) 298 K. Red color wall and gray wireframe denote the flat nanofiller and PE, respectively..... 147
6.16	Density profiles of PE beads as a function of z distance (a) at 473 K (melt state), (b) 298 K, and (c) both temperatures..... 148
6.17	Normalized end-to-end vector autocorrelation functions of PE chains as a function of Monte Carlo Step (MCS) for PE ($C_{40}H_{82}$) nanocomposites with neutral, attractive, and repulsive interactions at 473 K..... 150
6.18	Fraction of C-C bonds that are in the <i>trans</i> state as a function of MCS after an instantaneous cooling of nanocomposite from 473 to 298 K 152
6.19	The bond orientation order parameter, S_b , as a function of MCS after an instantaneous cooling of the nanocomposites from 473 to 298 K 154

LIST OF ABBREVIATIONS

<i>a</i>	acceleration
AC	alternating current
AFM	atomic force microscope
Al ₂ O ₃	aluminium oxide or alumina
AM	air mass
Å	Angstrom
Å ⁻¹	per Angstrom
<A>	averaged property
<i>ca.</i>	circa (approximately)
CN, N	coordination number
COMPASS	condensed-phase optimized molecular potentials for atomistic simulation studies
CPU	central processing unit
<i>D</i>	diffusion coefficient
DFT	density functional theory
DSC	differential scanning calorimeter
DSSC, DSSCs	dye-sensitized solar cell, dye-sensitized solar cells
<i>e.g.</i>	exempli gratia (for example)
<i>et al.</i>	et alia (and other)
eV	electron Volt

LIST OF ABBREVIATIONS (Continued)

E	potential energy
EXAFS	extended X-ray absorption fine structure
E_{σ} , E_{ω}	the first-, second-order short-range interaction energies
f	Mayer f -function
fs	femtosecond
F	force
$g(g^+, g^-)$	<i>gauche</i> (<i>gauche</i> plus, <i>gauche</i> minus)
g/cm^3	gram per cubic centimeter
g/mol	gram per mole
h	Planck constant
\hbar	reduced Planck constant or Dirac constant ($= h/2\pi$)
HSAB	hard/soft acid base
<i>i.e.</i>	id est (that is)
Γ	iodide anion
Γ/I_3^-	iodide/tri-iodide redox couple
J	Joule
k_B , k	Boltzmann constant ($\sim 1.38 \times 10^{-23} \text{ J K}^{-1}$)
k	wave-vector
kJ/mol	kiloJoule per mole
K	Kelvin
K^+	potassium cation

LIST OF ABBREVIATIONS (Continued)

KI	potassium iodide
KSCN	potassium thiocyanate
<i>l</i>	bond length
LJ	Lennard-Jones
<i>m</i>	atomic mass
mbar	millibar
mol/dm ³	mole per cubic decimeter or Molar
MC	Monte Carlo
MD	Molecular Dynamics
MM	Molecular Mechanics
MCS	Monte Carlo step
MSD	mean square displacement
\bar{M}_w	average molecular weight
nm	nanometer
NMR	nuclear magnetic resonance
NPT	isothermal-isobaric ensemble
NVE	microcanonical ensemble
NVT	canonical ensemble
ps	picosecond
PE	polyethylene
PEO	poly(ethylene oxide)

LIST OF ABBREVIATIONS (Continued)

PME	particle-mesh Ewald
q	charge
QM	quantum mechanics
QM/MM	quantum mechanics/molecular mechanics
QSPR	quantitative structure property relationship
r	(1) position, (2) end-to-end distance
$rand$	random number
R	gas constant ($\sim 8.314 \text{ J K}^{-1} \text{ mol}^{-1}$)
R_g	radius of gyration
RDF, $g(r)$	radial distribution function
RDFs	radial distribution functions
RIS	rotational isomeric state
s	(1) second, (2) radius of gyration
S/cm	Siemen per centimeter
S_b	bond order parameter
SNND, 2nd	second nearest neighbor diamond
SPEs	solid polymer electrolytes
$\langle S^2 \rangle^{1/2}$	root-mean square radius of gyration
t	(1) time, (2) <i>trans</i> conformation
T	temperature
T_g	glass transition temperature

LIST OF ABBREVIATIONS (Continued)

T_m	melting temperature
Tetraglyme	tetraethylene glycol dimethyl ether
TiO ₂	titanium dioxide or titania
u	statistical weight
U	statistical weight matrix
v	velocity
viz.	videlicet (namely)
V	volume
W/m ²	Watt per square meter
XRD	X-ray diffraction
Z	partition function
°C	degree Celcius
ΔG	Gibbs free energy change
ΔH	enthalpy change
ΔS	entropy change
Δt	time step
θ	(1) bond angle, (2) angle between chords
Φ	torsion angle
ε	depth of Lennard-Jones potential
ε_0	permittivity of free space
σ	zero point of Lennard-Jones potential

LIST OF ABBREVIATIONS (Continued)

σ, ω	the first-, second order interaction parameters
σ^2	Debye-Waller factor
π	pi (=22/7)
ρ	density
$\chi(E)$	fine structure factor as a function of X-ray energy, E
$\mu(E)$	absorption coefficient as a function of X-ray energy, E
$\mu_0(E)$	background absorption coefficient
$\Delta \mu_0(E_0)$	jump in the absorption background at the absorption edge, E_0
$\chi(k)$	fine structure factor as a function of wave-vector, k
$\chi(R)$	real-space representation of EXAFS spectrum

CHAPTER I

INTRODUCTION

It is assumed that the world energy demand will increase by about 70% between 2000 and 2030. Fossil fuels, supplying 80% of all energy consumed worldwide, are facing rapid resource depletion. The resource reserves of fossil fuels throughout the whole world in 2002 were projected to last 40 years for oil, 60 years for natural gas and 200 years for coal. Because of a growing demand for energy, combined with the depletion of fossil resources, global warming and its associated climate change, there is an urgent need for environmentally sustainable energy technologies. Among all the renewable energy technologies, such as wind turbines, hydropower, wave and tidal power, solar thermal, biomass-derived liquid fuels and biomass-fired electricity generation, photovoltaic technology utilizing solar energy is considered as the most promising one. Fortunately the supply of energy from the sun to the earth is gigantic: 3×10^{24} J a year, or about 10,000 times more than that the global population currently consumes. In other words, covering 0.1% of the earth's surface with solar cells with an efficiency of 10% would satisfy our present needs (Grätzel, 2001).

A photovoltaic system consists of solar cells and ancillary components. Solar cells utilize the energy from the sun by converting solar radiation directly into electricity. In 1954, researchers at the Bell Telephone Laboratories demonstrated the first practical conversion of solar radiation into electric energy by use of a *p-n*

junction type solar cell with 6% efficiency (Chapin, Fuller, and Pearson, 1954). With the advent of the space program, photovoltaic cells made from semiconductor-grade silicon quickly became the power source of choice for use on satellites. The common solar power conversion efficiencies are between 15 and 20% (Grant *et al.*, 2002). However, the relatively high cost of manufacturing these silicon cells has prevented their widespread use. Another disadvantage of silicon cells is the use of toxic chemicals in their manufacture. These aspects prompted the search for environmentally friendly and low cost solar cell alternatives (Li, Wang, L., Kang, Wang, P., and Qiu, 2006).

In 1991, dye-sensitized solar cell (DSSC) based on the mechanism of a fast regenerative photoelectrochemical process was first reported by Grätzel *et al.* (Oregon and Grätzel, 1991). The overall efficiency of this new type of solar cell was 7.1–7.9% (under simulated solar light), which is comparable to that of amorphous silicon solar cells (Grätzel, 2001). The main difference between this type of solar cell and conventional cells is that in the new cells the functional element, which is responsible for light absorption (the dye), is separated from the charge carrier transport. Such a feature makes it possible for DSSC to use low- to medium-purity materials through low-cost processes, and exhibits a commercially realistic energy-conversion efficiency. In addition, it is of great importance that the materials used in DSSC are environment benign (Li, Wang, L., Kang, Wang, P., and Qiu, 2006). For these reasons they have attracted great scientific and technological interest as potential alternatives to classical semiconductor-based photovoltaic devices (Oregon and Grätzel, 1991). The active photoelectrode is a nanocrystalline *n*-type semiconductor, usually TiO₂, modified by chemical attachment of a dye monolayer, being usually a ruthenium

complex which strongly absorbs light within wide range of the visible spectrum. On the counter electrode, a thin reflecting Pt film is deposited to catalyze the iodide regeneration. The two electrodes are brought in close proximity, while the gap contains a redox electrolyte. The electrolyte assures internal electrical contact between the two electrodes and, mainly, provides the potential barrier necessary for photovoltaic conversion (Chatzivasiloglou *et al.*, 2007). The schematic representation of DSSC is shown in Figure 1.1. Although DSSC based on liquid electrolytes have reached efficiency as high as 10% under AM 1.5 (1000 W/m²) (Nazeeruddin *et al.*, 1993), the main problem is that the liquid electrolytes may limit device stability because the liquid may evaporate when the cell is imperfectly sealed, and more generally, permeation of water or oxygen molecules and their reaction with the electrolytes may worsen cell performance. Liquid electrolytes also makes the manufacture of multi-cell modules difficult because cells must be connected electrically yet separated chemically, preferably on a single substrate (Sinke and Wienk, 1998). Recently, many attempts have been made to solve the above problems by the replacement of liquid electrolyte with solid or quasi solid-state hole conductors (Cao, Oskam, and Searson, 1995; Hagen *et al.*, 1997; Kubo *et al.*, 2001; Gebeyehu, Brabec, and Sariciftci, 2002; Longo, Nogueira, De Paoli, and Cachet, 2002; Paulsson, Hagfeldt, and Kloo, 2003; Stathatos, Lianos, Zakeeruddin, Liska, and Grätzel, 2003) which can be classified as *p*-type semiconductors, ionic liquid electrolytes and polymer electrolytes.

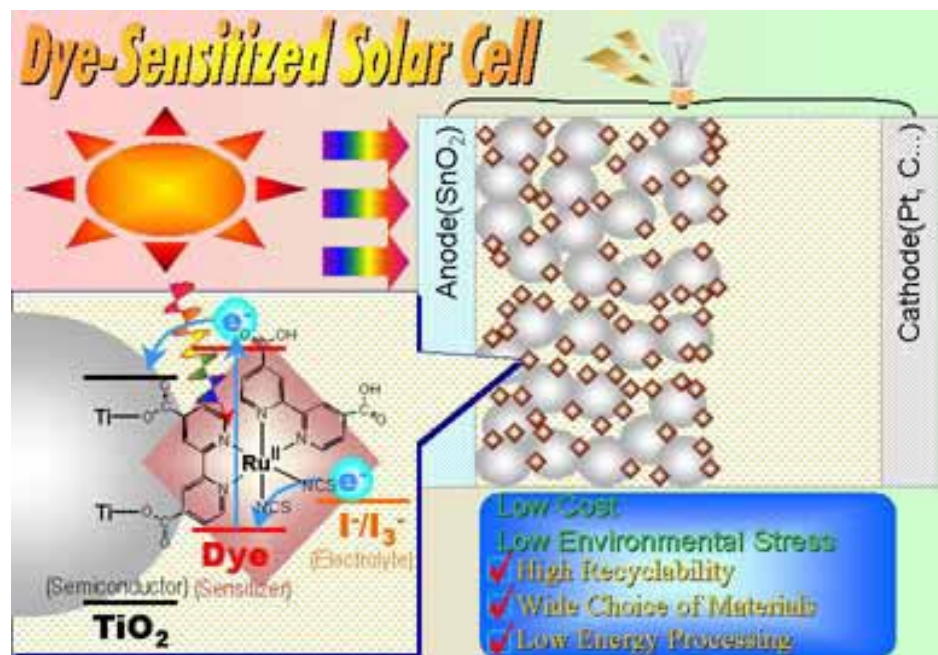


Figure 1.1 Schematic representation of dye-sensitized solar cell (Minoura Laboratory, 2008).

Solid polymer electrolytes (SPEs), usually comprised of alkali salts dissolved in a polymer matrix, are subject to intense study because they are vital components of modern electronic devices, including high energy-density batteries, fuel cells, and electrochromic displays (Vashishta, Mundy, and Shenoy, eds., 1979; Gray, 1991, 1997; MacCallum and Vincent, 1987, 1989). Because of its ability to solvate a variety of inorganic salts leading to polymer electrolytes with significant values of ionic conductivity, poly(ethylene oxide) or “PEO” is one of the most widely studied host polymer matrix for potential use as an electrolyte in high energy-density batteries (MacCallum and Vincent, 1987, 1989). It is now well-known that ion transport occurs primarily through amorphous regions of PEO:salt complexes (Berthier *et al.*, 1983). Ionic conductivity in PEO-based SPEs, however, is low at room temperature, because

large amounts of crystalline phases are present (Bruce and Vincent, 1993). For instance, for PEO:LiX ($X = \text{ClO}_4, \text{CF}_3\text{SO}_3$), ionic conductivity is in the range of 10^{-3} - 10^{-4} S/cm at 100°C , while it falls to the range of 10^{-6} - 10^{-8} S/cm at room temperature (Albinsson, Mellander, and Stevens, 1991). This limits the practical operating temperatures to the 80 - 140°C range. In addition, DSSC containing solid electrolytes have limited applications due to their low conversion efficiencies and poor electric contact between photo-electrode and electrolyte (Akhtar, Chun, and Yang, 2007). Thus, developing SPEs with high conductivity along with acceptable mechanical and other properties at room temperature is highly desirable. Molecular level understanding of ion transport in polymer:salt complexes is required to engineer systems with higher ionic conductivity at lower temperatures for improved device performance (Hyun, Dong, Rhodes, Frech, and Wheeler, 2001). Ion-polymer interactions, polymer segmental motions, and ionic association complicate ion transport mechanisms in PEO-based SPEs. Understanding each of these aspects and their interrelations in amorphous PEO is necessary to engineer PEO-based SPEs with higher ionic conductivity. Numerous experimental and computational studies on these aspects have been performed (Catlow and Mills, 1995; Borodin and Smith, 1998, 2000).

The conductivity is not only sensitive to the degree of crystallinity of polymer host, but also very sensitive to salt concentration. The concentration dependence usually shows a maximum due to competing effects. As the concentration increases, the conductivity increases due to the availability of more charge carriers. At the same time, however, formation of ion pairs and larger clusters set in, which leads to a decrease in the conductivity. In addition, at higher salt concentration, the polymer

becomes stiffer as can be seen from the rise of the glass-transition temperature, which can be ascribed to an effective transient cross-linking by the salt. Lower chain mobility accounts for an additional lowering of the conductivity.

The methodologies to reduce the crystallinity of PEO/salt complex are such as followings:

- Synthesis of new polymer *e.g.* copolymerization of macromonomer, grafting, crosslinking and networking of polymer.
- Adding small molecule plasticizer or blending with other amorphous polymer to decrease the percent of crystallinity of materials.
- Adding inorganic filler like SiO_2 , TiO_2 , Al_2O_3 to reduce the amount of crystallinity without disturbing the mechanical properties of new materials (If the filler is of nanosize and interact well with the polymer matrix, we will call this material as polymer nanocomposite) (Intarakamhang, 2005).

According to the above introduction, it can be concluded that DSSC is one of the most interesting technologies because it is low cost, non-toxic and its efficiency can be improved. The future development of the DSSC requires a deeper understanding of the involved processes as well as each component of DSSC (*i.e.* electrodes, dye, electrolyte) must be carefully and separately improved/modified. The system is indeed very complex and involves physical, organic and inorganic chemistry as well as surface science. The huge potential and tuning possibilities makes this system fascinating and is keeping researchers in various fields occupied. Some of the most important processes in this system take place on a microscopic level, involving molecular and electronic properties. Simulation, the bridge between theory

and reality, can provide the understanding at the atomistic or molecular level of the involved processes.

Thus, our interest is to employ computational molecular modeling methods including Molecular Dynamics (MD) for atomistic calculation and Monte Carlo (MC) for mesoscale calculation to study the solid polymer electrolytes of the type PEO-KI added TiO₂ nanofiller.

Research Objectives

1. To study the effect of adding KI salt and TiO₂ nanofiller in PEO-based nanocomposite electrolytes on structural, conformational and dynamics properties.
2. To apply computational molecular modeling techniques, at different length and time scale, to gain more understanding at the atomistic and mesoscale of PEO/KI/TiO₂ nanocomposite electrolytes.

Scope and Limitation of the Study

Computational Simulation

The simulation techniques employed to study structures and properties of polymer nanocomposite electrolytes were:

- **Atomistic Simulation:** Molecular Dynamics (MD) method was employed to determine the atomistic structures and to predict EXAFS spectra of K⁺ and I⁻ ions in water and K⁺ ion in tetraglyme as model complexes for SPEs used in DSSC. Besides, MD was applied to study the effects of adding KI and TiO₂ nanofiller

on structural, conformational and dynamics properties of PEO-based nanocomposite electrolytes: PEO/KI, PEO/TiO₂ and PEO/KI/TiO₂ systems. Materials Studio 4.2 simulations package provided by National Nanotechnology Center of Thailand is the software used for MD simulations of these systems.

- **Mesoscale Simulation:** Monte Carlo (MC) technique was applied to study the structures, dynamics and crystallization of monodisperse polymer melts containing nanofiller with repulsive/neutral/attractive polymer-filler interaction. For MC part, we used in-house software initially developed by Visit Vaosoongnern (Chemistry, Suranaree University of Technology) from the past collaboration with the Department of Polymer Science, University of Akron, USA during 2000-2004.

CHAPTER II

LITERATURE REVIEW

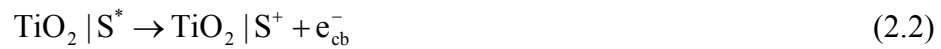
2.1 Dye-Sensitized Solar Cell (DSSC)

Several interests have motivated the development of alternative energy sources, including those related to economical and political questions, as well as those related to health and environmental concerns, *e.g.*, for decreasing air pollution and carbon dioxide emission. In view of such concerns, solar energy can be considered the most important alternative energy source because it is abundant, clean, safe, and allows energy generation in remote areas (Licht, 1995; Grätzel, 2001).

Solar cell or photovoltaic cell is a device that converts solar energy into electricity by the photovoltaic effect. In 1954, researchers at the Bell Telephone Laboratories demonstrated the first practical conversion of solar radiation into electric energy by use of a *p-n* junction type solar cell with 6% efficiency (Chapin, Fuller, and Pearson, 1954). With the advent of the space program, photovoltaic cells made from semiconductor-grade silicon quickly became the power source of choice for use on satellites. The common solar power conversion efficiencies are between 15 and 20% (Grant *et al.*, 2002). However, the relatively high cost of manufacturing these silicon cells has prevented their widespread use. Another disadvantage of silicon cells is the use of toxic chemicals in their manufacture. These aspects prompted the search for environmentally friendly and low cost solar cell alternatives (Li, Wang, L., Kang, Wang, P., and Qiu, 2006).

In 1991, dye-sensitized nanocrystalline TiO₂ solar cells based on the mechanism of a fast regenerative photoelectrochemical process were first reported by Grätzel and coworkers (Oregan and Grätzel, 1991). Dye sensitized solar cell (DSSC) or “Grätzel cell” has attracted considerable interest in the scientific community due to its low energetic production cost, low cost of the raw materials and high efficiency to convert solar energy into electricity (Nazeeruddin *et al.*, 1993; Hagfeldt and Grätzel, 1995; Grätzel, 1999). These cells achieve 10.4% certified solar power efficiencies (Grätzel, n.d.) and their stability data indicates, at least, 10 years of use in outdoor applications (Hinsch *et al.*, 2000). The efficiency of a DSSC is lower than the classical crystalline silicon cells and the next generation of solid-state thin films technology such as copper indium gallium selenide (CIGS) cells. However, DSSC technology presents lower costs and, since we still are far from the theoretical efficiency, there is a high potential for improvements in efficiency to be developed.

Energy conversion in a DSSC is based on the injection of an electron from a photoexcited state of the sensitizer dye (typically a bipyridine metal complex) into the conduction band of the nanocrystalline semiconductor (TiO₂ is by far the most employed oxide semiconductor), as depicted in Figure 2.1. These cells also employ a liquid electrolyte (usually an iodide/triiodide redox-active couple dissolved in an organic solvent) to reduce the dye cation (*viz.* regenerate the ground state of the dye). Regeneration of iodide ions, which are oxidized in this reaction to triiodide, is achieved at a platinised counter electrode, Equations 2.1-2.6:



where S, e_{cb}^- , and $e_{(\text{Pt})}^-$ represent a dye sensitizer, an electron in conduction band of TiO_2 , and an electron at a platinised counter electrode, respectively.

In summary, these cells are the result of a combination of several different materials: optically transparent conducting electrodes (used to deposit the oxide layer and the metallic catalysts, acting as photoanode and counter electrode, respectively), nanoparticulated oxide semiconductors, inorganic metal complexes or organic dyes (as sensitizers), inorganic salts (in the electrolyte), solvents and metallic catalysts. Each material performs a specific task in the complex mechanism of a DSSC and contributes to the overall solar cell efficiency.

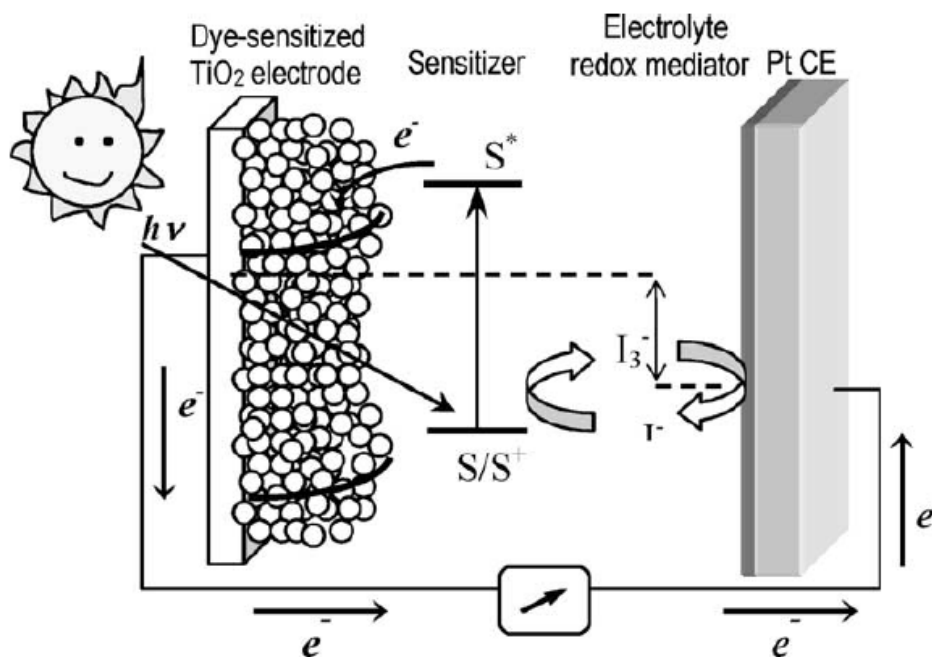


Figure 2.1 Schematic representation of a dye-sensitized TiO₂ solar cell and the electron transfer processes involved in energy conversion (S represents the dye sensitizer and I⁻/I₃⁻ is the charge mediator) (Nogueira, Longo, and De Paoli, 2004).

2.2 Solid Polymer Electrolytes (SPEs)

Solid Polymer Electrolytes (SPEs) consist of salts dissolved in high molecular weight polymer. Polymer, which can dissolve salt must be comprise of O, N or S atom because these atoms can interact with cation, and make decompositive salt to have better conductivity. Conductive polymer-salt complexes were first described in the early 1970's, and were quickly adopted by the electrochemical community, who recognized the potential of a flexible, plastic, ion transporting medium for vital applications such as energy storage and electrochemical displays (Vincent, ed., 1978;

Vashishta, Mundy, and Shenoy, eds., 1979). In contrast to the cases of brittle glassy or crystalline solid conductors, polymer materials can accommodate volume changes, which makes them particularly suited for applications together with intercalation materials, such as the anode and cathode in a rechargeable battery. And, in contrast to liquid electrolytes, polymer electrolytes do not leak any harmful chemicals, and are therefore much safer.

Unfortunately, the ionic conductivity of a polymer electrolyte is, at a given temperature, at least 100 or 1000 times less than in a liquid or the better ceramic electrolytes. A considerable scientific effort has been dedicated to exploring and understanding the characteristics of these electrolyte systems. Many investigations have focused on developing SPEs with high ionic conductivities (10^{-3} S/cm or higher) at ambient temperature (Chintapalli, 1996).

In polymer electrolytes, the polymer host works both as an electrolyte and as separator isolating the electrodes. A successful polymer candidate should satisfy the following requirements (Gray, 1991; Connor, ed., 1997; Lin, Boinske, and Halley, 1996):

- The polymer must contain atoms or groups with sufficient electron donor power to form co-ordination bonds with cations. For alkali ions, such as lithium, oxygen is regarded as the preferred electron donor.
- The polymer must have a suitable distance between coordinating sites to allow the formation of multiple intra-polymer bonds for good solubility of cations.
- The polymer should have low barriers to bond rotation to facilitate ion motion.

To date, several polymer hosts have been developed and characterized as shown in Table 2.1.

Table 2.1 Polymer hosts generally studied (Stephan, 2006)

Polymer host	Repeat unit	T_g (°C)	T_m (°C)
Poly(ethylene oxide)	$-(\text{CH}_2-\text{CH}_2-\text{O})_n-$	-64	65
Poly(propylene oxide)	$-(\text{CH}(\text{CH}_3)-\text{CH}_2-\text{O})_n-$	-60	- ^a
Poly(acrylonitrile)	$-(\text{CH}_2-\text{CH}(\text{CN}))_n-$	125	317
Poly(methyl methacrylate)	$-(\text{CH}_2\text{C}(\text{CH}_3)(\text{COOCH}_3))_n-$	105	-
Poly(vinyl chloride)	$-(\text{CH}_2-\text{CHCl})_n-$	85	-
Poly(vinylidene fluoride)	$-(\text{CH}_2-\text{CF}_2)_n-$	-40	171
Poly(vinylidene fluoride-hexafluoropropylene)	$-(\text{CH}_2-\text{CF}_2)_n-(\text{CF}(\text{CF}_3)-\text{CF}_2)_m-$	-90	135

^aAmorphous

In the field of thermodynamics of polymer-ion solvation, when a salt is dissolved into a polymer matrix, the free energy change is given by the standard Gibbs free energy expression:

$$\Delta G_{\text{mixing}} = \Delta H_{\text{mixing}} - T\Delta S_{\text{mixing}} \quad (2.7)$$

When the ΔG_{mixing} is less than zero, the mixing process occurs spontaneously.

It is clear that one must consider changes in both entropy and enthalpy.

The enthalpy change, ΔH , is most straightforward, consisting of a positive part from the lattice energy of the salt, and a negative part from ionic coordination to the polymer. For a complete mixing, the ions should therefore not bind too efficiently to one other, but form bonds with the polymer solvent. For most polymer electrolytes, this means that cations should coordinate electrostatically to the polymer backbone, while the anions should diffuse freely in the matrix, with a minimum of interaction with the polymer and especially with the cations. A salt with a small univalent cation and a large anion seems to fulfill these requirements: low lattice enthalpy, weak ion-ion bonding and strong cation-polymer coordination.

The entropy change, ΔS , is more complex. First, there is a positive entropy contribution from the break-up of the crystal lattice of the ionic salt, and the subsequent disordering of the ions in the system. This effect is compensated for by an increased rigidity in the polymeric system when the cations crosslink different parts of the polymer, thereby reducing its translational and rotational motion. On the other hand, salt dissolution facilitates more polymer configurations via multidentate coordination to the cation – an effect which leads to an increase in entropy. Nevertheless, if ΔS is negative, Gibbs free energy should become positive at high temperatures, where out-salting will occur – the very opposite effect of dissolution in most liquid systems (MacCallum and Vincent, eds., 1989).

As is evident from the discussion on the enthalpy of mixing, it is necessary that the polymer in a polymer electrolyte has a strong coordination with the cations. Therefore, polymers with groups or atoms that can serve as electron donors are most suitable. Such polymers can be found among the polyethers, polyimides or polythiols (Pistoia, ed., 1994). The most common polymer type used in polymer electrolytes has

so far been PEO, and it is also the subject of investigation in this thesis. PEO shows sufficient thermal and chemical stability, and has a spacing between the oxygen groups which is ideal for cation solvation (for example, both $-(\text{CH}_2\text{CH}_2\text{CH}_2\text{O})_n-$ and $-(\text{CH}_2\text{O})_n-$ are much poorer solvents). Since PEO has no double bonds, it displays a large flexibility and can therefore coordinate with many different types of cations.

In battery applications, for example, ion conduction has been shown to take place in the amorphous phase. The disadvantage of PEO as a salt host then becomes apparent, since ~70-95% of pure PEO is crystalline at room temperature, depending on its molecular weight (Takahashi and Tadokoro, 1973). Therefore, much research effort has been invested in modifying the polymer to prevent it from crystallizing, *e.g.*, by attaching a methyl group to the monomer unit to create poly(propylene oxide), PPO (MacCallum and Vincent, eds., 1987). However, PPO and other modified systems have poorer solubility for salt than PEO. Better results have been achieved with block copolymers, comb-polymers or cross-links – all are ways to prevent PEO from crystallizing (Przyluski and Wiczorek, 1992).

Other ways to increase the “amorphicity” of the systems have been to introduce small additives, plasticizers or nano-size particles into the polymer host. They disturb the local crystal field and suppress order (Hug, Farrington, Koksang, and Tonder, 1992). These additives have been shown to increase the conductivity with several orders of magnitude. The presence of a plasticizer like poly(ethylene glycol), PEG, also results in a lower glass transition temperature, T_g , due to weaker interactions between the ions and the polymer chain, and can furthermore cause higher ion dissociation (Vincent, 1995).

2.3 Poly(ethylene oxide), PEO

PEO is one of the most widely studied host polymer matrix for potential use as an electrolyte in high energy-density batteries because of its ability to solvate a variety of inorganic salts leading to polymer electrolytes with significant values of ionic conductivity (MacCallum and Vincent, 1987, 1989). The solvation of salt occurs through the association of the metallic cation with the oxygen atom in the backbone (Figure 2.2) and the mechanism of ionic motion of a cation (*e.g.* Li^+) in a PEO-host is proposed and displayed in Figure 2.3.

The chemical structure of PEO explains most of the properties of this polymer host. Figure 2.4 shows the structure of 1, 2-dimethoxyethane (DME), the shortest and simplest ether molecule having the local conformational properties of PEO (Smith, Jaffe, and Yoon, 1993; Lin, Boinske, and Halley, 1996; Jaffe, Smith, and Yoon, 1993). A segment of a long PEO polymer chain is shown in Figure 2.5. The melting point of PEO is a function of the average molecular weight and molecular weight distribution of the sample. Usually, it varies from 60°C for lower molecular weights (~4000 g/mol) to 66°C for bigger molecular weights (~100,000 g/mol) (Gray, 1991). T_g also displays a close relationship with molecular weight, it grows up to a value of -17°C of a molecular weight 6000 g/mol (Faucher *et al.*, 1966). Values of -65°C and -60°C are reported for higher molecular weight samples (Gray, 1991). PEO is completely soluble at room temperature in water and also soluble in a wide range of common organic solvents (Iverson, 1962) such as acetonitrile, dichloromethane, carbon tetrachloride, tetrahydrofuran and benzene. PEO and most PEO-salt mixtures exhibit co-existence between crystalline and amorphous phases; in fact only 15-30% of PEO is in the amorphous phase at room temperature (Smith, Jaffe, and Yoon, 1993).

The unit structure of crystalline PEO has been well established from x-rays and neutron scattering experiments (Smith, Jaffe, and Yoon, 1993; Lin, Boinske, and Halley, 1996; Krishnan and Balasubramanian, 2004). As shown in Figure 2.6, it contains four helical chains in a cell. Each chain has a 7_2 helical structure as shown in Figure 2.7, which contains seven ethylene oxide repeat units with two turns in a fiber period of 19.3 Å (Intarakamhang, 2005). When operated at room temperature, at which PEO displays a large degree of crystallinity (a major barrier to ions transport), polymer electrolytes always end up with an undesirably low ionic conductivity. For example, polymer electrolyte systems (PEO/LiX) give an ionic conductivity of the order of 10^{-6} S/cm at ambient temperature. Therefore, current research efforts to develop batteries with better performance resulting from higher ionic conductivity are mainly focused on lowering the degree of polymer crystallinity under ambient temperature. To obtain a more amorphous polymer at ambient temperature, it is necessary to introduce a certain degree of disorder in the structure. This is achieved by using blends (Li and Khan, 1993), copolymers, comb-branched polymers and cross-linked networks (MacCallum and Vincent, eds., 1987). All these modifications have been achieved either by reducing the crystallinity of the polymer or by lowering T_g . Also, the incorporation of nanosized silica or other oxides has produced interesting results (Weston and Steele, 1982; Croce, Appetecchi, Persi, and Scrosati, 1998).

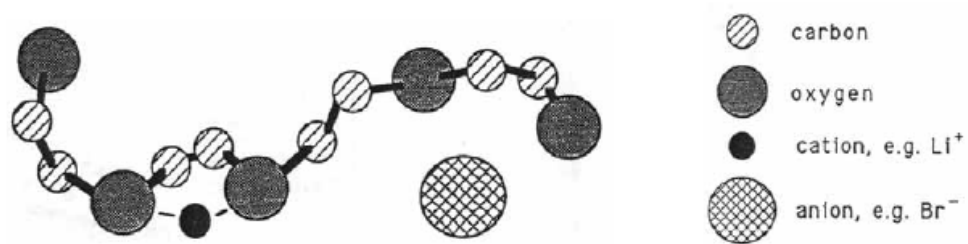


Figure 2.2 Solvation of a salt by a PEO chain. The primary interaction is between the ether oxygens and the cation.

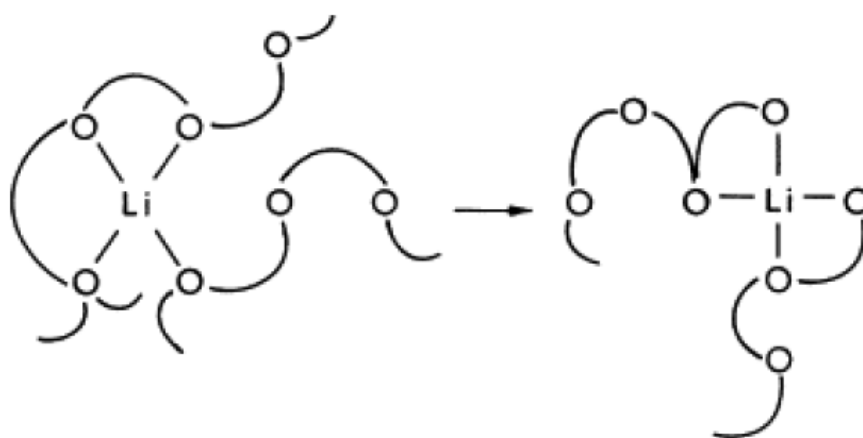


Figure 2.3 Cartoon of ion motion in a polymer host (Stephan, 2006).

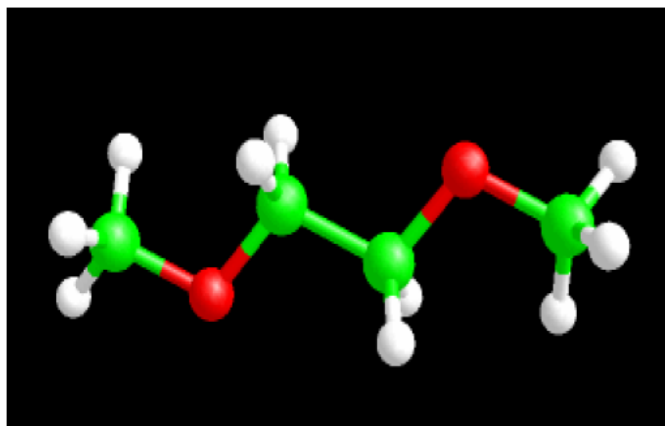


Figure 2.4 The structure of DME: CH₃-O-CH₂-CH₂-O-CH₃. The green, red and white spheres represent carbon, oxygen and hydrogen, respectively (Jaffe, Smith, and Yoon, 1993).

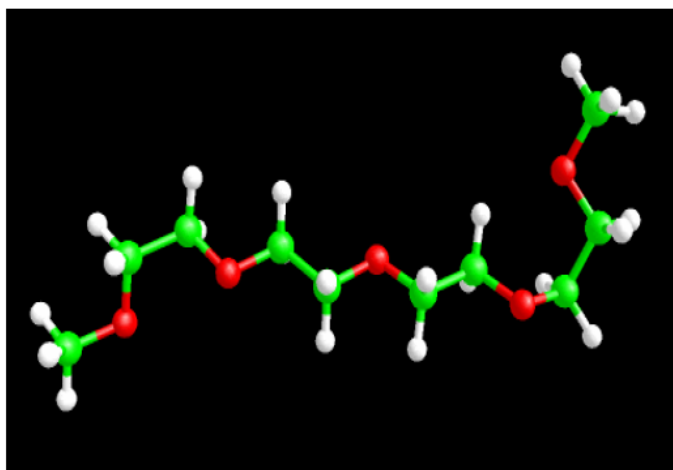


Figure 2.5 A segment of a PEO chain (Lin, Boinske, and Halley, 1996).

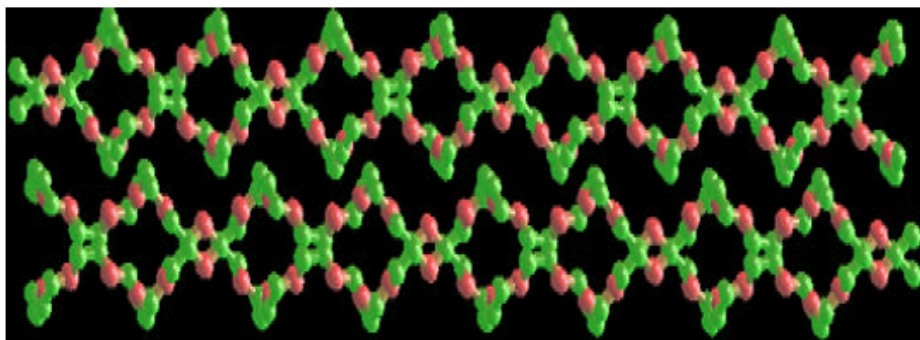


Figure 2.6 Schematic representation of crystalline PEO unit cell. Hydrogen atoms are not shown here for clarity (Krishnan and Balasubramanian, 2004).

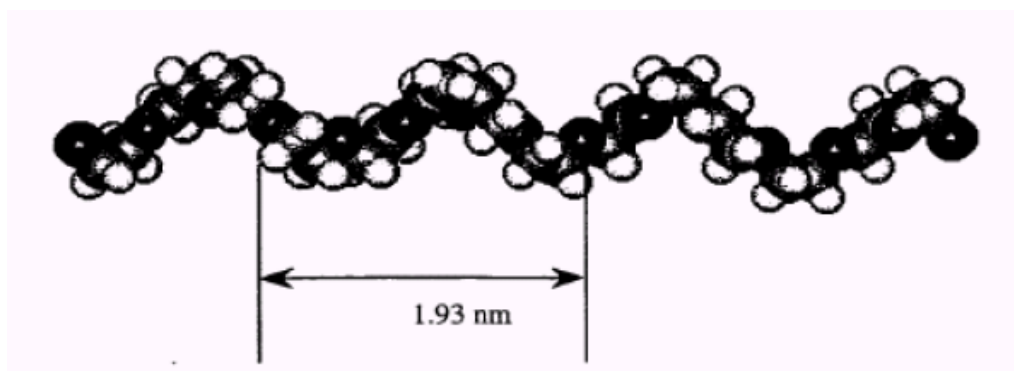


Figure 2.7 The helical structure of PEO.

2.4 PEO-Salt Electrolytes

In 1981, Papke and coworkers support a single strand helical arrangement with a 2.6 Å inside diameter of PEO chains with Na and K salt complexes on the basis of infrared and Raman studies as illustrated in Figure 2.8. Their molecular model indicates that this tunnel comprises *trans* (*t*) C–O bonds and alternating *gauche* (*g*) C–C bonds, and four oxygen atoms of polymer coordinate with cation placed inside the helix. On the contrary, Wright *et al.* proposed a double strand helical arrangement of the PEO chains based on their investigations on the interpretation from crystallographic data from X-ray fiber photograph on KSCN and NaSCN complexes.

It is clear that PEO is able to solvate a wide range of metal salts, including alkali metals, alkaline earth metals and transition metals. The different of salt influence the electrolyte properties. For most polymer-salt complexes, cations should bind to the polymer chain instead of other ions. Also, to freely move in the polymer matrix, anions should have minimal interactions with the polymer and the cations. To satisfy all these requirements, *e.g.*, weak anion-cation interaction and strong cation-polymer bonding, a salt with a small univalent cation and a large anion is needed, such as lithium iodide (LiI) and potassium iodide (KI).

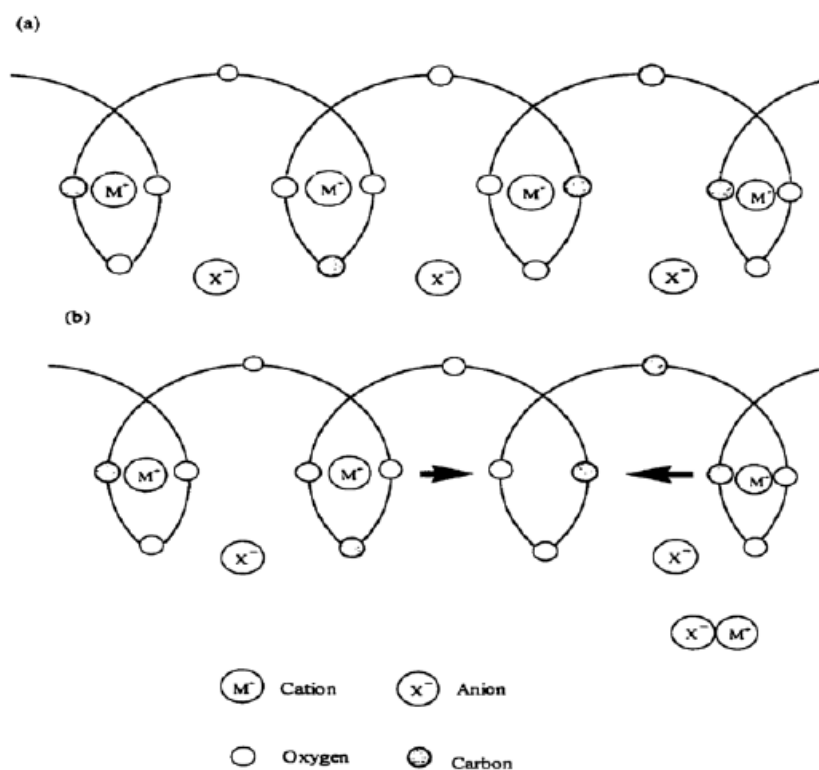


Figure 2.8 A regular helix model of the crystalline PEO complex (a) below the melting transition temperature (b) above the melting transition temperature (Wright, 1975, quoted in Puatrakul, 2000).

The solubility of cations in the polymer is determined by cation-polymer interactions, which can be predicted by the hard/soft acid base (HSAB) principle (Gray, 1991). The HSAB principle was formulated by Pearson as a means to explain and predict the solubility of complexes formed between Lewis acids and bases. A “hard” acid consists of smaller and non polarizable cations, *e.g.* alkali ions, while a “soft” acid has larger and easily distorted cations, *e.g.* Hg^{2+} . A “hard” base has non-polarizable ligands with high electronegativity, *e.g.* ether oxygen, while a “soft” base has ligands with more polarizable groups, *e.g.* thio group in thioether. The HSAB

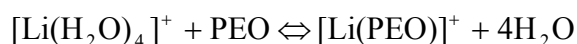
principle states that matching hard acid with hard bases or soft acid with soft bases. This yields the strongest interaction, or the strongest solvation. Therefore, for PEO polymers with hard bases, the best candidates for cations are non-polarizable small cations, *e.g.* Li^+ , Na^+ , K^+ .

To dissolve ions in less polar solvents, such as polyether, a large anion with delocalized charge is required. The following order predicts the most appropriate anions for polyether-based polymer electrolytes (Gray, 1991):



Large and polarizable monatomic anions, *e.g.* I^- , are very easily dissolved in polyether-based polymer electrolytes.

An important aspect of ion-polymer interactions is the chelating effect (Morgan, 1920). It occurs when simple solvent molecules coordinated to a central ion are replaced by multidentate ligands, *i.e.* molecules that can form more than one bond with the central ion. An example of such a process is the exchange of four water molecules coordinated to Li^+ for a single PEO chain that can provide four ether oxygens. The total reaction, which consists of four steps, can be written as:



The disorder of the whole system is increased because there are two species on the left side of the equation and five species on the right side. This leads to a large positive entropy and explains why, in general, chelating complexes are very stable. The total equilibrium concentrations of lithium complexes will depend on both the favorable enthalpy of Li^+ -water interactions and increased entropy associated with binding to PEO chains.

2.5 Enhancement Conductivity of SPEs

Considerable efforts have been devoted to the development of SPEs with high ionic conductivity and dimensional stability. Various efforts have been made to design new polymeric matrices by synthetic processes or modifying existing polyether-salt complexes, and improve ionic conductivity. There are two means to increase the ionic conductivity of the dry SPEs: (I) suppression of crystallization of polymer chains to improve polymer chain mobility; (II) increase in the carrier concentration (Ruiz *et al.*, 2000; Chen *et al.*, 2002, quoted in Intarakamhang, 2005). The suppression of crystallization of polymer chains to improve polymer chain mobility can be realized by

- (i) synthesis of new polymer *e.g.* copolymerization of macromonomer, grafting, cross-linking and networking of polymer;
- (ii) adding small molecule plasticizer or blending with other amorphous polymer to decrease the percent of crystallinity of materials, and
- (iii) adding inorganic filler like SiO_2 , TiO_2 , Al_2O_3 to reduce the amount of crystallinity without disturbing the mechanical properties of new materials. If the filler is of nanosize and interact well with the polymer matrix, we will call this material as polymer nanocomposite (Intarakamhang, 2005).

In this research, the method of adding TiO_2 nanoparticle to PEO-based electrolytes will be studied.

2.6 PEO-TiO₂ Nanocomposite for DSSC

To improve the mechanical, interfacial, and conductivity properties of the polymer electrolytes, an alternative approach, which consists of developing a solvent-free solid electrolyte by the addition of “solid plasticizers” (*e.g.*, nanoscale inorganic fillers) to polymer electrolytes is studied by many researchers both using experimental and computational methods. The addition of ceramic nanoparticles like SiO₂, TiO₂, Al₂O₃ to polymer electrolytes, initially done to enhance mechanical properties, has also been found to improve the anodic stability (Croce *et al.*, 1999), cyclability (Appetecchi, Dautzenberg *et al.*, 1998; Appetecchi, Mastragostino *et al.*, 1998), sometimes conductivity (Croce *et al.*, 1999; Capiglia *et al.*, 1999; Scrosati *et al.*, 2000; Kumar and Scanlon, 1999), and cation transfer number (Croce *et al.*, 1999; Capiglia *et al.*, 1999; Scrosati *et al.*, 2000) of polymer electrolytes without causing any observed degradations.

It is widely recognized that the ionic conductivity of polymer electrolytes can be considerably enhanced by the introduction of inorganic fillers, which also inhibit polyether crystallinity and improves the mechanical properties of the electrolyte. Conductivities as high as 10⁻⁴ S/cm at 320 K have been reported for PEO-LiClO₄ electrolytes containing nanosize particles of TiO₂ and Al₂O₃ (Croce, Appetecchi, Persi, and Scrosati, 1998; Kumar, Scanlon, and Spry, 2001). The conductivity enhancement has been ascribed to disorder caused by interactions between Lewis acid sites on the nanoparticle surface and the base species present in the system (polymer chain and anions groups). This leads to a weaker interaction between polymer and Li⁺ ions (Croce *et al.*, 1998; Marcinek *et al.*, 2000; Forsyth *et al.*, 2002; Wiczorek *et al.*, 1998).

Despite all research efforts to investigate the particle influences on the Li^+ conductivity, little is known about the interaction of the inorganic fillers with the polymer and ions. Furthermore, as recently remarked by Forsyth *et al.* (2002), the nanocomposite polymer electrolyte research encountered difficulty in terms of measurement reproducibility. As pointed by Kumar *et al.* (2001), conductivity enhancement in composite PEO electrolytes depend upon many factors such as the type of polymer-ceramic system, particle ceramic phase, particle size, annealing parameters (or thermal history), filler concentration and temperature. The influence of the particle on the PEO properties can be understood in terms of two different effects. The first is related to the space charge created around the particle, which has influence on the lithium and polymer mobility because of the following mechanisms: (a) electrostatic interaction between the particle and the lithium ion; (b) the interaction between particles and polymer which modify the segmental motion of the polymer at temperatures higher than T_g . The second effect concerns the influence of the particles on the polymer morphology. It is well described in the literature that the addition of oxides, such as Al_2O_3 , TiO_2 , reduces the crystallinity of the nanocomposites, resulting in changes of the Li^+ mobility (Forsyth *et al.*, 2002; Wiczorek *et al.*, 1998; Dai, Wang *et al.*, 1998; Dai, Greenbaum *et al.*, 1998). From our point of view, the present knowledge of these systems is not sufficient to establish the relative importance of the two above-mentioned effects.

Dai *et al.* (1998) investigated the effects of nanoscale Al_2O_3 and MgO on highly concentrated PEO/LiI electrolytes by ^7Li NMR and conductivity measurements and showed that the addition of Al_2O_3 improve the conductivity due to the suppression of crystalline phases in the electrolyte. Mustarelli *et al.* (1999) examined

the cation dynamics of the composites formed by PEO, lithium salts and PEO nanoscale silica and lithium triborate glass. The authors observed that the addition of the fillers increased the activation energy of the lithium motion and concluded that the ^7Li spin dynamics was influenced by the filler nanoparticles. Stergiopoulos *et al.* (2002) employed AFM and DSC techniques to study the morphology and crystallinity of PEO matrix introduced the titania (Degussa P25) filler. The AFM top-view image of the binary electrolyte as shown in Figure 2.9, reveals that, in the presence of the titania filler, the crystallinity of the PEO decreases considerably, in excellent agreement with the DSC results. The AFM analysis shows the existence of two distinct phases: the first one corresponds mainly to the original polymer matrix, it is crystalline and very compact; the second is an amorphous area consisting of polymer subunits held together in a parallel orientation and forming straight long chains, along which TiO_2 spherical particles of about 20-25 nm in diameter are distributed. The polymer chains separated by the titania particles are arranged in a three-dimensional, mechanically stable network that creates free space and voids into which the iodide/triiodide anions can easily migrate. Recently, Forsyth *et al.* (2002) analyzed the effect of nanoparticle TiO_2 fillers on the structural and transport properties in amorphous polymer electrolytes. Using a combination of techniques and spectroscopic tools (^1H and ^7Li NMR, Raman, positron annihilation and AC impedance) they remarked the interaction between the TiO_2 filler surface and the polymer electrolyte. The authors also mention the importance of the filler surface area as a key factor for determining high conductivity.

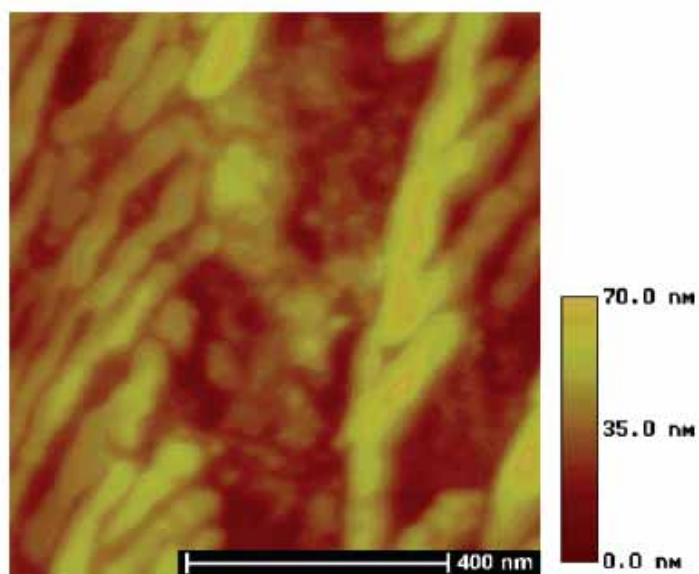


Figure 2.9 Top view AFM picture of the binary PEO/titania electrolyte.

Among several research techniques, molecular simulations provide an excellent opportunity to directly study the changes in polymer electrolyte properties with the addition of nanoparticles. Previously, Monte Carlo (MC) and Molecular Dynamics (MD) simulations performed for various model polymers near planar solid surfaces indicated that molecular arrangements, conformations and dynamics of the polymer were strongly perturbed with respect to the isotropic bulk. The strength of the nanoparticle-polymer interaction and the nanoparticle specific surface area were found to be the most important factors controlling the properties of the interfacial polymer. The addition of nanoparticles with attractive interactions led to decreased polymer dynamics and increased viscosity, whereas the addition of nanoparticles with the repulsive, or excluded volume, interactions led to increased polymer dynamics and decreased viscosity (Smith, Bedrov, Li, and Bytner, 2002; Starr *et al.*, 2002).

These effects were found to scale linearly with the specific surface area of nanoparticles (Smith, Bedrov, Li, and Bytner, 2002).

In this work, various computational molecular modeling methods including MD for atomistic calculation and MC for mesoscale calculation will be employed to study the effects of adding TiO₂ nanoparticle into the PEO-based electrolytes on structural, conformational and dynamics properties of PEO. TiO₂ is widely used as the filler in polymer nanocomposite electrolytes because of its many advantages: it is a low cost, widely available, non-toxic and biocompatible material, and as such is even used in health care products as well as domestic applications such as paint pigmentation.

CHAPTER III

COMPUTATIONAL MOLECULAR MODELING

3.1 Computational Chemistry

Since the development of the first computers in the early 1950's, scientists have tried to explore how these machines might be used in Chemistry. From the very beginning, the field of Computational Chemistry focused either on solving complex mathematical problems, typically quantum mechanical, or has tried to model the dynamical behavior of atomic and molecular systems. The boundaries between these two areas have never been well defined and, today, we see a convergence between quantum chemistry and simulation in studying chemical reactions (Curtiss and Gordon, eds., 2004).

With advances in computer technology leading to ever faster computers, Computational Chemistry has become an increasingly reliable tool for investigating systems where experimental techniques still provide too little information. Ultra-fast spectroscopy can be used to follow fast reactions but only at a molecular level. A variety of diffraction techniques can also give detailed information about crystalline structure, but have difficulties monitoring changes at a molecular level. This is why the exponential growth in computer power has led to a corresponding growth in the number of computational chemists and in the variety of different computational techniques available for solving chemical problems: *ab initio* Quantum Mechanics (QM), semi-empirical methods, Density Functional Theory (DFT), Monte Carlo

(MC), Molecular Mechanics (MM), Molecular Dynamics (MD), QM/MM, Car-Parrinello, *etc.*

There are two main branches within the Computational Chemistry: the computationally expensive methods which try to explore the electronic structure of small systems or systems with fixed crystal structures by quantum mechanical methods; and methods which focus on the atomic structure and dynamics of much larger systems but using less complex calculations. In this thesis, the focus is on the latter – simulating atomic and molecular interaction with the mathematics of classical mechanics. The following text is based on (Allen and Tildesley, 1989; Haile, 1997; Colbourn, 1994; Rapaport, 1995).

3.2 Molecular Dynamics (MD)

3.2.1 The Simulation Method

In reality, atoms and molecules in solid materials are far from static unless the temperature is low; but even at 0 K, vibrational motion remains. For ionically conductive materials, atomic movement is the subject of major interest. Molecular Dynamics allows us to simulate the dynamics of the particles in a well-defined system to gain greater insights into local structure and local dynamics – such as ion transport in solid materials.

In an MD simulation, atomic motion in a chemical system is described in classical mechanics terms by solving Newton's equations of motion:

$$\vec{F}_i = m_i \vec{a}_i \quad (3.1)$$

for each atom i in a system of N atoms: m_i is their respective atomic mass; $a_i = d^2 r_i / dt^2$ is their acceleration; and F_i is the force acting upon atom i due to interactions with all other particles in the system. The forces are generated from a universal energy potential E :

$$-\frac{dE}{d\vec{r}_i} = \vec{F}_i = m_i \frac{d^2 \vec{r}_i}{dt^2} \quad (3.2)$$

The basic idea of MD goes back to classical idea in Physics – that if one knows the location of the particles in the Universe, and the forces acting between them, one is able to predict the entire future. In a normal MD simulation, this Universe comprises only a few thousand atoms; in extreme cases, up to a million.

With Newton's equations, it is possible to calculate sequentially the locations and velocities of all particles in the system. This generates a sequence of snapshots which constitutes a “movie” of the simulated system on the atomic scale. Due to the massive computer time necessary to solve these equations for a large number of particles, the movies are generally fairly short – in this work in the pico- or nanosecond regime. All that is needed to solve the equations of motion are the masses of the particles and a description of the potentials, E .

In order to solve Equation 3.2, various kinds of numerical integration methods²³ such as Gear, Verlet, leapfrog, and velocity Verlet have been developed.

From the Verlet algorithm, which is based on particle position at time t , $r(t)$, acceleration at time t , $a(t)$, and the position from previous time $r(t-\Delta t)$, the new position of a particle after time Δt (Δt is the time-step between two snapshots.) is given by

$$r(t + \Delta t) = 2r(t) - r(t - \Delta t) + \Delta t^2 a(t) \quad (3.3)$$

Then, the velocity at time t can be calculated by

$$v(t) = \frac{r(t + \Delta t) - r(t - \Delta t)}{2\Delta t} \quad (3.4)$$

The Verlet algorithm uses no explicit velocities. The advantages of the Verlet algorithm are, *i*) it is straightforward, and *ii*) the storage requirements are modest. The disadvantage is that the algorithm is of moderate precision.

The leapfrog algorithm works stepwise by:

- Calculating the acceleration at time t according to Equation 3.2.
- Updating the velocity at time $t + \Delta t / 2$ using

$$v(t + \Delta t / 2) = v(t - \Delta t / 2) + a(t)\Delta t \quad (3.5)$$

- Calculating the atom position in the snapshot using:

$$r(t + \Delta t) = r(t) + v(t + \Delta t / 2)\Delta t \quad (3.6)$$

In this way, the velocities *leap* over the positions, then the positions *leap* over the velocities. The advantage of this algorithm is that the velocities are explicitly calculated, however, the disadvantage is that they are not calculated at the same time as the positions.

The velocity Verlet algorithm is as follows:

$$r(t + \Delta t) = r(t) + \Delta t v(t) + \frac{\Delta t^2 a(t)}{2} \quad (3.7)$$

$$a(t + \Delta t) = \frac{f(t + \Delta t)}{m} \quad (3.8)$$

$$v(t + \Delta t) = v(t) + \frac{1}{2} \Delta t [a(t) + a(t + \Delta t)] \quad (3.9)$$

This algorithm yields positions, velocities and accelerations at the same time. There is no compromise on precision.

The MD simulation method is very straightforward, but one must bear in mind that it is based on some severe approximations. At the highest level, the Born-Oppenheimer approximation is made, separating the wavefunction for the electrons from those of the nuclei. The Schrödinger equation can then be solved for every fixed nuclear arrangement, given the electronic energy contribution. Together with the nuclear –nuclear repulsion, this energy determines the potential energy surface, E . At the next level of approximation, all nuclei are treated as classical particles moving on the potential energy surface, and the Schrödinger equation is replaced by Newton's

equations of motion. At the lowest level of approximation, the potential energy surface is approximated to an analytical potential energy function which gives the potential energy and interatomic forces as a function of atomic coordinates.

3.2.2 Forcefields for MD Simulations

In the context of molecular modeling, a forcefield means the energy functions and parameter sets used to calculate the potential energy of a system. The energy functions and parameter sets are either derived from quantum chemistry calculations or empirically from experimental data. Typically, classical forcefields (described here) employ two-body pairwise additive potentials and ignore multi-body dispersion and many-body polarization effects. The basic functional form of a classical forcefield can be regarded as the sum of nonbonded interactions, also called intermolecular interactions, and intramolecular interactions (bond stretch, valence angles and dihedral angles):

$$E = \sum_{i \neq j} E_{ij}^{NB}(r) + \sum_{ij} E_{ij}^s(r) + \sum_{ijk} E_{ijk}^b(\theta) + \sum_{ijkl} E_{ijkl}^t(\Phi) \quad (3.10)$$

where r is the distance between atom centers, $E_{ij}^{NB}(r)$ is the nonbonded energy associated between atom i and j , $E_{ij}^s(r)$ is the covalent bond stretching energy between atom pair i and j , $E_{ijk}^b(\theta)$ is the bond-angle bending energy that depends on the angle θ formed by atoms i , j and k , and $E_{ijkl}^t(\Phi)$ is the torsional energy arising from rotation around the dihedral angle Φ defined by atoms i, j, k and l . Nonbonded interactions $E_{ij}^{NB}(r)$, the interactions between atoms in different molecules or in the

same molecules separated by two or more atoms, are composed of electrostatic interactions and van der Waals interactions as given by:

$$E_{ij}^{NB}(r) = E_{ij}^{elec}(r) + E_{ij}^{vdw}(r) \quad (3.11)$$

The summations run over all interactions of each type present in each molecule and between molecules. The bond-stretch, bond-angle and torsional-angle terms have many forms. In the vast majority of forcefields used in Molecular Dynamics simulations, bond breaking is not possible; this is also the case for the forcefields used in this work. The electrostatic energy, E_{ij}^{elec} , also called the Coulombic energy, is directly related to atomic charges by Coulombs law,

$$E_{ij}^{elec}(r) = \frac{1}{4\pi\epsilon_0} \frac{q_i q_j}{r} \quad (3.12)$$

where q_i , q_j are the charges on atoms i and j , and ϵ_0 is the permittivity of free space. There are many forms used to describe the van der Waals energy. The two most popularly used are the Lennard-Jones (LJ) potential (Lennard-Jones, 1931),

$$U(r) = \left(\frac{A}{r^{12}} \right) - \left(\frac{B}{r^6} \right) = 4\epsilon \left[\left(\frac{\sigma}{r} \right)^{12} - \left(\frac{\sigma}{r} \right)^6 \right] \quad (3.13)$$

where $A = 4\epsilon\sigma^{12}$ and $B = 4\epsilon\sigma^6$ and the Buckingham potential,

$$U(r) = A' \exp(-B'r) - \frac{C'}{r^6} \quad (3.14)$$

In Equation 3.13 and 3.14, A , B , ε , σ , A' , B' and C' are constants fitted to *ab initio* and/or experimental data. The parameters A' and B' determine the short range repulsive interaction, C' is the dispersion parameter. The parameters ε and σ have the significance of being the depth and zero point of the potential. Both the LJ and Buckingham potential include the long-range London dispersion term.

Such classical forcefields are used widely in the Molecular Dynamics simulations of polymer electrolytes, but recent Molecular Dynamics simulations by Smith and coworkers have shown that polarization effects can play a very important role for these systems and should not be ignored (Londono *et al.*, 1997).

3.2.3 Periodic Boundary Conditions and Other Requirements

Since the computation time required to calculate the trajectories of all N particles in a simulation box increases with N^2 , the simulated system cannot be made large enough to accurately represent the bulk properties of an actual crystal or amorphous material: surface effects will always be present. This problem is solved by implementing periodic boundary conditions, in which the simulation box is replicated through space in all directions; see Figure 3.1. The set of atom present in the box is thus surrounded by exact replicas of itself, *i.e.* periodic images. If an atom moves through a boundary on one side of the simulation box, so will its replica on the other side. This keeps the number of atoms in one box constant, and if the box has constant volume the simulation then preserves the density of the system, which can effect the

properties of the simulation, but much less than the surface effect would have done without the periodicity. An MD simulation should also follow the laws of thermodynamics. At equilibrium, it should have a specific temperature, volume, energy, density, pressure, heat capacity, *etc.* In statistical thermodynamics, this constitutes the state of the system; its *ensemble*. Since MD is a statistical mechanics method, an evaluation of these physical quantities can be made from the velocities and masses of the particles in the system, and MD can serve as a link between these atomic-level quantities and macroscopic properties. When performing an MD simulation model is retained. This ensemble then scales the velocities of the particles. Three different ensembles have been used here:

1. The microcanonical ensemble (NVE), which maintains the system under constant energy (E) and with constant number of particles (N) in a well-defined box with volume (V). This is appropriate during the initial equilibration phase of a simulation.
2. The isothermal-isobaric ensemble (NPT), where temperature and pressure are kept constant. This is normally the best model of the experimental conditions.
3. The canonical ensemble (NVT), where volume and temperature are kept constant. This ensemble has been used for most simulations, so that comparisons can be made with experimental data from structures with fixed dimensions.

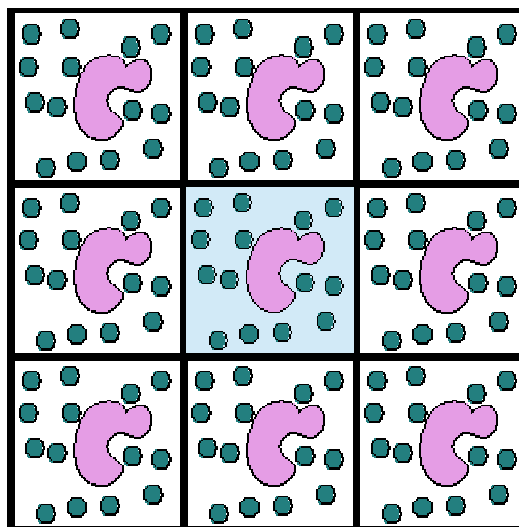


Figure 3.1 Periodic boundary conditions in Molecular Dynamics (Computational chemistry list, www, 1996).

One factor that impacts total CPU time required by a simulation is the size of the integration time-step (Δt). This is the time length between evaluations of the potential. The time-step must be chosen small enough to avoid discretization errors (*i.e.* smaller than the fastest vibrational frequency in the system). Typical time-step for classical MD is in the order of 1 femtosecond (10^{-15} s). This value may be extended by using algorithms such as *SHAKE*, which fix the vibrations of the fastest atoms (*e.g.* hydrogens) into place (Wikipedia, www, 2008). The SHAKE algorithm, a modification of the Verlet algorithm, has become the standard approach for doing Molecular Dynamics with fixed bond lengths. It can also be used to hold angles fixed, but this is less common. It works well for time-step up to 5 fs, thereby enabling a five-fold speedup in computational time as long as the process of iteratively solving the constraint equations does not consume too much time (Mathiowetz, www, 1994).

3.2.4 Structure and Dynamics from MD Simulations

The statistics provided by the MD simulations have been used to calculate different properties relating to structural and dynamical behavior. This analysis and its chemical interpretation has been the major part of this thesis work.

3.2.4.1 Radial Distribution Function (RDF)

One of the most important properties extracted from the MD simulation is the pair radial distribution function (RDF). It is a function, usually written $g_{a...b}(r)$, which presents the probability of finding a particle of type b at a distance r from particle of type a . In a perfect crystal without thermal motion, the RDF would appear as periodically sharp peaks, which gives information about the short-range order in the system.

The RDF can be calculated by counting the number of atom pairs within some distance range, and averaging this over a number of time-steps and particle pairs:

$$g_{ab}(r) = \frac{\sum_{k=1}^M N_k(r_{ab}, \Delta r)}{M \left(\frac{1}{2} N\right) \rho V(r_{ab}, \Delta r)} \quad (3.15)$$

where N_k is the number of atoms found at time k in a spherical shell of radius r and thickness Δr , and ρ is the average system density, N/V , of a given atom type.

Integrating this RDF over r gives the coordination number function (CNF), which is the average coordination number of particle type a to particle type b at distance r .

The RDF can be compared directly with experimental data from X-ray or neutron diffraction, and can thus be used as a check on the reliability of the potentials in many systems.

3.2.4.2 End-to-end Distance and Radius of Gyration

Since polymer molecules may in general assume an enormous number of spatial arrangements, descriptions of chain configuration are generally given in terms of statistical (ensemble) averages of some characteristic property. Two examples of parameters used to specify average global configuration are the distribution and moments of the end-to-end distance and the radius of gyration. The end-to-end distance, r , of a single chain may be defined by:

$$r = \sum_{i=1}^n l_i \quad (3.16)$$

where l_i denotes the vector along backbone bond i , and n denotes the number of backbone bonds in the molecule. The radius of gyration, s , is defined as the root mean square distance of the atoms in the molecule from their common center of mass, that is,

$$s^2 = \frac{\sum_{i=1}^N m_i s_i^2}{\sum_{i=1}^N m_i} \quad (3.17)$$

where s_i denotes the distance of atom i from the center of mass, and N denotes the total number of atoms.

In polymer physics, the radius of gyration is used to describe the dimensions of a polymer chain. Since the chain conformations of a polymer sample are quasi infinite in number and constantly change over time, the “radius of gyration” discussed in polymer physics must usually be understood as a mean over all polymer molecules of the sample and over time. That is, the radius of gyration which is measured is an *average* over time or ensemble. One reason that the radius of gyration is an interesting property is that it can be determined experimentally with static light scattering as well as with small angle neutron- and X-ray scattering. This allows theoretical polymer physicists to check their models against reality. The hydrodynamic radius is numerically similar, and can be measured with size exclusion chromatography.

Local chain geometry is frequently characterized by measurements of valence and dihedral angle distributions. The latter, whose values are essentially determined by a combination of packing effects and local intramolecular interactions are strongly correlated with global dimensions, and are often experimentally measurable.

3.2.4.3 Bond Angle and Dihedral Angle

In a chemically complex system such as $\text{LiPF}_6\text{PEO}_6$ average atomic distances calculated as RDF can be too rough a measurement to capture all the structural information available. The spatial arrangement of atoms can also be of major interest, and can be obtained throughout by calculating bond angle and dihedral angle distributions in the crystallographic asymmetric unit. The total distribution of all bond and dihedral angles contains all the information we need on the polymer configuration. Figure 3.2 shows the geometry of a simple chain molecule.

Plotting especially the dihedral angles in this way gives group information for the simulated system, which can be related to the crystallographically determined space group. The appearance of new peaks indicates some new repeat unit.

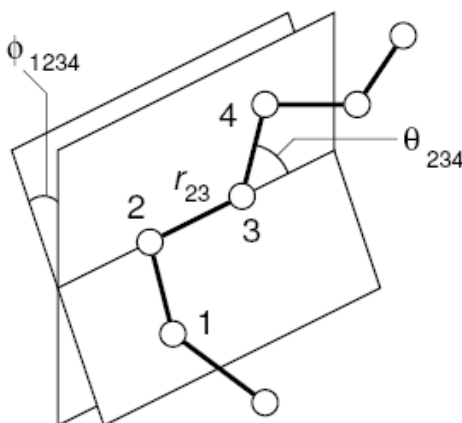


Figure 3.2 Geometry of a simple chain molecule, illustrating the definition of interatomic distance r_{23} , bend angle θ_{234} , and torsion angle ϕ_{1234} (Allen, www, 2004).

3.2.4.4 Density Profile

A local density profile, $\rho(z)$ is defined as the average number of atoms in a slice of width Δz , which is parallel to the solid substrate. The proper choice of the width Δz of a slice is a trade-off between two factors. First, a very small width results in too few particles in each slice, and therefore one observes large statistical errors and data scattering. Second, a very large width of a slice will not show the actual dependence of the properties on the distance from the surface. Hence, a balance between those two requirements must be achieved (Sorkin, www, 2003).

3.2.4.5 Mean Square Displacement (MSD) and Diffusion Coefficient (D)

The self diffusion coefficient, D of an atom undergoing random Brownian motion in three dimensions can be evaluated from the limiting slope of the mean square displacement as a function of time, that is:

$$D_{\alpha} = \frac{1}{6N_{\alpha}} \lim_{t \rightarrow \infty} \frac{d}{dt} \sum_{i=1}^{N_{\alpha}} \langle [r_i(t) - r_i(0)]^2 \rangle \quad (3.18)$$

where r_i denotes the position vector of atom α , and the angular brackets denote averaging over all choices of time origin within a dynamics trajectory.

An alternative method for obtaining the self diffusion coefficient involves making use of the velocity autocorrelation function. In this case, D is given by:

$$D = \frac{1}{3} \int_0^{\infty} \langle v_i(t) \cdot v_i(0) \rangle dt \quad (3.19)$$

where $v_i(t)$ denotes the velocity of atom i at time t . Again, averaging is performed over all time origins in the trajectory. This equation is an example of the Green-Kubo formalism for calculating transport coefficients from time correlation functions measured on an *equilibrium* system.

3.2.5 MD vs. Experiment

It has been argued that Computational Chemistry is both “theory” and “experiment”: “theory” since clearly no measurements are made on a real system, and “experiment” since the potentials used are often based on experimental data on simple systems. MD is indeed often referred to as a “computer experiment”.

Today, most computational chemists would probably say that computation is neither theory nor experiment, but rather a third leg on the chemical body – both to test theory and to interpret experiment; alternatively, to perform “experiments” on systems inaccessible to normal experimental techniques.

This discussion puts focus on the relationship between MD and experiment. Experimentalists interpret their data using theories and models – they do not anticipate reality. Experimental data can often be interpreted in several ways, sometimes even within the same theoretical context. Not rarely are data interpreted on the basis of incorrect or inappropriate theory for the system under study. The interpretation of experimental results is not a search for biblical “truth”, just like the computational chemist, the experimentalists use models to make their interpretation, thereby creating a gap between themselves and reality. MD can indeed sometimes be as good (or bad) a method as experiment for modeling this reality.

3.3 Monte Carlo (MC)

The Monte Carlo simulation is the simulation technique that gathers samples in a random way. As the name of “Monte Carlo” implies, the Monte Carlo simulation uses random numbers for making decision during the simulation. In terms of molecular mechanics, the Monte Carlo provides another way to explore a conformational space. While Molecular Dynamics can visit a conformational state in a deterministic way by solving Newtonian equations of state, Monte Carlo simulation can find a conformational state in a stochastic way by generating random numbers.

With a given potential like Equation 3.20, the simulation involves a successive energy evaluation to make a decision for acceptance of a move attempt which is chosen randomly.

$$V_{total} = \underbrace{V(r)_{bond} + V(\theta)_{angle} + V(\phi)_{torsion} + V(\chi)_{out-of-plane}}_{V_{bonded}} + \underbrace{V(r)_{vdw} + V(r)_{elec}}_{V_{non-bonded}} \quad (3.20)$$

The decision is accomplished by Metropolis algorithm (Metropolis *et al.*, 1953) in the most cases, which has the following criteria.

$$\Delta E = V(r)_{new} - V(r)_{old} \leq 0 \quad \text{accepted}$$

$$\Delta E = V(r)_{new} - V(r)_{old} > 0 \text{ AND } \exp(-\Delta E / kT) \geq rand(0,1) \quad \text{accepted} \quad (3.21)$$

$$\Delta E = V(r)_{new} - V(r)_{old} > 0 \text{ AND } \exp(-\Delta E / kT) < rand(0,1) \quad \text{rejected}$$

If the new state is in a lower energy state, the new state replaces the previous state. If the new state is in a higher energy state, the decision is based on the energy difference between two states. For the decision procedure, Monte Carlo simulation allows a system to move to higher energy state. The probability to overcome the higher energy barrier depends on the energy difference between the new attempt and the current conformation. By doing so, Monte Carlo simulation explores the conformational space to calculate the ensemble averaged properties, while Molecular Dynamics simulation deals with time averaged properties. Both averaged properties should be same through the ergodic hypothesis.

Much effort has drawn attention to increasing the computational efficiency of Monte Carlo simulation. One of the efforts is to run the simulation on a lattice, which reduces the floating number calculation. Another way to gain speed in the Monte Carlo simulation is to use an efficient move algorithm that allows the faster relaxation or equilibration. Many beads can move at a single move attempt. The computational time of the lattice simulation based on Monte Carlo method is proportional to the power of 1 to 2 depending on the quality of the potential energy function.

3.3.1 Computer Simulations for Polymers and Polymer Surfaces

3.3.1.1 Computer Simulations of Polymers

A polymer is different from small molecules due to its large size which spans a wide range of molecular motions from small local fluctuation to center of mass movement of the whole molecules. Accordingly, the corresponding time spectrum of the molecular motions is in the range of nanoseconds (10^{-9} s) to the order of seconds (10^0 s). As illustrated in Figure 3.3, the four different methods have their

own territories in terms of the time and length scale, which are mainly given by the quality of each method that determines the required computational resources.

Considering the broadness of the time and length scales of polymer motions, a simulation method can be specified according to the nature of the problem. Quantum simulation that is considered to be an extreme with great details has been tried to understand the specific interactions and chemical kinetics for the polymerization reactions. The other extreme Quantitative Structure Property Relationship (QSPR) has also been the useful tool to give an idea of polymer bulk property without a severe computation. Between two extremes, molecular mechanics simulation can give conformation dependent properties of polymers because the simulation searches the conformational space. Among the three methods (*i.e.* molecular minimization, Molecular Dynamics and Monte Carlo) of molecular mechanics, the molecular minimization is relatively less important than the other two methods in polymer. This is because the minimization is limited to only several representative local minima and provides only static information: for biomaterial like a protein, the minimization has been widely used because the conformation corresponding to the global minimum state is often the most probable conformation that defines the properties. As a result, Molecular Dynamics and Monte Carlo simulations have drawn much more attention for the polymer area.

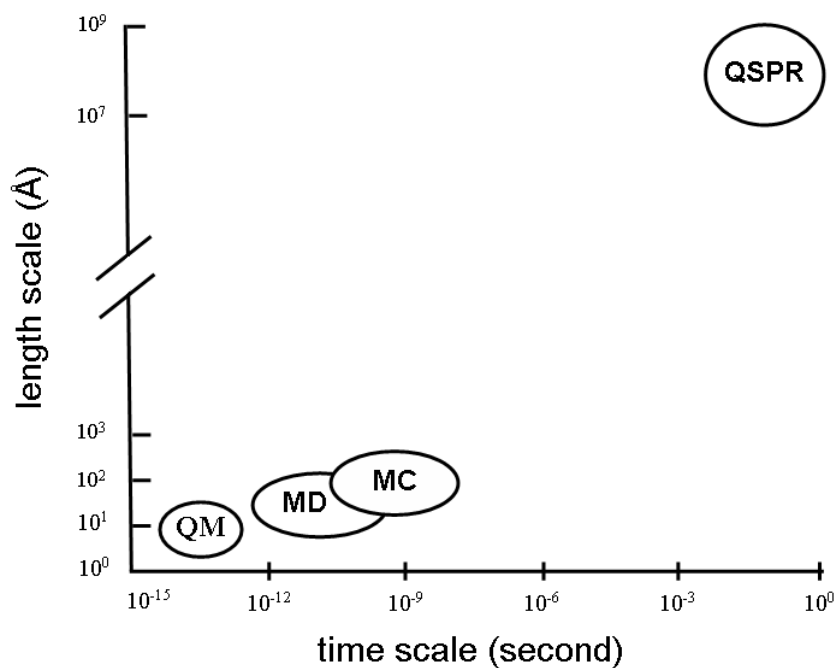


Figure 3.3 The time and length regimes for various simulation methods.

However, the accessible time and length regimes of the two methods are insufficient to understand all polymer chain behavior. For example, the fluctuation or relaxation of the end-to-end distance of a long polymer chain can be of the order of seconds, which is not easily accessible by Molecular Dynamics and Monte Carlo simulations with a detailed molecular description, using the current computer technology as shown in Figure 3.3. Since the large scale relaxation is related to the long-time dynamics of polymer chain, the chain diffusion is another difficult property to calculate by computer simulation.

Therefore, effort in computer simulation of polymer system has been directed toward gaining the speed-up of the simulations, which enable reaching a larger time regime or a longer length regime. The effort can be categorized into several ways; The first one is to simplify the potential energy function which governs simulation, the second one is to reduce the number of particles, but still keeping much chemical details, the third one is to increase the efficiency of relaxation through adopting large scale movement in a integer based lattice, which is computationally very efficient since the arithmetic during the simulation is based on not real numbers but integer numbers. The third one is more likely for the Monte Carlo simulation because Monte Carlo method deals with the static properties through the ensemble average.

For the simplification of potential energy function, fortunately, many polymeric materials, especially common polymers widely used in our real lives, are composed of chemically identical monomeric units which do not have specific functional groups. Therefore, a polymer chain has been modeled as a necklace of many Lennard-Jones particles through bond connectivity.

Another direction in the development of computer simulation is to reduce the number of degree freedoms, which greatly reduces the computational cost. This approach is generally called “united atom model” in Molecular Dynamics simulation and “coarse-grained model” in Monte Carlo simulation. The united atom model can be considered as an intermediate approach between the fully atomistic model and the LJ fluid model. In many Molecular Dynamics simulations based on the united atom model, it is found that the potential energy function still holds many chemical details which are bond stretching potential, angle potential, and torsional

angle potential. The use of the detailed potential energy functions makes the Molecular Dynamics simulation based on the united atom model explore a conformational space. The effort using the united atom model has been focused to increase the reliability of the simulation results compared to the experiment. Therefore, the method has not been applied to long chains although the method turns out to be in very good accordance with experimental results for short chains in terms of the local and global scale behaviors. The exploring a long chain system remains as a challenging work using the united atom model, which must happen prior to the fully atomistic model.

The other direction for the speed-up of simulation is to design a lattice based simulation model, which allows the simulation to achieve a faster equilibration by a large-scale move and by the integer number arithmetic relative to real number arithmetic. The lattice model requires a coarse-graining of a polymer chain. Unlike the united atom Molecular Dynamics, the lattice based simulation has an inherent limitation to build a proper internal coordinates for a chain closer to a real polymer chain because the particle position is limited to the lattice point. For example, assigning proper internal coordinate such as bond angle and torsion angle to a polymer chain in a cubic lattice seems to be difficult. And a move of particles in a lattice also follows an unrealistic pathway. As a result, the lattice simulation is more likely combined with a Monte Carlo simulation, incorporating low quality of potential energy function.

One representative Monte Carlo simulation is the bond fluctuation model (Deutsch and Binder, 1991; Paul, Binder, Kremer, and Heerman, 1991; Baschnagel, Paul, Tries, and Binder, 1998), which is a more efficient method compared to simple cubic lattice model in that it allows a better flexibility for the bond length and bond angle; it would be more appropriate to say step length and angle between two successive steps. Another way to give a more flexibility to span a conformational space is to use a high coordination lattice like diamond lattice (Rapold and Mattice, 1995).

In a lattice based Monte Carlo simulation, the computational cost can be largely reduced by using large-scale moves. As shown in Figure 3.4, there are several elementary moves such as kink jump, crank shaft rotation, and end rotation known as the standard Verdier-Stockmayer type move (Verdier and Stockmayer, 1962). In addition to the basic moves, the reptative move (Fried and Binder, 1991), the end-bridging move, and the concerted rotation move (Pant and Theodorou, 1995) can be useful for the faster relaxation and can deal with a more delicate situation like a polydisperse system, as illustrated in Figure 3.5.

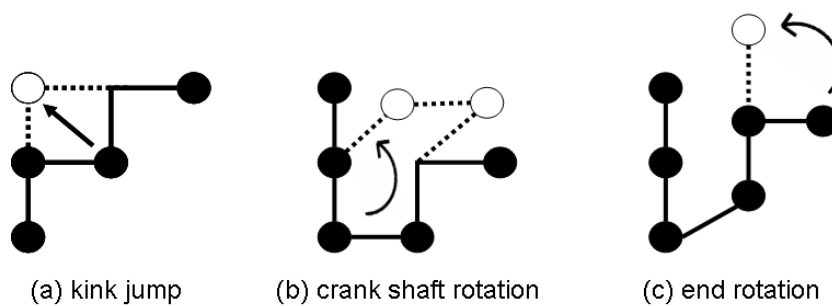


Figure 3.4 Basic elementary moves based on the standard Verdier-Stockmayer type model.

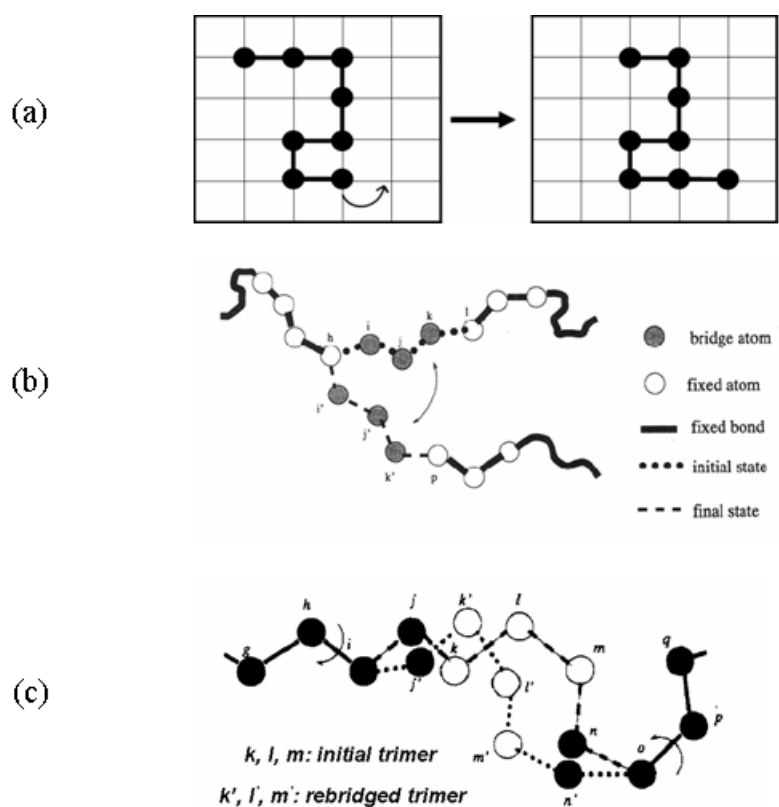


Figure 3.5 Collective moves (a) reptative move (b) end-bridge move (c) concerted rotation.

3.3.1.2 Computer Simulation of Polymer Surfaces

Polymer surfaces and interfaces play an important role in polymer technology through the processes of wetting, adsorption, and adhesion, and through their effects on the kinetics of phase separation and the mechanical mixing of molten polymers (Sanchez, ed., 1992). When polymers lie on different surfaces, the chain configuration and the dynamics will have remarkable changes compared with those in the bulk. For example, the chain configuration on the surface regions will be very different from those in the bulk region and no longer obey the Gaussian distribution; the diffusion and inter-diffusion will be enhanced or reduced due to the different natures of surfaces and interfaces. Moreover, the properties of polymers on the surface depend not only on the nature of the surface but also on the nature of the material. For a specific material, the nature of surfaces will affect the ordering, chain configuration, morphology, dynamic of the system, and so on.

Several kinds of polymer surfaces and interfaces (including physically existing surface and mathematically abstracted surface) are interesting in the polymer processing, experimental study, and theoretical investigation. They are the polymer-polymer interface, polymer-small molecule interface, polymer confined between hard walls (with or without interaction with the hard walls), polymer adsorbed on one substrate in one side and exposed to air or vacuum in the other side, and polymer exposed to the air or vacuum surfaces on both sides (the so-called free-standing thin film). The schematic representations of five kinds of interfaces or surfaces are illustrated in Figure 3.6.

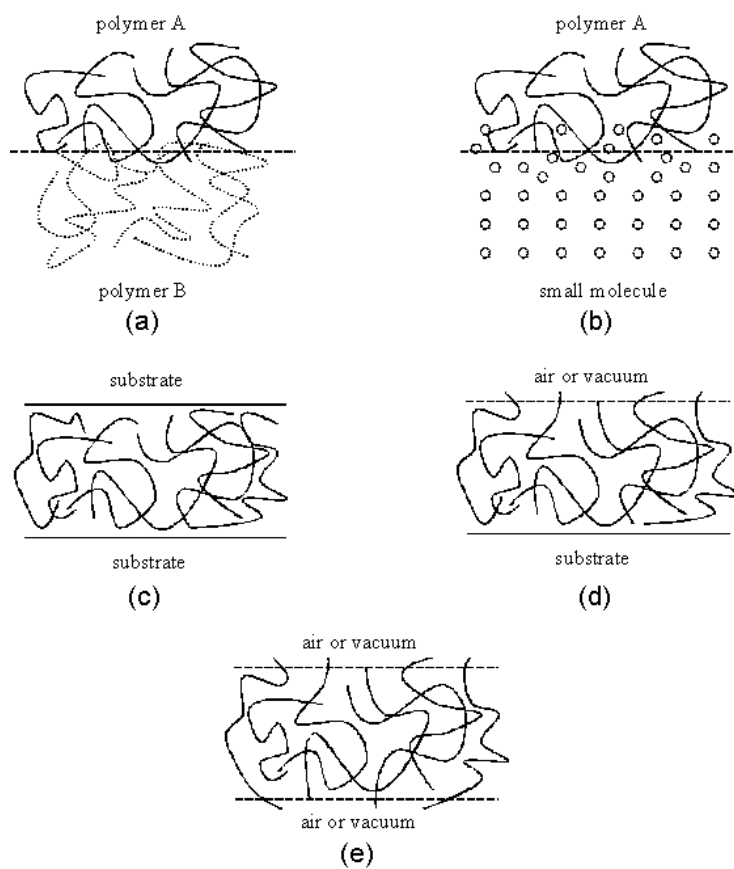


Figure 3.6 Five kinds of polymer interfaces and surfaces: (a) polymer-polymer interface, (b) polymer-small molecules interface, (c) polymer confined between two substrates, (d) polymer confined between a substrate and an air or vacuum surface, and (e) free-standing polymer thin film.

A host of Molecular Dynamics simulations (Bitsanis and Hadziioaou, 1990; Mansfield and Theodorou, 1990; Hentschke, Schürmann, and Rabe, 1992) and Monte Carlo simulations (Madden, 1987; Mansfield and Theodorou, 1989; Kumar, Vacatello, and Yoon, 1990; Ribarsky and Landman, 1992; Lai, 1995; Baschnagel and Binder, 1995) have been performed to scrutinize the effects of a variety of surfaces on static and dynamics properties of the polymer chains; free surface, surface near a solid wall, confined geometry and polymer-polymer interface. In the area of Molecular Dynamics simulation, the pioneering work was done by Mansfield and Theodorou (1990) on freely standing films of a glassy atactic polypropylene composed of 75 monomeric units at maximum. Their observations have detailed molecular features; sigmoidal interfacial profile, segregation of methyl groups at the free surface, perpendicular ordering to the surface plane of C-H and C-CH₃ bonds at the free surface, chain flattening near the free surface. After their work, polymer surfaces or interfaces created by other boundary situations attracted the use of Molecular Dynamics simulations. Some of interesting works can be summarized; the physisorbed alkane chain on graphite surface by Hentschke *et al.* (1992), the collapse of a single polybutadiene chain in vacuum state by Zhan *et al.* (1994), the influence of solid wall interaction on the structure and dynamics of hexadecane melts (*n*-C₁₆H₃₄) by Winkler *et al.* (1996), the behavior of confined polymer melts in a shear flow by Khare *et al.* (1996), and the binary hydrocarbon mixture of benzene and *n*-heptane near an adsorbing wall by Fodi *et al.* (1998). Surprisingly, after 20 years progress of the computer technology, the chain size currently under study in polymer surface area by Molecular Dynamics does not exceed much more than that of the earlier polypropylene. This would be because the development of the forcefield for the

interaction from a substrate requires another extensive work and the evaluation of the potential term from the interaction seems to be strenuous. Therefore, there has been a propensity to find more reliable and exact solutions for molecular system until now.

In the case of the Monte Carlo simulation, the length scale which is accessible by the simulation has been increased dramatically along with the number of Monte Carlo steps. The increase is observed in the total size of the polymer system as well as the size of a single molecule. A recent work of Werner *et al.* (1999) covered the study of surface effect on interfacial properties on a binary polymer melt confined between two parallel walls using extensive Monte Carlo simulation. The size of the polymer chain in their study corresponds to a degree of polymerization of the order 100 and the film thickness is comparable to 60 times of the radius of gyration (R_g) of the chain. With the progress, many macroscopic static properties have been understood, which include the short chain segregation near a solid surface, the interfacial width change on film thickness and so on.

In spite of the many successes of the Monte Carlo simulations, the models are still arbitrary to some extent because many of the models are based on coarse grained LJ particles. This coarse grained model has a drawback in understanding the chemical details and the conformation of a chain. Therefore, the understanding by the Monte Carlo simulation is limited to the phenomenological level. For example, the density is generally arbitrarily chosen in a Monte Carlo simulation for polymer. Considering that the density is represented by the thermodynamic equilibrium of a system, the understanding of thermodynamics obtained from a Monte Carlo simulation is also quite incomplete.

The drawbacks observed in both Molecular Dynamics and Monte Carlo simulations have motivated to develop a compromising model. The model should be able to simulate a relatively long and large system, but not lose much detail of the chemical nature and conformational information.

3.3.2 Monte Carlo Simulation on a High Coordination Lattice

A coarse graining model in a lattice has the computational efficiency that comes from two reasons. The first one is the reduction of the evaluation of energy terms, which is generally proportional to the square of the number of particles because many energetic terms are two-body potentials. The second reason is that the positions of particles during simulation can be stored as integers, which reduces the number of instructions done by a central processing unit (CPU) and memory usage compared to the real number operation in off-lattice simulation. As a result of the efficiency, the method enables running a simulation in a large scale, which is required for polymer simulation. As often is the case, the pros come with the cons. Due to the coarse graining, the detailed chemical information such as the chemical nature of the coarse-grained particle (bead) and the nature of bond between the two beads disappears. The drawback would not be an important issue when a polymer chain is expressed by a collective set of simple beads. In the bulk state of polyolefin, the simplification works well with only the topological consideration. However, many variables are coupled with each other to make the understanding of a polymer surface difficult. The decoupling of the effect of the variables or the ruling-out of an effect of a variable using a computer simulation requires a detailed description of a polymer chain embodied in the simulation as well as its applicability to the large-scale system.

3.3.2.1 Coarse Graining into Rotational Isomeric State Model

Often the energy state of a molecule can be described by a sum of energetic contributions of internal coordinates and non-bonded interactions, as in Equation 3.20. Among them, the bond stretching and angle bending terms are so strong, because of large force constants, that they do not vary much with time, staying at the most probable bond length and bond angle. Since computational efficiency is indispensable for a polymer simulation, these two terms are neglected in most cases. Accordingly, a property of a polymer chain can not be only dependent on the remaining energy terms, torsional energy and non-bonded energy. Furthermore, if a polymer chain is not perturbed by the existence of others, the importance of the long-range interaction is diminished. In that case, the partition function of a single chain can be expressed by only torsional partition function or conformational partition function as follows.

$$Z = \int_{\phi_1} \dots \int_{\phi_n} \exp\left(-\frac{E_{\phi_1 \dots \phi_n}}{kT}\right) d\phi_1 \dots d\phi_n \quad (3.22)$$

Then, the average of a property, $\langle A \rangle$, can be written as,

$$\langle A \rangle = Z^{-1} \int_{\phi_1} \dots \int_{\phi_n} \exp\left(-\frac{E_{\phi_1 \dots \phi_n}}{kT}\right) A(\phi_1 \dots \phi_n) d\phi_1 \dots d\phi_n \quad (3.23)$$

The continuous torsional states can be grouped to have several discrete states. This assumption is reasonable because discrete torsional states are separated by an activation barrier. The torsional states are called “rotational isomeric state (RIS)”. With the discrete torsional states, the conformational partition function of Equation 3.22 can be rewritten as the summation over the discrete conformational space.

$$Z = \sum_{\phi_1} \dots \sum_{\phi_n} \exp\left(\frac{-E_{\phi_1 \dots \phi_n}}{kT}\right) \quad (3.24)$$

The RIS model (Mattice and Suter, 1994) is a coarse grained model, which only considers the discrete rotational isomeric states with other internal coordinates frozen. Schematically, the mapping from a realistic chain to a RIS chain is illustrated in Figure 3.7. For a polyethylene (PE) chain, which is the model polymer chain in this study, Abe *et al.* (1966) presented a RIS model with three torsional states of $\phi_{CCCC} = 180^\circ$ (*trans*; t), 60° (*gauche plus*; g^+), and -60° (*gauche minus*; g^-) at the fixed bond length $l_{CC} = 1.54 \text{ \AA}$ and the fixed bond angle $\theta_{CCC} = 112^\circ$. Based on the model, a linear polyethylene chain can be mapped onto the tetrahedral lattice very successfully except for the very small bond angle mismatch. In this mapping, each occupied lattice site of the tetrahedral lattice represents a single $-\text{CH}_2-$ group of the polyethylene chain. The bond between two neighboring occupied lattice sites can be one of three rotational states; *trans* (t), *gauche*⁺ (g^+), or *gauche*⁻ (g^-)

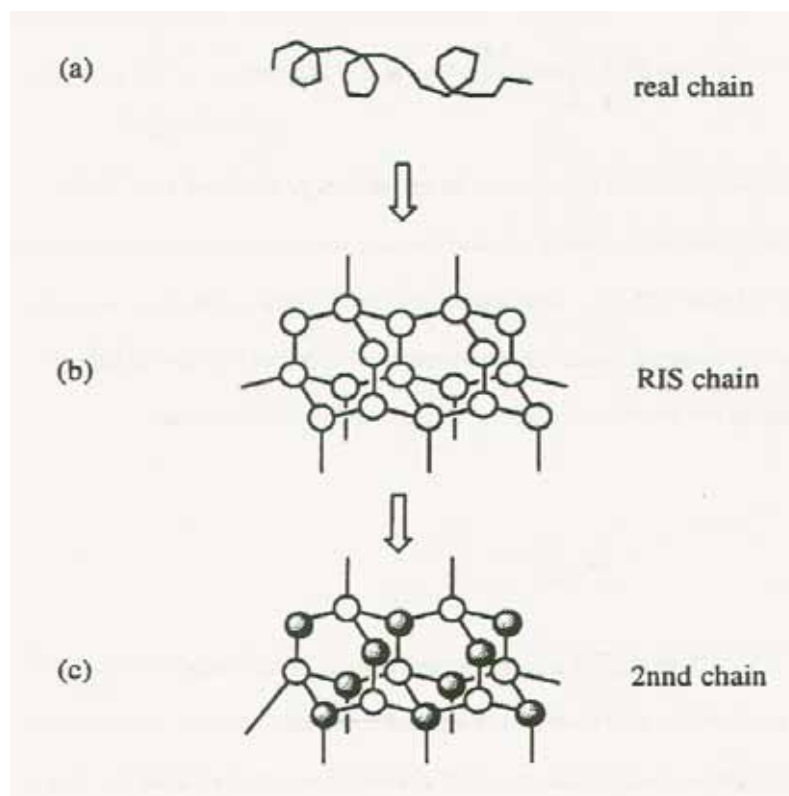


Figure 3.7 Example of the mapping of a real chain into lattice by coarse graining. The degree of coarse graining increases from (a) to (c). (a) continuous space, (b) space available with a single bond length, tetrahedral bond angle, and $\phi = 180^\circ, \pm 60^\circ$, (c) rejection of alternate sites from (b).

3.3.2.2 Further Coarse Graining

A further coarse-grained lattice from the RIS model for PE chain can be obtained by discarding every second site from the tetrahedral lattice. This process corresponds to the coarse graining from Figure 3.7 (b) to Figure 3.7 (c). The coarse graining generates a slanted cubic cell whose length is 2.5 \AA in a , b , and c directions, and the angles between any two unit vectors are 60° . The modification produces a coordination number of 12 (or $10i^2 + 2$ sites in shell i), which is higher than that of the

tetrahedral lattice. The high coordination number provides a flexibility to define a rotational state in the lattice. The new lattice is identical to the closest packing of uniform hard spheres. The high coordination lattice is named as the “second nearest neighbor diamond (2nd) lattice”. Each occupied site in this model represents an ethylene ($-\text{CH}_2-\text{CH}_2-$) group. Figure 3.8 shows the structure of the 2nd lattice and the twelve coordination sites around a central bead. This coarse-grained lattice provides a better computational efficiency due to the reductions in the number of particles and in the number of conformational states, which facilitates its application to the fairly large polymeric systems. More detailed information about the 2nd lattice is found elsewhere (Balijepalli and Rutledge, 1998).

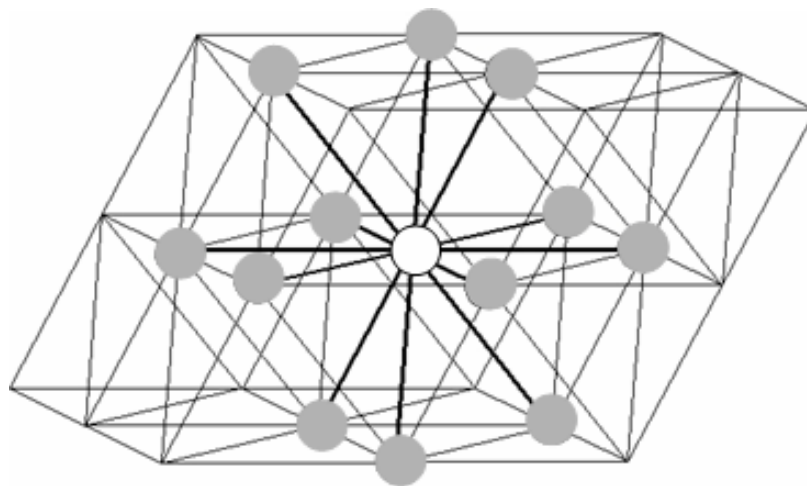


Figure 3.8 The 2nd lattice. The gray spheres represent the possible twelve coordination lattice sites around a central bead (open circle).

3.3.2.3 Conventional RIS Formalism

In the RIS scheme for n -alkane homologs, the first approximation is to handle the rotatable bonds independently. On the assumption that a rotational state of a bond is not affected by other bonds and defined solely by the first order interaction, the conformational energy of a chain will be

$$E\{\phi\} = \sum_i E_i(\phi_i) = \sum_i E_{\xi,i} \quad (3.25)$$

where ξ denotes the rotational state of bond i . The statistical weights $u_{\xi,i}$ can be defined by the Boltzmann probability, which means the relative population of the ξ state in the i th bond.

$$u_{\xi,i} = \exp(-E_{\xi,i} / RT) \quad (3.26)$$

Then, the conformational partition function of a chain Z as a whole is given by

$$Z = \prod_i \sum_{\xi} u_{\xi,i} = \prod_i z_i \quad (3.27)$$

If the rotor has three rotational states as shown in Figure 3.9 (a), which is a proper choice for the n -alkane homologs, the Z is given by $(1+2\sigma)^{n-2}$ for a linear alkane or PE chain with n carbon, where 1 and σ correspond to the statistical weights of *trans* and *gauche* states, respectively.

The first approximation, independent bonds approximation, is invalid in real situation because of the second order interaction known as pentane effect. The interdependence of bonds destroys the degeneracy of the energy state of the *gauche-gauche* (gg) conformation and splits into g^+g^+ and g^+g^- or g^-g^- and g^+g^- . As a result, the total energy of a chain with the interdependent bonds given by

$$E\{\phi\} = \sum_i E_i(\phi_{i-1}, \phi_i) = \sum_i E_{\xi\eta,i} \quad (3.28)$$

where $\xi_{\eta,i}$ means the $(i-1)$ th bond is in ξ state and i th bond is in η state. The statistical weights corresponding to $E_{\xi\eta,i}$ can be written as a matrix form as

$$U_i = [u_{\xi\eta}]_i \quad (3.29)$$

The conventional RIS model for PE of Abe *et al.* (1966) is defined by the statistical weight for two successive rotatable internal bonds,

$$U_i = \begin{bmatrix} 1 & \sigma & \sigma \\ 1 & \sigma & \sigma\omega \\ 1 & \sigma\omega & \sigma \end{bmatrix} \quad (3.30)$$

where σ and ω are the first- and the second-order interaction parameters and the rows are indexed by the states of $(i-1)$ th bond and the columns are indexed by the states of i th bond. The orders of indexing are t , g^+ , and g^- . Then, the total conformational partition function will be

$$Z = \prod_i U_i \quad (3.31)$$

In a Monte Carlo simulation using a RIS scheme, a move attempt can change the rotational states of the chain which is affected by the move. The change enters the Metropolis evaluation (Metropolis *et al.*, 1953) to decide to accept or reject the move attempt. This decision can be simply done by obtaining bond probabilities from the statistical weights.

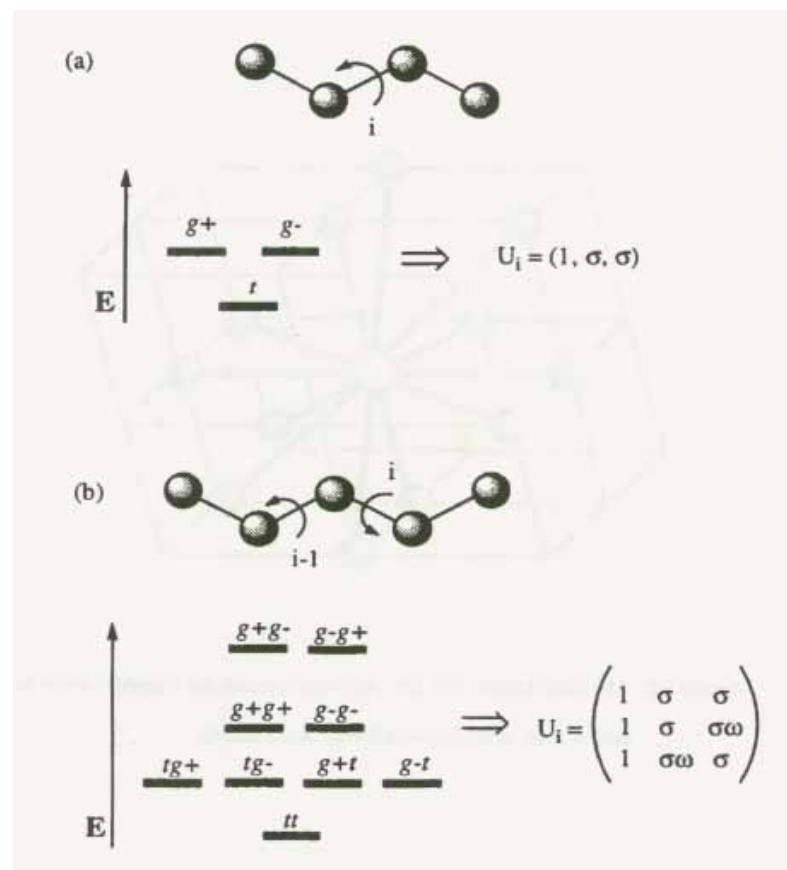


Figure 3.9 The rotational states of a linear chain and corresponding statistical weights (a) independent bond (b) interdependent bond.

3.3.2.4 RIS Formalism for 2nd Chain

The two successive bonds are contracted into one virtual bond between two neighboring beads in the 2nd lattice. The formalism of the RIS model of the virtual bonds for the coarse-grained chain should be modified. A virtual rotor in the 2nd frame, as shown in Figure 3.10, contains four successive rotors corresponding to *n*-heptane in the original RIS frame. The detailed description of *n*-heptane at the same place, which requires a 9×9 statistical weight matrix, is given by

$$U = \begin{bmatrix} 1 & \sigma & \sigma & \sigma & \sigma & \sigma^2 & \sigma^2 & \sigma^2 \omega & \sigma^2 \omega \\ 1 & \sigma & \sigma & \sigma & \sigma \omega & \sigma^2 & \sigma^2 \omega & \sigma^2 \omega & \sigma^2 \omega^2 \\ 1 & \sigma & \sigma & \sigma \omega & \sigma & \sigma^2 \omega & \sigma^2 & \sigma^2 \omega^2 & \sigma^2 \omega \\ 1 & \sigma & \sigma & \sigma & \sigma & \sigma^2 & \sigma^2 & \sigma^2 \omega & \sigma^2 \omega \\ 1 & \sigma & \sigma & \sigma & \sigma & \sigma^2 & \sigma^2 & \sigma^2 \omega & \sigma^2 \omega \\ 1 & \sigma & \sigma & \sigma & \sigma \omega & \sigma^2 & \sigma^2 \omega & \sigma^2 \omega & \sigma^2 \omega^2 \\ 1 & \sigma & \sigma & \sigma \omega & \sigma & \sigma^2 \omega & \sigma^2 & \sigma^2 \omega^2 & \sigma^2 \omega \\ 1 & \sigma & \sigma & \sigma \omega & \sigma & \sigma^2 \omega & \sigma^2 & \sigma^2 \omega^2 & \sigma^2 \omega \\ 1 & \sigma & \sigma & \sigma & \sigma \omega & \sigma^2 & \sigma^2 \omega & \sigma^2 \omega & \sigma^2 \omega^2 \end{bmatrix} \quad (3.32)$$

The row represents 1 and 2 rotors and the column represents 3 and 4 rotors in Figure 3.10 (a). The order of the rotational states of the rows and columns are tt , tg^+ , tg^- , g^+t , g^-t , g^+g^+ , g^-g^- , g^+g^- , g^-g^+ . By the nature of the coarse graining, several details of conformational information are missing in such a way that some torsional states are no longer distinguishable in the coarse-grained chain. Then, Equation 3.32 can be modified into a simpler form with the modified statistical weights, a , b , and c , which are obtained from the geometric mean ($a = \sigma \omega^{1/8}$, $b = \sigma \omega^{1/4}$, $c = \sigma^2 \omega^{1/2}$).

$$U = \begin{bmatrix} 1 & \sigma & \sigma & \sigma & \sigma & \sigma^2 & \sigma^2 & \sigma^2\omega & \sigma^2\omega \\ 1 & a & a & a & a & b\sigma & b\sigma & b\sigma\omega & b\sigma\omega \\ 1 & a & a & a & a & b\sigma & b\sigma & b\sigma\omega & b\sigma\omega \\ 1 & a & a & a & a & b\sigma & b\sigma & b\sigma\omega & b\sigma\omega \\ 1 & a & a & a & a & b\sigma & b\sigma & b\sigma\omega & b\sigma\omega \\ 1 & b & b & b & b & c & c & cb\omega & cb\omega \\ 1 & b & b & b & b & c & c & cb\omega & cb\omega \\ 1 & b & b & b & b & c & c & cb\omega & cb\omega \\ 1 & b & b & b & b & c & c & cb\omega & cb\omega \end{bmatrix} \quad (3.33)$$

Equation 3.33 can be reduced further because of the symmetry of the torsional potential energy (Rapold and Mattice, 1996).

$$U_{2nd} = \begin{bmatrix} 1 & 4\sigma & 2\sigma\sigma & 2\sigma\sigma\omega \\ 1 & 4a & 2\sigma b & 2\sigma\omega b \\ 1 & 4b & 2c & 2c\omega \\ 1 & 4b & 2c & 2c\omega \end{bmatrix} \quad (3.34)$$

Here, the rows define the lengths of the vectors connecting beads i and $i+2$ in Figure 3.10 (b) and the columns define the lengths of the vectors connecting bead $i+1$ and $i+3$. This reduction means that the rotational isomeric states in 2nd lattice can be categorized into four groups based on the vectors, which are specified by the distances between these two beads. The distances of 5.00 Å, 4.33 Å, 3.53 Å, and 2.50 Å correspond to the local conformations of A: tt , B: (tg^+, tg^-, g^+t, g^-t) , C: (g^+g^+, g^-g^-) , and D: (g^+g^-, g^-g^+) , respectively. Equation 3.34 can be condensed further to a 3×3 matrix with the modified indexing, A, B, and (C+D).

$$U_{2nd} = \begin{bmatrix} 1 & 4\sigma & 2\sigma^2(1+\omega) \\ 1 & 4a & 2b\sigma(1+\omega) \\ 1 & 4b & 2c(1+\omega) \end{bmatrix} \quad (3.35)$$

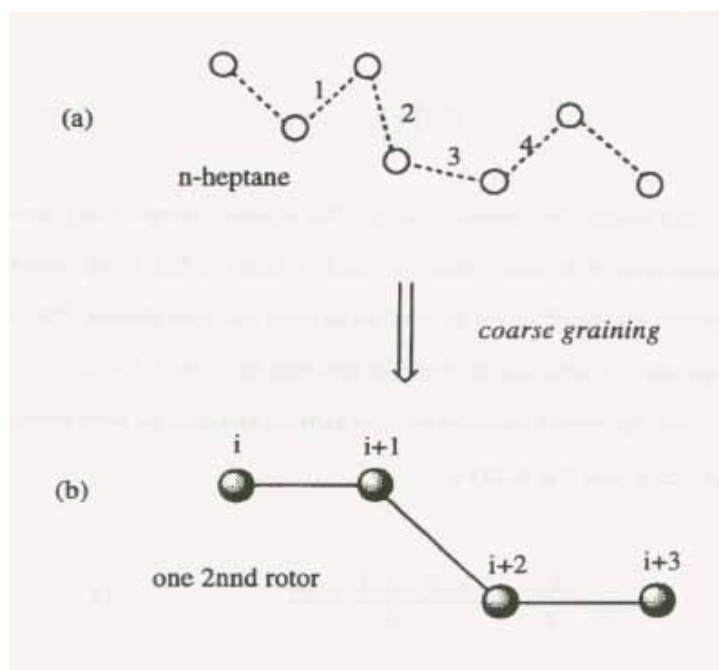


Figure 3.10 The coarse graining of *n*-heptane with 4 rotors to a single rotor in 2nd lattice: (a) *n*-heptane (b) 2nd chain equivalent to *n*-heptane.

3.3.2.5 Long-range Interactions

The incorporation of the rotational isomeric state model is not enough to describe the energetics of the melt system because the RIS model is a single chain model in the unperturbed state, θ state. The model only accounts for the short-range intermolecular interaction up to next nearest neighbor bonds on the 2nd lattice. For the remaining long-range intramolecular and intermolecular interaction, the Lennard-

Jones pair potential, $u(r)$, seems to be a reasonable choice since there are only dispersive interactions in a polyethylene melt. Including the long-range interaction, the total energy which will be used in Metropolis evaluation will be

$$E_{total} = E_{RIS} + E_{LJ} \quad (3.36)$$

The lattice representation of the continuous Lennard-Jones potential at the i th shell, u_i , is obtained from an averaged Mayer f-function which is used for the description of the second virial coefficient of a non-ideal gas. The interaction parameter at the i th shell is defined through following equation.

$$\exp\left(-\frac{u_i}{k_B T}\right) - 1 \equiv \bar{f}_i \quad (3.37)$$

The average Mayer f-function at the i th shell, \bar{f}_i , is obtained by integrating $u(r)$ over the cells in the i th shell.

$$\bar{f}_i = \frac{\int_{cell} f dr}{\int_{cell} dr} \quad (3.38)$$

$$f = \exp\left(-\frac{u(r)}{k_B T}\right) - 1 \quad (3.39)$$

The set of the interaction parameters for 2nd beads is derived from the Lennard-Jones potential for an ethylene molecule ($\text{CH}_2=\text{CH}_2$). Table 3.1 gives a set of interaction parameters obtained by the averaging method. The details about the long-range interaction is given by Cho *et al.* (Cho and Mattice, 1997).

Table 3.1 Long-range interaction shell energy obtained from the averaging process

Shell	Shell energy (kJ/mol) ^{a)}
1	12.501
2	0.084
3	-0.611
4	-0.137
5	-0.036

^{a)} In this example, the used LJ parameters are $\sigma = 4.2 \text{ \AA}$ and $\varepsilon/k = 205 \text{ K}$ and the interaction shell energies are derived at 443 K.

The single bead move is always employed in this study with the restriction that a chain can not pass through itself, as in a self-avoiding random walk. A randomly chosen bead can move to a vacant site in the first shell when the attempt does not change the bond length to its two bonded neighbors. Even though the relaxation or equilibration of a system is quite slow with the single bead move, the move provides the reliable dynamic properties at the time scale of Monte Carlo step (MCS). One MCS is defined as the simulation length when every bead in the system has attempted one move, on average.

3.3.2.6 Applications of the Method

Due to the computational efficiency that comes from the lattice characteristic and the chemical details that comes from the RIS characteristic, this Monte Carlo simulation method on the high coordination lattice has proven to be quite successful to visit many polymeric questions which show a large scale chain behavior. These include the successful mapping of polyoxyethylene and polythiaethylene onto the 2nd lattice (Doruker, Rapold, and Mattice, 1996), the restoring of PE chains to the fully atomistic chains (Doruker and Mattice, 1997), the simulation of the dynamics of PE in the bulk state, the simulation of PE thin film (Doruker and Mattice, 1998, 1999), the simulation of PE nanofibers (Vao-soongnern, Doruker, and Mattice, 2000), and the bulk simulation on polydisperse PE melt (Ozisk, Doruker, Mattice, and von Meerwall, 2000).

CHAPTER IV

MOLECULAR SIMULATION ANALYSIS AND X-RAY ABSORPTION MEASUREMENT OF POTASSIUM AND IODIDE IONS IN AQUEOUS SOLUTION AND POTASSIUM ION IN TETRAGLYME SOLUTION

4.1 Introduction

Solid polymer electrolytes (SPEs) are of great interest in the context of developing a variety of modern electrochemical applications such as high-energy-density batteries, fuel cells and electrochromic devices. SPEs usually comprise of alkali salts dissolved in a polymer matrix. The wide range of technological applications of SPEs has spurred attempts to determine the local structures around the ionic species of polymer solid electrolytes and understand the mechanism of ionic transport in polymer electrolytes. Poly(ethylene oxide), PEO is one of the most widely studied host polymer matrix because of its ability to solvate a variety of inorganic salts leading to polymer electrolytes with significant values of ionic conductivity. Oxygen atoms in PEO backbone play an important role in complexation with cations such as Li^+ and K^+ which makes decompositive salt to have better conductivity. In this chapter, the local structures of ionic species *i.e.* K^+ and I^- in aqueous solution are studied as the first step toward understanding more complicated ion/polymer systems.

Structural parameters can be calculated from experimental measurements, *ab initio* electronic structure calculations or numerical simulations such as Molecular Dynamics (MD). Figure 4.1 gives a qualitative picture of these structural parameters, the coordination number of the nearest neighbors, N ; Debye–Waller factor, σ^2 , which corresponds to the half-width of the peak in the radial distribution function, $g_{ij}(r)$; and the average distance between the central absorbing atom (i) and the surrounding atoms (j), which corresponds to the center of the peak, R_θ . The broken line depicts the (ideal) Gaussian peak centered at $R_{\theta,G}$, which in general, can be more symmetric and narrower than the real peak. This center is shifted compared to the one obtained experimentally, or even from the MD simulations. The coordination number can be calculated by direct integration of this first peak:

$$N = \rho \int_{r_1}^{r_2} 4\pi r^2 g_{ij}(r) dr \quad (4.1)$$

where r_1 and r_2 are the integration limits.

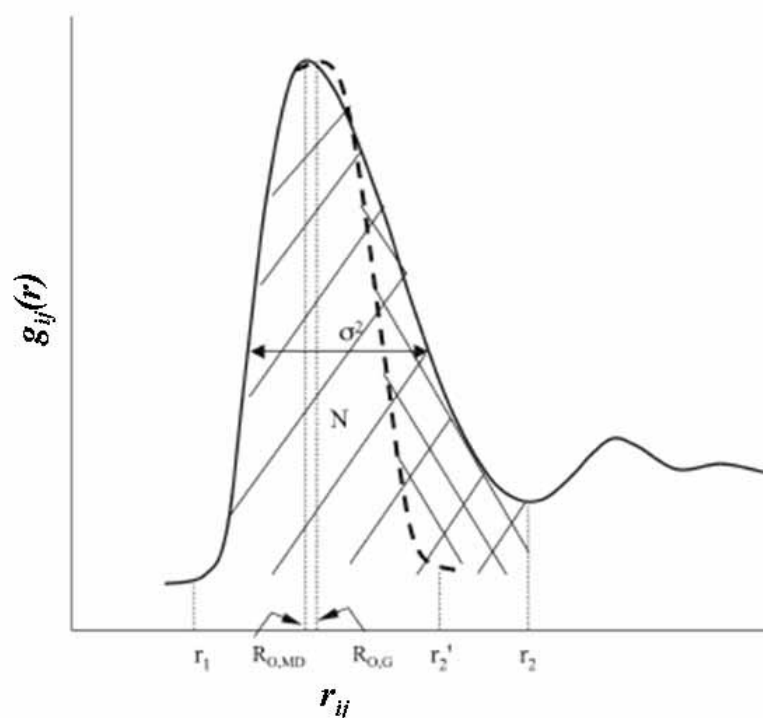


Figure 4.1 The fundamental quantities of ion solvation structure, coordination number N_0 (*area under curve*), Debye–Waller factor (half-width) σ^2 , center of peak, R_0 (Glezakou, Chen, Fulton, Schenter, and Dang, 2006).

In this work, MD simulations with COMPASS forcefield, extended X-ray absorption fine structure (EXAFS) spectroscopy, and the combination of MD simulation and EXAFS called “MD-EXAFS” method were employed to determine the solvation structures of K^+/H_2O and I^-/H_2O systems which are the simplified models for PEO/KI-based electrolytes. These models would give information on the solution structure by oxygen atoms which is the first step to understand more complicated molecules with $-(CH_2CH_2O)-$ repeating unit such as diglyme, triglyme, tetraglyme and long chain PEO.

In this work, COMPASS (Condensed-phase Optimized Molecular Potentials for Atomistic Simulation Studies) forcefield was used to describe the total interaction energy which has many terms as illustrated in Equation 4.2.

$$\begin{aligned}
E_{pot} = & \sum_b [K_2(b-b_0)^2 + K_3(b-b_0)^3 + K_4(b-b_0)^4] \tag{1} \\
& + \sum_\theta [H_2(\theta-\theta_0)^2 + H_3(\theta-\theta_0)^3 + H_4(\theta-\theta_0)^4] \tag{2} \\
& + \sum_\phi [V_1[1-\cos(\phi-\phi_1^0)] + V_2[1-\cos(2\phi-\phi_2^0)] + V_3[1-\cos(3\phi-\phi_3^0)]] \tag{3} \\
& + \sum_\chi K_\chi \chi^2 + \sum_b \sum_{b'} F_{bb'}(b-b_0)(b'-b_0') + \sum_\theta \sum_{\theta'} F_{\theta\theta'}(\theta-\theta_0)(\theta'-\theta_0') \tag{4, 5, 6} \\
& + \sum_b \sum_\theta F_{b\theta}(b-b_0)(\theta-\theta_0) + \sum_b \sum_\phi (b-b_0)[V_1 \cos \phi + V_2 \cos 2\phi + V_3 \cos 3\phi] \tag{7, 8} \\
& + \sum_{b'} \sum_\phi (b'-b_0')[V_1 \cos \phi + V_2 \cos 2\phi + V_3 \cos 3\phi] \tag{9} \\
& + \sum_\theta \sum_\phi (\theta-\theta_0)[V_1 \cos \phi + V_2 \cos 2\phi + V_3 \cos 3\phi] \tag{10} \\
& + \sum_\phi \sum_\theta \sum_{\theta'} K_{\phi\theta\theta'} \cos \phi (\theta-\theta_0)(\theta'-\theta_0') + \sum_{i>j} \frac{q_i q_j}{\epsilon r_{ij}} + \sum_{i>j} \left[\frac{A_{ij}}{r_{ij}^9} - \frac{B_{ij}}{r_{ij}^6} \right] \tag{11, 12, 13}
\end{aligned} \tag{4.2}$$

This forcefield employs quartic polynomials for bond stretching (Term 1) and angle bending (Term 2) and a three-term Fourier expansion for torsions (Term 3). The out-of-plane (also called inversion) coordinate (Term 4) is defined according to Wilson *et al.* (1980). All the crossterms up through third order that have been found to be important (Terms 5-11) are also included. This gives a forcefield equivalent to the best used in a formate anion test case (Maple *et al.*, 1990). Term 12 is the Coulombic interaction between the atomic charges and Term 13 represents the van der Waals interactions, using an inverse 9th-power term for the repulsive part rather than the more customary 12th-power term.

4.2 Background of MD-EXAFS

Extended X-ray absorption fine structure (EXAFS) spectroscopy is a method widely used for characterization of solvent-solute interaction. In EXAFS, an X-ray source is tuned to energies just slightly above an inner-shell electron absorption edge. As a result, a low-energy electron is ejected and is backscattered by atoms of the nearest solvent shells. This scattering process leads to interferences with the outgoing wave, giving rise to the characteristic oscillations of the EXAFS spectra. An analysis of the relation between EXAFS spectra and molecular structure has benefited from the availability of efficient algorithms for the evaluation of electron scattering analysis such as those implemented in the FEFF6 code by Rehr, Albers, and Zabinsky (1990, 1991, 1992, 1995). In standard EXAFS analysis, the fine structure factor is defined by

$$\chi(E) = \frac{\mu(E) - \mu_0(E)}{\Delta\mu_0(E_0)} \quad (4.3)$$

where $\mu(E)$ is the absorption coefficient as a function of the X-ray energy E , $\mu_0(E)$ is the background absorption coefficient, and $\Delta\mu_0(E_0)$ is the jump in the absorption background at the absorption edge, E_0 . Given a set of neighboring atoms located at positions r_i relative to the photoelectron source located at r_0 , with $R_i = |r_i - r_0|$, the EXAFS signal in k -space is described by:

$$\chi(k) = \sum_i N_i \frac{F_i(k)}{kR_i^2} e^{-2\sigma_i^2 k^2} e^{-2R_i/\lambda} \sin[2kR_i + \varphi_i(k)] \quad (4.4)$$

where the photoelectron wave-vector, k , is related to the X-ray energy by $E = E_0 + (\hbar^2 k^2)/2m_e$. N_i is the number of neighboring atoms in the i th coordination shell at a distance R_i away from the absorbing atom. The backscattering amplitude and mean-squared displacement of the neighboring atoms are given by $F_i(k)$ and σ_i , respectively. The phase shift of the photoelectron is given by $\varphi_i(k)$, while the exponential term containing the mean free path λ of the photoelectron accounts for their inelastic scattering. It is this exponential damping term which accounts for the selectivity of EXAFS to short-ranged order. The backscattering amplitude and the phase shift functions are extracted from EXAFS spectra taken from a standard which has a known structure and which contains the same absorbing and scattering elements as the unknown. A Fourier transform of the oscillations in k -space yields a real-space distribution, similar to a radial distribution function. Fitting Equation 4.4 to the measured EXAFS spectra can provide the structural parameters: the number and type of surrounding atoms, their average distance to the central absorbing atom, and their distribution about the absorbing center.

Due to the advance of modern EXAFS algorithms and the availability of more accurate ion and solvent potential models, the number of studies that combine MD with EXAFS has increased considerably (Ferlat *et al.*, 2001; McCarthy *et al.*, 1997; Hoffmann *et al.*, 1999; Wallen *et al.*, 1997; Fulton *et al.*, 2000; Spångberg *et al.*, 2000; Okamoto, 2004). MD-EXAFS, a method to generate EXAFS spectra from an MD simulation, has been recently developed. In the MD-EXAFS procedure, an ensemble of configurations is generated by an empirical potential and then electron scattering analysis is performed on each configuration to generate an individual fine structure spectrum and these spectra are finally averaged to obtain the fine structure

corresponding to the simulation and the empirical potential. The average EXAFS spectrum from the simulation was obtained from a configurationally average:

$$\bar{\chi}(E) = \frac{\bar{\mu}(E) - \mu_0(E)}{\Delta\mu_0(E_0)} \quad (4.5)$$

where bars denote the configurationally average. This is often fitted to the expression

$$\bar{\chi}(k) = \sum_i N_i S_0^2 \frac{\bar{F}_i(k)}{k\bar{R}_i^2} e^{-2\bar{R}_i/\lambda - 2k^2\sigma_i^2} \sin\left[2k\bar{R}_i + \bar{\varphi}_i(k) - \frac{4}{3}C_{3,i}k^3\right] \quad (4.6)$$

In this expression, $\bar{F}_i(k)$ is often estimated from a single symmetric characteristic configuration and is assumed to have insignificant fluctuations with configuration. The Debye-Waller factor, σ_i^2 , and the third cumulant, $C_{3,i}$, reflect the structural disorder of the system. The amplitude reduction factor, S_0^2 , accounts for many body effects in a single particle theory.

In order to obtain a real-space representation of the EXAFS spectra, a Fourier transform of the structure factor is calculated as implemented in the FEFFIT package. Equation 4.6 is thus transformed to:

$$\tilde{\chi}(R) = \frac{1}{\sqrt{2\pi}} \int_0^\infty k^2 \bar{\chi}(k) W(k) e^{i2kR} dk \quad (4.7)$$

where $W(k)$ is a Hanning window.

4.3 EXAFS Experimental Details

Potassium *K*-edge (3608.4 eV) EXAFS spectra were collected at X-ray Absorption Spectroscopy Beamline 8 (BL-8), Synchrotron Light Research Institute (SLRI), Thailand. For ~ 1 mol/dm³ KI in aqueous solution, 2-eV steps were used in the pre-edge region, while 0.2-eV steps were employed from 60 eV below the edge to 60 eV above the edge. For the EXAFS region (60 eV above the edge to 800 eV), 2-eV steps were employed. Energy calibration was performed with the KI salt. All measurements were performed under 250 mbar air gas. A total of 3 scans (each scan lasted approximately 20 min) were collected, and these scans were added after E_0 determination before further data analysis to improve the signal to noise ratio.

Iodide *K*-edge normalized absorption spectrum was provided by Prof. Dr. Iwao Watanabe, Ritsumeikan University, Kusatsu, Shiga, Japan. The EXAFS experiments of 0.1 mol/dm³ iodide anion dissolved in aqueous solution were done at Beamline **BL01B1**, SPring-8, Japan.

4.4 Computational Details

MD simulations were carried out on a system consisting of one ion (K^+ or I^-) and 64 to 500 water molecules in a cubic simulation box with cell length determined from the density of ~ 1.0 g/cm³. Periodic boundary conditions were applied in all three spatial directions. MD simulations were performed at 300 K, in the NVE ensemble using the Discover module in Materials Studio 4.2 simulations package provided by National Nanotechnology Center, Thailand. The COMPASS forcefield which is the first *ab initio* forcefield was used. The equations of motion were integrated using the velocity Verlet algorithm with a time step of 1 fs. The nonbonded interactions (*i.e.*

Lennard-Jones, and Coulombic) were truncated at molecular center-of-mass separations of 9.5 Å. After minimization by Molecular Minimization, the ion-solvent systems were equilibrated for 100 ps followed by a 1000 ps MD trajectory for data analysis. When the simulations were finished, radial distribution functions were calculated to evaluate the structural parameters (*i.e.* distance and coordination number) of the $\text{K}^+/\text{H}_2\text{O}$ and $\text{I}^-/\text{H}_2\text{O}$ systems. Furthermore, for each configuration taken from the trajectory, a cluster was obtained by extracting all species that fell within 6 Å (covering the first and the second coordination shells) radius of the probed (K^+ or I^-) ion. The cluster was then used as an input to the program FEFF6, which calculates the EXAFS spectrum $\mu(E)$ for the probed ion as a function of energy, E , using a multiple scattering approach. Some configurations taken from each simulation were used to generate EXAFS spectra and then the averaged spectrum was compared to the measured one.

4.5 Results and Discussion

4.5.1 Radial Distribution Functions (RDFs)

Figure 4.2 shows the atomistic molecular models of (a) $\text{K}^+/\text{H}_2\text{O}$ and (b) $\text{I}^-/\text{H}_2\text{O}$ systems. The calculated RDFs for $\text{K}^+/\text{H}_2\text{O}$ and $\text{I}^-/\text{H}_2\text{O}$ systems are included in Figure 4.3 and Figure 4.4, respectively. The simulated peak positions and coordination numbers are summarized in Table 4.1.

For $\text{K}^+/\text{H}_2\text{O}$ system, the coordination number obtained by integration of the first peak in the RDF out to its first minimum is 6.4, which is in excellent agreement with 6.8 and 7, the results from MD simulation with polarized forcefield reported by Glezakou *et al.* (2006) and from recent MD simulation as well as experimental

measurements (Marcus, 1988), respectively. Moreover, the K^+ -O distance and coordination number from our MD simulation of 2.65 Å and 6.4 respectively, are in good agreement with recent *ab initio* dynamics simulations where values of 2.80 Å and 6.0–6.8 are reported (Rempe, Asthagiri, and Pratt, 2004; Fulton, Heald, Badyal, and Simonson, 2003).

The observations for I^-/H_2O system are as follows. The I–O and I–H distances and the coordination numbers, N_O and N_H from MD simulation are 3.55 Å, 2.55 Å, 6.9, and 6.4, respectively. These values agree well with the literature data (Brodszkaya, Lyubartsev, and Laaksonen, 2002; Tóth, 1996; Heuft and Meijer, 2005). Structural data obtained from Monte Carlo (MC) and MD techniques (Brodszkaya *et al.*, 2002; Koneshan *et al.*, 1998; Lee, 1996; Hribar *et al.*, 2002; Ignaczak *et al.*, 1999; Ayala *et al.*, 2003; Tóth, 1996) include an I–O RDF first peak in the range of 3.55–3.78 Å and an I–H first peak in the range of 2.55–2.93 Å and the calculated coordination number varies from 7.3 to 9.7 based on coordinating oxygen and 6 to 6.6 based on coordinating hydrogen. Recently, density functional theory (DFT) based MD simulations (Heuft and Meijer, 2005) were also employed to study the solvation properties of iodide anion in water. The distances of I–O and I–H as well as the coordination numbers, N_O and N_H are 3.55 Å, 2.61 Å, 6.6, and 5.1, respectively. From Figure 4.4, the low intensity first peak followed by a high minimum, in combination with the broad and low intensity second peak are observed. This leads to the conclusion that the solvation shell of iodide is rather unstructured and diffuse.

We will use the simulated solvation structures to compute the MD-EXAFS spectra for dilute K^+ and I^- ions in aqueous solution (Section 4.5.2).

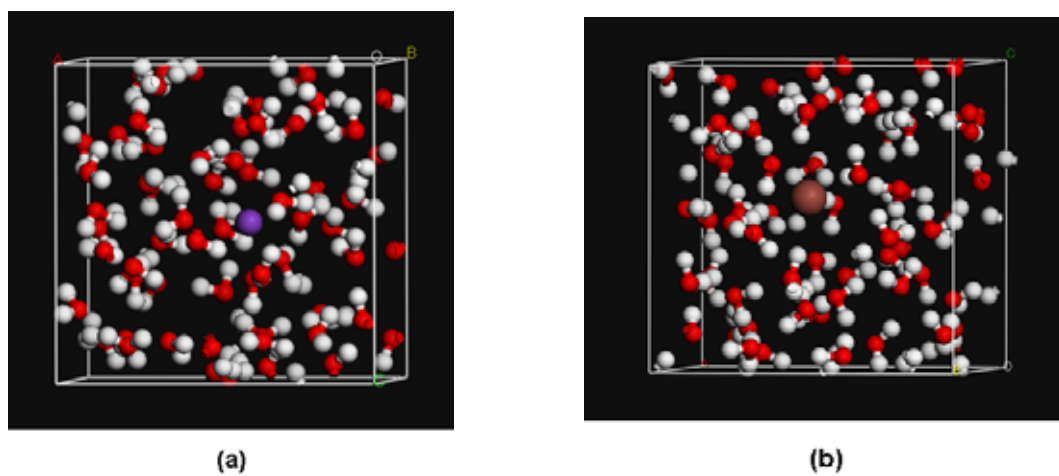


Figure 4.2 Atomistic models of (a) $\text{K}^+/\text{H}_2\text{O}$ and (b) $\text{I}^-/\text{H}_2\text{O}$ (colors: hydrogen atoms—white, oxygen atoms—red, potassium ion—purple, and iodide ion—brown).

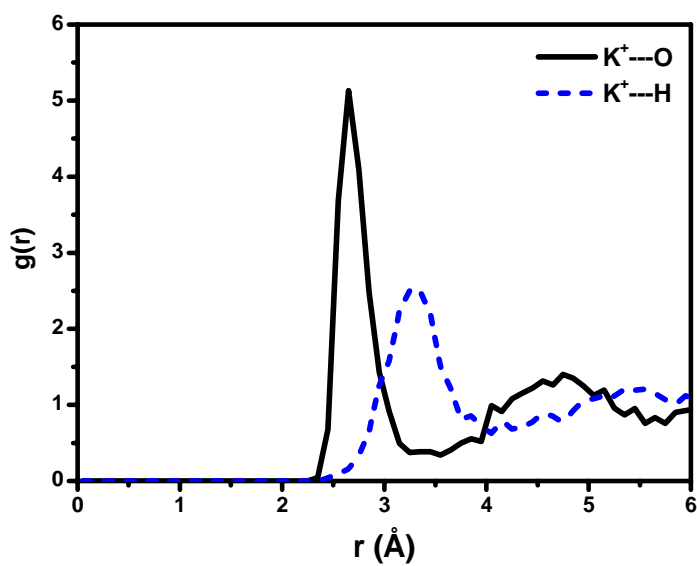


Figure 4.3 RDFs for $\text{K}^+ \cdots \text{O}$ (solid line) and $\text{K}^+ \cdots \text{H}$ (dashed line).

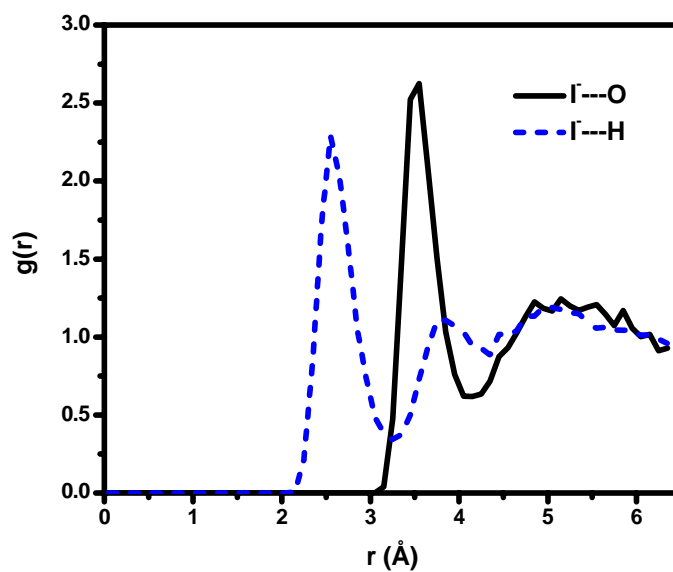


Figure 4.4 RDFs for I⁻-O (solid line) and I⁻-H (dashed line).

Table 4.1 Parameters characterizing the first peak of RDFs determined from MD at 300 K for K⁺/H₂O and I⁻/H₂O systems.

Ions	$R_{ion-O}(\text{Å})$		$R_{ion-H}(\text{Å})$		N_O		N_H	
	MD ^a	Ref.	MD ^a	Ref.	MD ^a	Ref.	MD ^a	Ref.
K ⁺	2.65	2.6-2.8 ^b	3.25	3.30 ^b	6.4	5-8 ^b	17.4	–
I ⁻	3.55	3.55 ^c	2.55	2.61 ^c	6.9	6.6 ^c	6.4	5.1 ^c

^aThis work.

^bMarcus, 1988.

^cHeuft and Meijer, 2005.

4.5.2 MD-EXAFS and Experiments

Selected 20 independent configurations of water molecules and one ion from MD simulations were taken into account for the MD-EXAFS analysis. For each configuration, a cluster of the closest water molecules to the photoelectron source (K^+ or I^-) were extracted from the configuration to form an input for electron multiple scattering analysis. This forms a cluster surrounding the probed ion with a radius of about 6 Å (this cutoff was selected beyond the distance of the first and the second solvation shells of K^+ and I^- ions). For each solvation system, two $\chi(k)$ EXAFS curves calculated from the clusters with and without hydrogens are plotted. The comparison between the calculation containing hydrogens and the calculation leaving hydrogens would give information about the effect of hydrogens on the EXAFS signals.

In Figure 4.5, the k^2 -weighted $\chi(k)$ experimental data from 1 mol/dm³ KI is compared to both MD-EXAFS spectra (with and without hydrogens). The MD-EXAFS spectrum calculated from containing hydrogens (*dotted red line*) is far from satisfactory (*i.e.* amplitude of $\chi(k)$ oscillation is too low). The effect of hydrogens on the calculated EXAFS spectra of cation hydration systems has been explained in literatures (Palmer, Pfund, and Fulton, 1996; Merklings, Ayala, Martínez, Pappalardo, and Marcos, 2003). The inclusion of hydrogen atoms proved necessary for obtaining a realistic backscattering potential but led to a sensible degradation of the spectrum when they were included as backscatterers. Hydrogens distort the calculation of the background $\mu_0(E)$ quite severely, apparently due to their effect on the muffin-tin radius of the potential of the absorbing atom, but do not have as large an effect on the $\chi(k)$. It turns out that the spectrum calculated without the hydrogens does a much better job of reproducing the number of nearest neighbors.

Next, the comparison between the EXAFS spectra from experiment (*solid line*) and from MD simulation which left all the hydrogens out of the configurations (*dash-dot line*) shows an overall good agreement for the frequency and the amplitude of the oscillations over the full k range from 2 to about 7 \AA^{-1} . The matching of the frequency of the oscillations means that the $\text{K}^+\text{-O}$ distances are nearly the same between the experiment and the simulation. The corresponding $\tilde{\chi}(R)$ plots derived from the experimental measurements are shown in Figure 4.6, together with the computed generated ensemble (MD-EXAFS). The $\tilde{\chi}(R)$ was generated by Fourier transform of the $k^2\chi(k)$ data, and they represent the partial pair distribution functions convoluted with the photoelectron scattering functions from Equation 4.4. Again, there is a remarkably good agreement in the radial structures of the experimental and simulated data. It is important to realize that the $\tilde{\chi}(R)$ are not exact representations of the $g_{\text{KO}}(r)$ (Ferlat, Soetens, Miguel, and Bopp, 2005). The K-O phase shift function, $\varphi_{\text{KO}}(k)$ in Equation 4.4 alters the phase of the scattered photoelectron leading to significant broadening and an R -shift of the K-O peak in Fourier transformed $k^2\chi(k)$ data.

Figure 4.7 displays the clusters (only four clusters are exemplified) extracted from MD configurations. We found that there are five to seven water molecules surrounding one potassium cation with $\text{K}^+\text{-O}$ distances less than the first minimum (3.55 \AA) of the $\text{K}^+\text{-O}$ RDFs peak. This agrees with the coordination number, $N_O = 6.4$, calculated from the MD result. The position of oxygen atoms in the solvation structures is quite symmetric and hydrogen atoms prefer to point away from the symmetric $\text{K}^+\text{-O}$ axes.

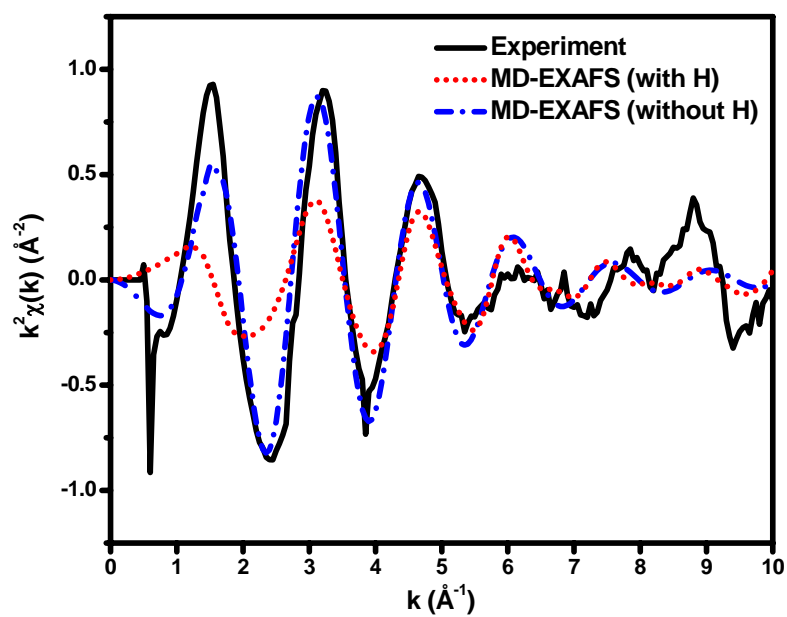


Figure 4.5 Comparison of potassium EXAFS k^2 -weighted $\chi(k)$ plots for K^+ in aqueous solution from experiment (*solid line*) and MD simulation (*dotted line*: hydrogens are included, *dash-dot line*: hydrogens are excluded).

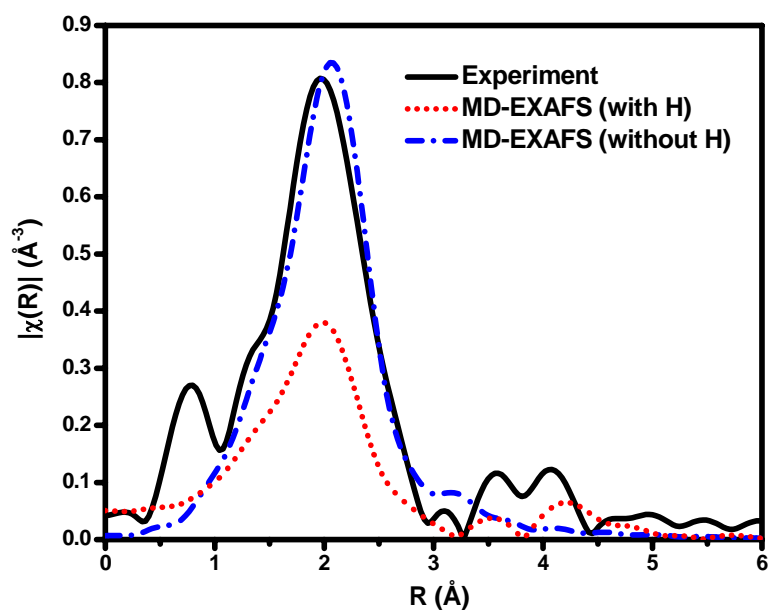


Figure 4.6 The $|\tilde{\chi}(R)|$ plots corresponding to the Fourier transformed $k^2\chi(k)$ as shown in Figure 4.5. The distances were not corrected for phase shifts. The unphysical peak at 0.9Å is an artifact of the multi-electron excitations.

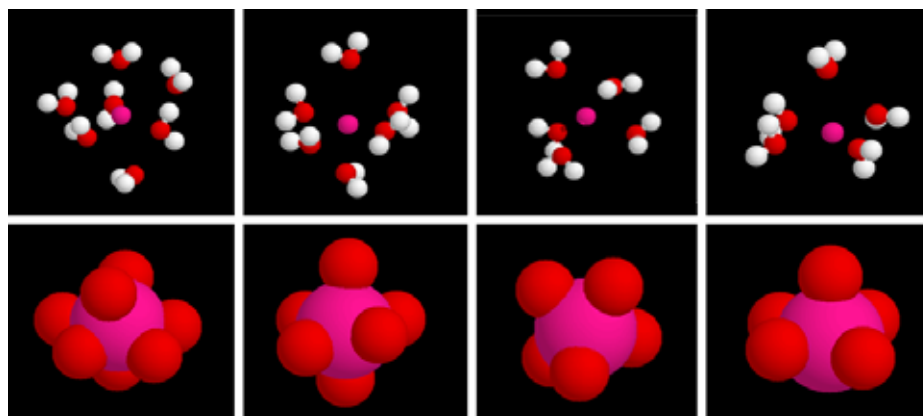


Figure 4.7 $K^+(H_2O)_n$ ($n = 5, 6, 7$) clusters extracted from MD configurations. The upper figures show hydrogen atoms while the lower figures do not display hydrogen atoms. (colors: potassium cations–pink, oxygen atoms–red, and hydrogen atoms–white).

In Figure 4.8, the k^3 -weighted $\chi(k)$ experimental data from 0.1 mol/dm³ iodide aqueous solution is compared to the MD-EXAFS spectra generated from the MD simulation. We found that the amplitude and frequency of oscillation calculated from leaving hydrogens out the configurations (*dash-dot line*) are similar to those from containing hydrogens in the configurations (*dotted line*) but there is a shift of peak positions as seen in Figure 4.8(a). The simulated spectrum with including hydrogens gave the better matching of peak positions to the experimental spectrum as seen in Figure 4.8(b). Thus, we suggest that hydrogens are important in EXAFS spectra of the iodide aqueous solution. Merklings *et al.* (2003) also reported the importance of hydrogens in XAS spectra of bromide aqueous solution. They found that leaving hydrogens out of the configurations gave the $\chi(k)$ MD-EXAFS spectrum far from satisfactory *i.e.* the amplitude of oscillation is lower than the MD-EXAFS with containing hydrogens. For the I/H₂O system, the comparison between the EXAFS spectra from experiment (*solid line*) and from MD simulation which all the hydrogens were included in the configurations (*dotted line*) shows an overall good agreement for the frequency and amplitude of the oscillations. This agreement of frequency means that I–O and I–H distances are nearly the same between the experiment and the simulation. Again, the $\tilde{\chi}(R)$ plot derived from the experimental measurement is consistent with that from the MD-EXAFS method as shown in Figure 4.9.

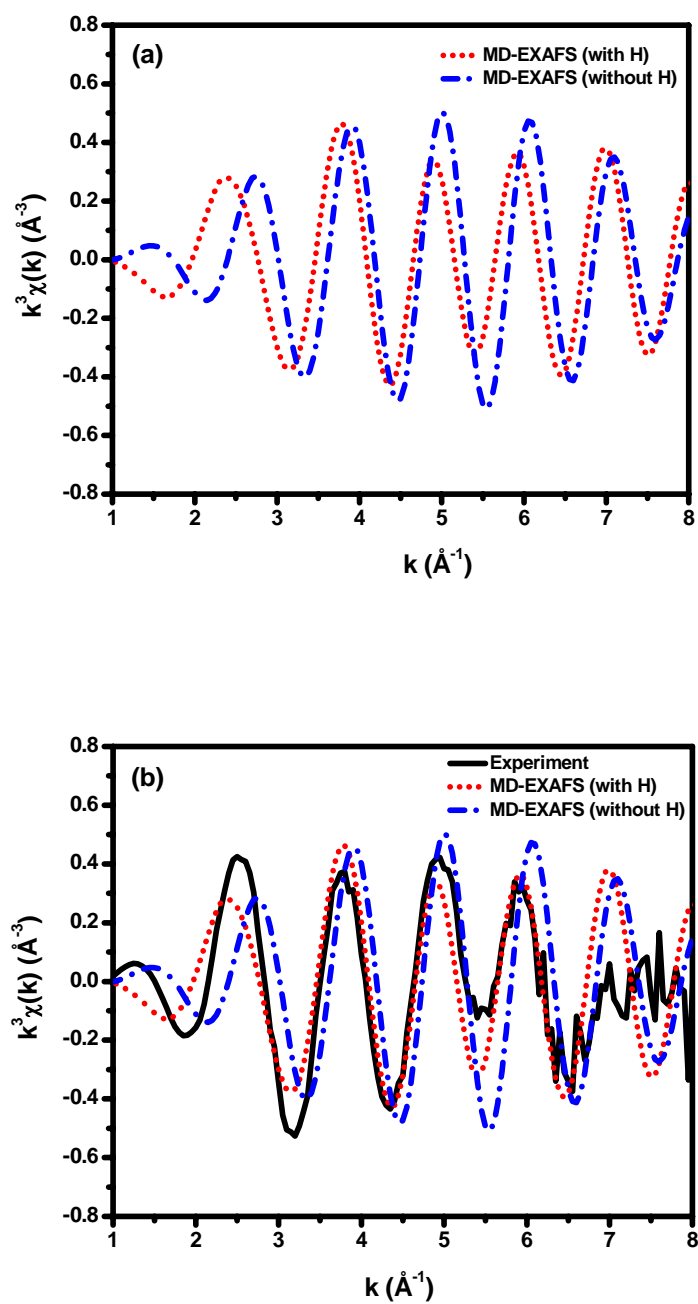


Figure 4.8 Comparison of iodide EXAFS k^3 -weighted $\chi(k)$ plots for iodide in aqueous solution from experiment (*solid line*) and MD-EXAFS (*dotted line*: hydrogens are included, *dash-dot line*: hydrogens are excluded).

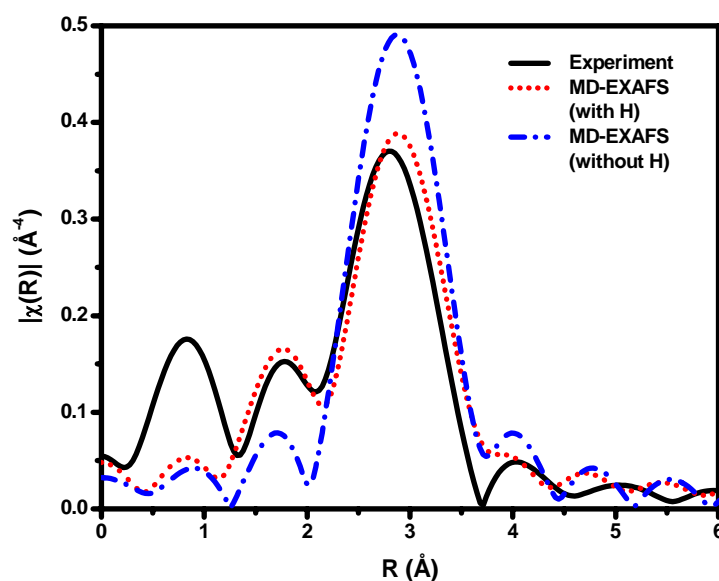


Figure 4.9 Comparisons of the R -space EXAFS spectra from experiments and MD simulations with including and excluding hydrogens.

Figure 4.10 displays the structures extracted from MD configurations for the first solvation shell of an iodide anion. Upper figures show six to eight water molecules surrounding one iodide anion while lower figures show only hydrogens and oxygens which fell within the first minima of the I-H ($\leq 3 \text{ \AA}$) and I-O ($\leq 4 \text{ \AA}$) RDFs peaks, respectively. Hydrogens in the structures are close to and point at the iodide anions.

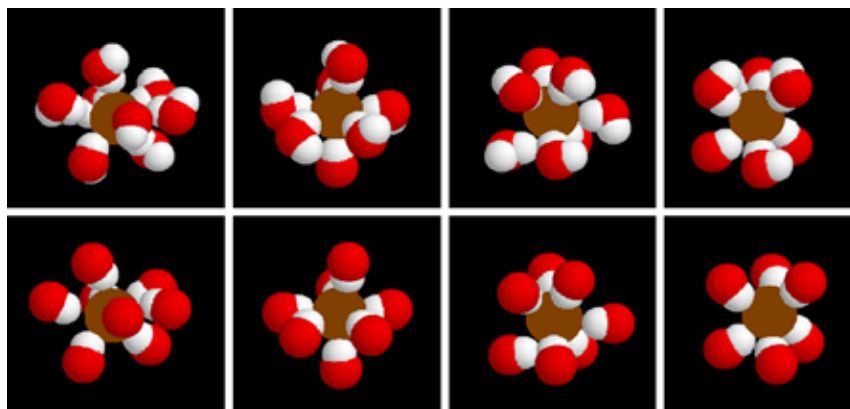


Figure 4.10 The structures extracted from MD configurations for the first hydration shell of Γ^- anion. Upper figures show six to eight water molecules surrounding one Γ^- anion while lower figures show only H and O that fell within the first minima of the Γ^- -H ($\leq 3 \text{ \AA}$) and Γ^- -O ($\leq 4 \text{ \AA}$) RDFs peaks, respectively (colors: Γ^- -brown, O-red, and H-white).

4.6 MD-EXAFS Method for K^+ /Tetraglyme System

4.6.1 EXAFS Experimental Details

Potassium *K*-edge (3608.4 eV) EXAFS spectra were collected at X-ray Absorption Spectroscopy beamline 8 (BL-8), Synchrotron Light Research Institute (SLRI), Thailand. The EXAFS measurements were done on a 4 mol/dm^3 KSCN in tetraglyme solution.

4.6.2 Computational Details

MD simulation was carried out on a system consisting of one potassium ion and 50 tetraglyme [$\text{CH}_3\text{O}(\text{CH}_2\text{CH}_2\text{O})_4\text{CH}_3$] chains in a cubic simulation box with linear dimensions roughly of 26 \AA . Periodic boundary condition was applied in all

three spatial directions. Simulation was initially performed in the NPT ensemble for 100 ps at 300 K. Further the system was equilibrated for 100 ps followed by a 1000 ps MD trajectory in the NVT ensemble at 300 K for data analysis. The MD-EXAFS spectra were averaged over the 20 configurations. For each configuration, a cluster of all atoms that fell within a 6 Å radius of the potassium ion was extracted to form an input for electron multiple scattering analysis.

4.6.3 Results of EXAFS Experiment and MD-EXAFS

Radial distribution functions (RDFs) between K^+ and all tetraglyme atoms (O, C, H) were calculated and plotted together in Figure 4.11(a). For clarification, the K^+ -O, K^+ -C, and K^+ -H RDFs are separately plotted as seen in Figure 4.11(b), 4.11(c), and 4.11(d), respectively. The simulated peak positions and coordination numbers calculated from the first peaks of all RDFs are summarized in Table 4.2. Each K^+ cation is coordinated by ~8.0 oxygens (K^+ -O distance ≤ 4.55 Å), ~35.8 carbons (K^+ -C ≤ 7.15 Å), and ~40.6 hydrogens (K^+ -H ≤ 5.15 Å).

The calculations show that an average of 6.4 water oxygens coordinate K^+ while an average of 8.0 tetraglyme oxygens coordinate each K^+ with the same K^+ -O distance of 2.65 Å. The smaller coordination number for K^+ /H₂O system may be due to (i) oxygens (or water molecules) in K^+ /H₂O system can diffuse easier than ether oxygens in tetraglyme chains, and (ii) chelating complex formed by coordination between more than one ether oxygens in the same molecule and the central K^+ cation is favorable.

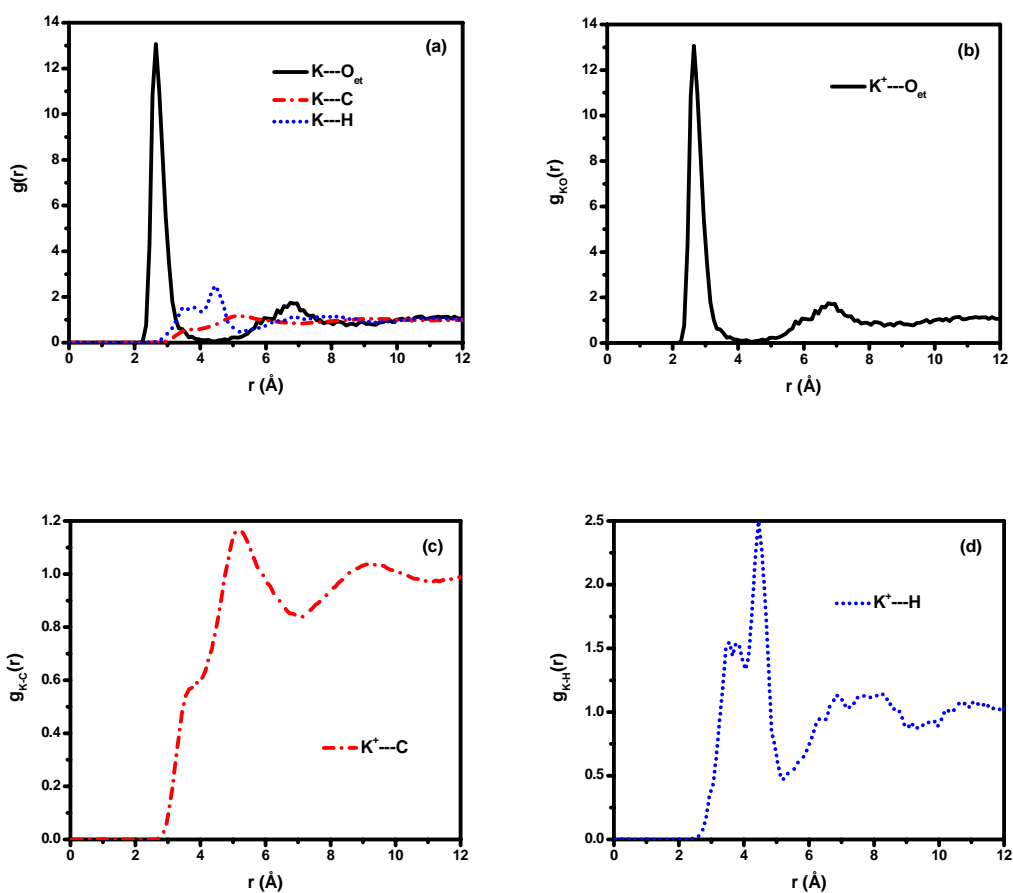


Figure 4.11 RDFs for (a) K^+ and all tetraglyme atoms, (b) K^+-O (*solid line*), (c) K^+-C (*dash-dot line*), and (d) K^+-H (*dotted line*).

Table 4.2 Parameters characterizing the first peak of RDFs determined from MD at 300 K for K^+ cation in tetraglyme.

Atom Pair	R (Å)	N (limit of integration)
K^+-O	2.65	8.0 ($0 \leq R \leq 4.45$)
K^+-C	5.25*	35.8 ($0 \leq R \leq 7.15$)
K^+-H	4.45*	40.6 ($0 \leq R \leq 5.15$)

* The highest point of the first shell

In Figure 4.12, the k^2 -weighted $\chi(k)$ experimental data (*solid line*) of ~ 4 mol/dm³ KSCN in tetraglyme solution were compared with the MD-EXAFS spectra of K⁺ in tetraglyme solution with including (*dotted red line*) and excluding (*dashed blue line*) hydrogens in the calculations. The $\tilde{\chi}(R)$ plots derived from the experimental measurements and MD-EXAFS are shown in Figure 4.13. The comparison shows an overall good agreement for the phase and the frequency of the $\chi(k)$ oscillations. However, the amplitude of $\chi(k)$ MD-EXAFS spectra is lower than that of the experimental EXAFS which may result from the neglect of (SCN)⁻ anions from the simulation. From the study of solvation structure of KI/tetraglyme systems using MD simulations as described in the next Chapter, the results revealed that I⁻ anions contribute to the first solvation shell of K⁺ cation as depicted in Figures 5.2 and 5.3. Thus, I⁻ anion should be an important scattering atom affecting on EXAFS signals of KI/tetraglyme system. Moreover, Dong *et al.* (2002) studied the solvation structure of NaCF₃SO₃/tetraglyme system with an ether oxygen:Na⁺ ratio of 10:1 at 300 K and 400 K. The Na⁺-O(tetraglyme) and Na⁺-O(triflate) RDFs revealed that triflate ions contribute more oxygens (4.9 at 300 K and 5.3 at 400 K) than tetraglyme (2.2 at 300 K and 2.0 at 400 K) to the first coordination shell of Na⁺ cation. Therefore, it can be confirmed that anions are important species contributing to the first solvation shell of a cation.

For both k - and R -space MD-EXAFS spectra of K⁺/tetraglyme system, the spectra with including and excluding hydrogens in the calculations are similar suggesting that hydrogens do not affect on EXAFS signals of this system.

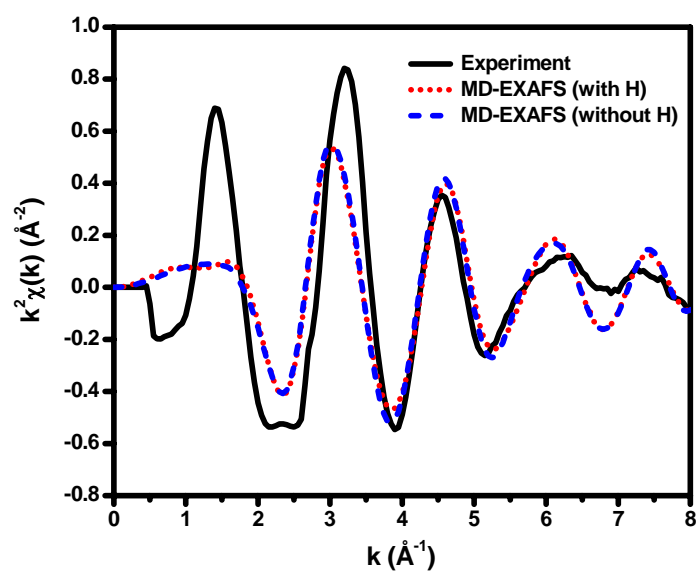


Figure 4.12 Potassium EXAFS k^2 -weighted $\chi(k)$ plots for K^+ /tetraglyme system.

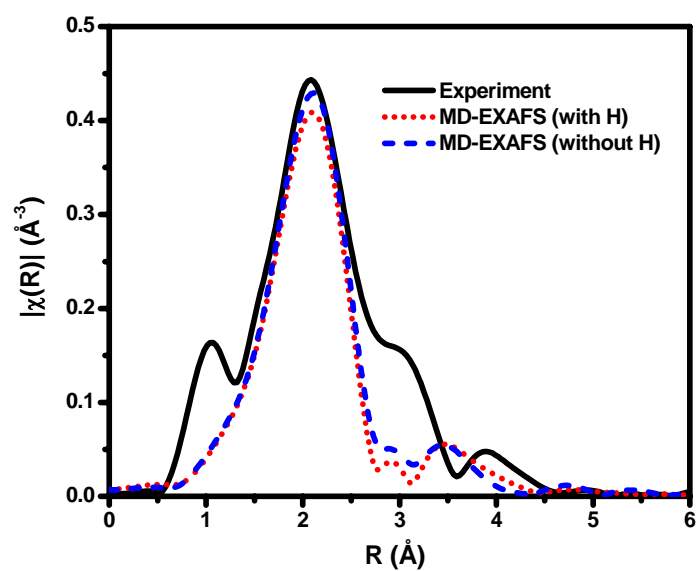


Figure 4.13 Comparison of the R -space EXAFS spectra from simulation and experiment for K^+ /tetraglyme system.

Figure 4.14 displays the clusters (radial cutoff from K^+ is 6 Å) extracted from MD configurations. We found that there are about eight oxygens from two tetraglyme chains surrounding one K^+ cation. This coordination number is consistent with that calculated from the RDFs as mentioned in Table 4.2.

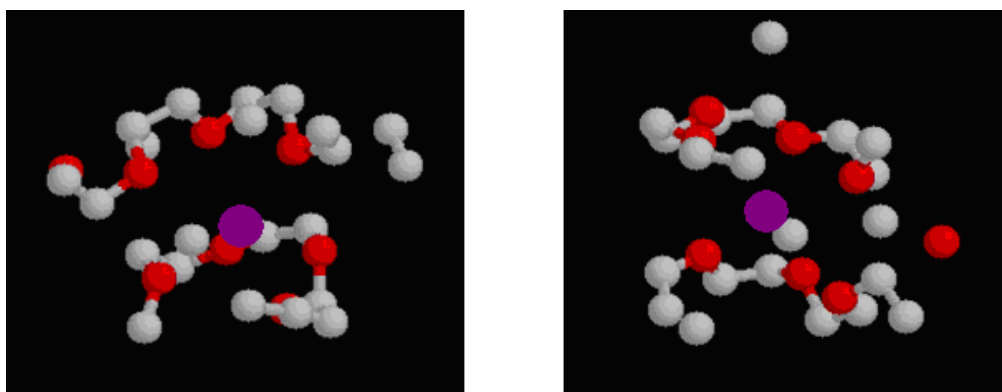


Figure 4.14 Clusters of PEO chains within a 6 Å radius of K^+ extracted from MD configurations (colors: carbon atoms–grey, oxygen–red, and potassium ion–purple).

4.7 Conclusions

In this Chapter, theoretical and experimental techniques are combined to describe and interpret the characteristics of the solvation structures of K^+ and I^- ions in water and K^+ ion in tetraglyme as model complexes for SPEs used in dye-sensitized solar cells. Molecular simulations with an empirical potential (COMPASS forcefield) were used to calculate the RDFs and local coordination at 300 K. Those structural properties obtained from the MD simulations are found to be in very good agreement with other works. The simulated solvation structures were used to compute the MD-

EXAFS spectra for K^+ and I^- ions in aqueous solution and K^+ ion in tetraglyme. MD-EXAFS spectra generated from MD simulations were then compared with the measured spectra. Comparison shows the consistence between the EXAFS spectra from MD simulations and those from the experiments. Thus, we suggest that MD simulation with empirical forcefield is a useful technique to study the local solvation structures of ionic aqueous solution and model compound representing PEO/salt electrolytes. However, it should be noted that generation MD-EXAFS for long chain polymer is outside the scope of this thesis. Therefore, in this work only smaller molecule complex systems have been illustrated.

CHAPTER V

MOLECULAR DYNAMICS SIMULATION OF TETRAGLYME:POTASSIUM IODIDE ELECTROLYTES

5.1 Introduction

Dye-sensitized solar cells (DSSCs) have been under investigation for the past decade due to their attractive features such as high energy conversion efficiency and low production costs (Oregan and Grätzel, 1991; Hara *et al.*, 2003). Regenerable redox couples (*e.g.* Γ/I_3^-) are usually dissolved in an organic solvent, which results in high energy conversion efficiency but some drawbacks such as leakage and evaporation of the solvent (Oregan and Grätzel, 1991; Hara *et al.*, 2003; Nogueira, Durrant, and De Paoli, 2001; Stergiopoulos, Arabatzis, Katsaros, and Falaras, 2002; Grätzel, 2000). Therefore, several attempts have been made to substitute liquid electrolytes with solid or quasi-solid state electrolytes such as solid polymer electrolytes (SPEs) (Nogueira *et al.*, 2001; Stergiopoulos *et al.*, 2002), polymer gel electrolytes (PGEs) (Kubo, Kitamura, Hanabusa, Wada, and Yanagida, 2002; Wang, Zakeeruddin, Exnar, and Grätzel, 2002; Stathatos, Lianos, Lavrencic-Stangar, and Orel, 2002), and organic hole-transport materials (HTMs) (Bach *et al.*, 1998; Gebeyehu *et al.*, 2002).

SPEs, usually comprised of alkali salts dissolved in a polymer matrix, have received considerable attention in recent decades because of their potential applications in electrochemical devices such as solid-state batteries (Mao, Perea, Howells, Price, and Saboungi, 2000; Gadjourova, Andreev, Tunstall, and Bruce, 2001) and separation membranes (Kim, Min, Lee, Won, and Kang, 2002). Poly(ethylene oxide) (PEO) has been most intensively studied as a polymer solvent for SPEs because it is both chemically stable and polar, which means that it can readily dissolve salts. However, its ionic conductivity is not satisfactory for solar cell applications primarily because of its high crystallinity. Thus, developing SPEs with high conductivity along with acceptable mechanical properties at room temperature is highly desirable. Molecular level understanding of ion transport in polymer:salt complexes is required to engineer systems with higher ionic conductivity at lower temperatures for improved device performance.

Although ionic motion through molecular liquids at low salt concentrations occurs through simple diffusion, ion-polymer interactions, polymer segmental motions, and ionic association complicate ion transport mechanisms in PEO-based SPEs. Understanding each of these aspects and their interrelations in amorphous PEO is necessary to engineer PEO-based SPEs with higher ionic conductivity. Numerous experimental and computational studies on these aspects have been performed (Catlow and Mills, 1995; Borodin and Smith, 1998, 2000; Ennari, Neelov, and Sundholm, 2000).

Experimental studies of PEO:salt complexes are as follows. X-ray diffraction (XRD) has been used to determine the structure of crystalline PEO and PEO:salt complexes. A variety of salts such as NaClO_4 , NaSCN , HgCl_2 , LiCF_3SO_3 , NH_4SCN ,

and KSCN have been studied. These studies show that the cations are coordinated to both the anions and the oxygens of PEO and the overall coordination number is dependent on the cation and the anion. It is also concluded from these studies that the conformation of PEO chains may be altered upon complexation with metal salts. Vibrational spectroscopy has been employed to study such conformational changes in crystalline and amorphous systems. PEO:NaX (X = Br, I, SCN, BF₄, and CF₃SO₃), PEO:MSCN (M = K, Rb, and Cs), and oligomer:salt complexes such as glyme:MCF₃SO₃ [M = Li, Na, and K; glyme is defined as CH₃O(CH₂CH₂O)_nCH₃. For example, the $n = 1$ oligomer is described as monoglyme, $n = 2$ as diglyme, $n = 3$ as triglyme, and $n = 4$ as tetraglyme or tetraethylene glycol dimethyl ether] have been examined by vibrational spectroscopy. Vibrational spectroscopy (Chintapalli and Frech, 1995; Huang, Frech, Johansson, and Lindgren, 1995; Bishop, MacFarlane, McNaughton, and Forsyth, 1996; Muhuri, Das, and Hazra, 1997; Chintapalli, Quinton, Frech, and Vincent, 1997) and X-ray absorption fine structure (Chintapalli, Frech, and Grady, 1997) have been used to investigate ionic association in PEO:salt complexes and oligomer:salt systems. Conductance measurements for a variety of PEO:salt and oligomer:salt complexes also show that ionic conductivity increases with increasing salt concentration up to a certain level (dependent upon the species of salt) and then decreases at high salt concentrations (Williamson, Southall, Hubbard, Davies, and Ward, 1999), where ionic mobility is presumably reduced by the lower mobilities of larger aggregate species.

Furthermore, computational techniques such as Molecular Dynamics (MD) and Monte Carlo (MC) have been performed to study PEO:salt complexes (Neyertz, Brown, and Thomas, 1995; Neyertz and Brown, 1995; Smith *et al.*, 1996). Several

MD simulations of PEO: MX models (MX = NaI, LiI, LiBr, and ZnBr₂) have been performed to examine an ionic association and conductivity (Muller-Plathe and van Gunsteren, 1995; Payne *et al.*, 1995; Neyertz and Brown, 1996; Londono *et al.*, 1997). Diffusion coefficients were calculated for PEO:NaI (Neyertz and Brown, 1995, 1996), PEO:LiI (Muller-Plathe and van Gunsteren, 1995), dimethyl ether:NaI, and monoglyme:NaI (Payne *et al.*, 1995) complexes.

MD simulation study of tetraglyme:KI is currently lacking, therefore it is appropriated to investigate this material here. Advantages of studying the tetraglyme:KI electrolytes include (1) tetraglyme and tetraglyme:salt complexes are more easily equilibrated, experimentally and computationally, than longer chain oligomers and PEO and (2) the local scale properties *i.e.* chain conformation and solvation structure are primary of interest in this work. MD simulation with COMPASS forcefield was employed to study the tetraglyme:KI complex as the first step toward a better understanding of more complicated systems *i.e.* PEO:KI and PEO:KI:I₂, which is the real component used in SPEs for DSSCs.

5.2 Computational Details

MD simulations of pure tetraglyme [CH₃O(CH₂CH₂O)₄CH₃, a 4-mers model compound for PEO] and tetraglyme:KI were performed using Materials Studio modeling 4.2 software provided by National Nanotechnology Center, Thailand. MD was performed using Discover module with COMPASS forcefield (Sun, 1998), which is one of the first *ab initio* forcefield approaches that has been parameterized and validated using the condensed-phase properties.

The simulated systems containing 50 tetraglyme chains (pure tetraglyme) and 50 tetraglyme chains plus 25 K^+ and 25 I^- ions for an ether oxygen: K^+ ratio of 10:1 (EO: K^+ = 10:1) were generated by Amorphous Cell module. The PEO:KI complex with the mole ratio of EO: K^+ = 10:1 was chosen because experimental results gave the highest ionic conductivities (Kalaigian, Kang, and Kang, 2006). Simulations were initially performed in the NPT ensemble for 1 ns at 300 K, and a new density of 1.04 g/cm³ was obtained. Further equilibrations of approximately 1 ns were performed in the NVT ensemble. Finally, for data analysis, atomic trajectories were collected for another 1 ns. The properties of interest to be investigated by MD techniques were: structure (radial distribution function between K^+ cations and all other species *i.e.* O, C, H, and I^-), conformation (dihedral distribution along C–C and C–O bonds), dimension (radius of gyration), and dynamics (mean square displacement of K^+ and I^- ions).

5.3 Results and Discussion

5.3.1 Radial Distribution Functions

To compare the coordination of K^+ by all other species in the system, the radial distribution functions (RDFs) between K^+ and ether oxygens, K^+ and carbons, K^+ and hydrogens as well as K^+ and I^- are plotted as seen in Figure 5.1 (a1). The RDFs between K^+ and ether oxygens as well as K^+ and I^- were calculated and plotted separately as seen in Figures 5.1 (b1) and 5.1 (c1) to examine how K^+ cations are coordinated by tetraglyme oxygens and iodide anions. All positions of peaks in the RDFs and the coordination numbers are listed in Table 5.1. Integrating the K^+ –O and K^+ – I^- RDFs over the first coordination shells gives an average 2.4 oxygens and 3.1

iodide anions coordinated to each K^+ . This result indicates that there is a competition in complexation of K^+ between ether oxygens and iodide anions, and that the degree of coordination of K^+ by iodide anions is not much stronger than that by ether oxygens. This observation is in contrast to the crystalline $P(EO)_3:LiCF_3SO_3$ compound, where a greater number of ether oxygens than triflate oxygens coordinated to Li^+ but is similar to the amorphous tetraglyme: $LiCF_3SO_3$ complex with an ether oxygen: Li^+ mole ratio of 10:1, where an average of 4.6 triflate oxygens and 1.6 ether oxygens coordinate each Li^+ (Hyun, Dong, Rhodes, Frech, and Wheeler, 2001). In addition to the EO:K = 10:1 system, the more diluted system with EO:K = 40:1 was also studied. All RDFs peak positions for the diluted system as seen in Figures 5.1 (a2), (b2), and (c2) remain the same as the more concentrated system while the coordination numbers (CN) are different as listed in Table 5.1. The RDFs and the coordination numbers of both systems are compared as shown in Figures 5.2 (a) and 5.2 (b) for K^+-O and K^+-I pairs, respectively. The similarity in the peak positions of RDFs indicates a fundamental similarity in K^+ complexation for both systems. Integrating the first peaks gives an average 4.4 ether oxygens and 1.8 iodide anions coordinated to each K^+ . This shows that ether oxygen is more competitive than the iodide anion in complexing with K^+ cation for the diluted system with a fewer number of iodide anions.

Figure 5.3 displays how K^+ cations are coordinated by ether oxygens and iodide anions for the first coordination shell (≤ 4.15 Å for ether oxygens and ≤ 4.85 Å for iodide anions) of the EO:K = 10:1 system. The total coordination number including both ether oxygens and iodide anions varies from three to eight. The case of two ether oxygens and three iodide anions (an overall coordination number of five)

coordinating to K^+ as seen in Figures 5.3 (a) and 5.3 (b), however, is the most frequently observed. The coordination numbers of six and seven as seen in Figures 5.3 (c) to 5.3 (f) are also frequently found. Tetraglyme chain can apply from one to all five ether oxygens to coordinate with K^+ . The tetraglyme chain with all of five ether oxygens coordinating with K^+ is shown in Figure 5.3 (f), leading to a more compacted chain with *gauche* conformations along all C–C bonds (discussed in details in Section 5.3.2).

Figure 5.4 shows the first coordination shells ($K^+ - O \leq 4.15 \text{ \AA}$ and $K^+ - I \leq 4.95 \text{ \AA}$) of K^+ cations for the diluted system. Most of K^+ cation is wrapped by all five ether oxygens of a tetraglyme chain and one or two iodide anions. This leads to tetraglyme chains interacting with K^+ cations become more compacted whereas other chains not directly involved in $K^+ - O$ complexation are similar to those in the pure tetraglyme system.

This result suggests that oxygens in tetraglyme chains can compete with iodide anions in complexing with K^+ cation. The complexation between ether oxygens and K^+ cations causes a change in tetraglyme chain conformation which observed in published experimental results and also from the dihedral distribution function and radius of gyration calculated from MD results.

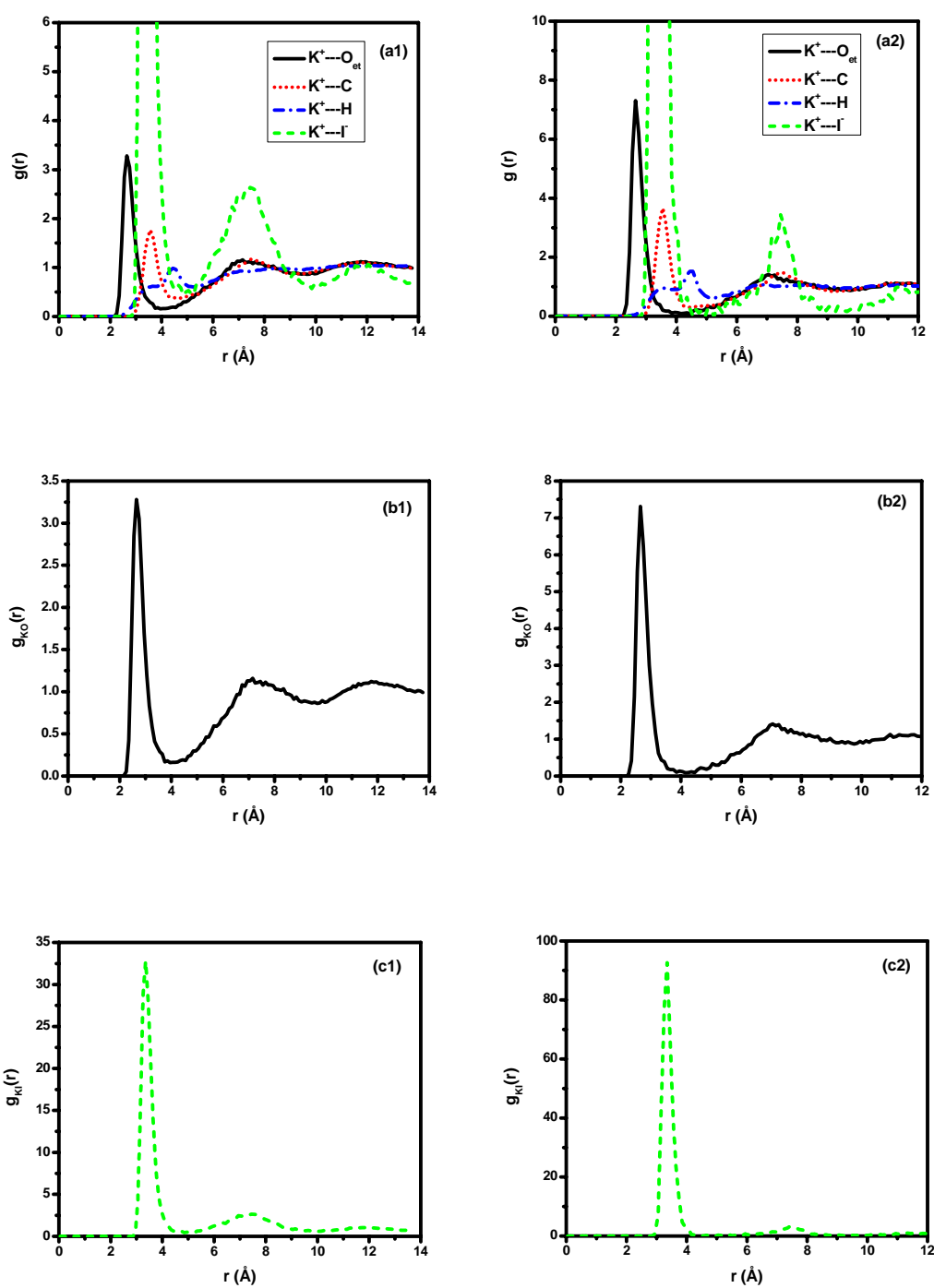


Figure 5.1 RDFs between (a1, a2) K^+ and all species, (b1, b2) K^+ and ether oxygens, and (c1, c2) K^+ and I^- in the tetraglyme:KI systems with EO:K = 10:1 (labeled by '1') and EO:K = 40:1 (labeled by '2') at 300 K.

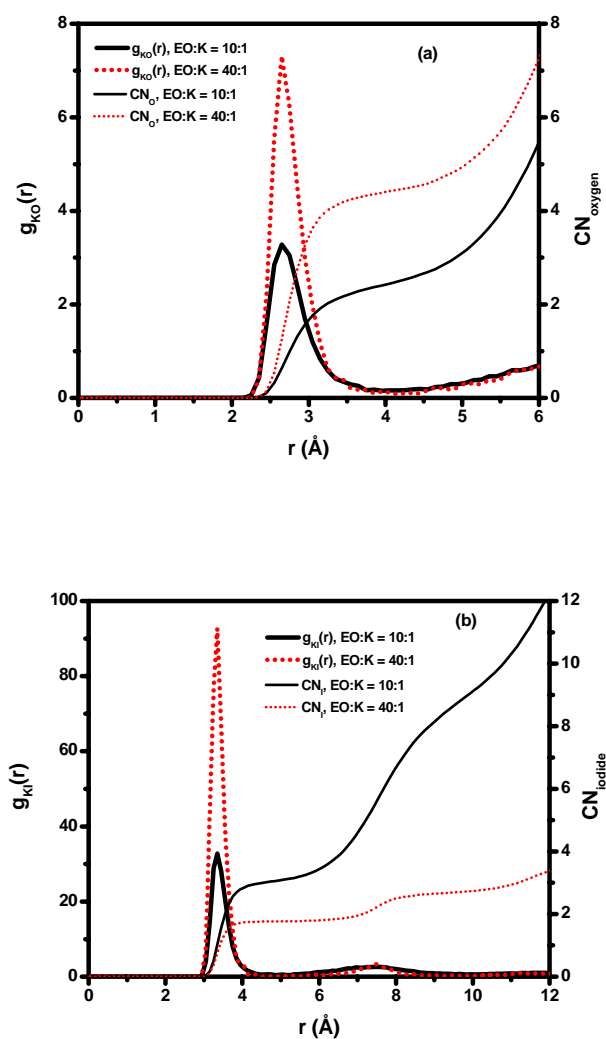


Figure 5.2 Comparison of the RDFs and CN of both tetraglyme:KI systems shown in (a) for K⁺-O pairs and (b) for K⁺-I pairs.

Table 5.1 Parameters characterizing the first peak of RDFs determined from MD at 300 K for tetraglyme:KI systems.

EO:K	Position of the first peak, R (Å)				Coordination number, CN			
	K^+-O_{et}	K^+-C	K^+-H	K^+-I^-	O_{et}	C	H	I
10:1	2.65	3.55	4.45	3.35	2.4	6.2	18.9	3.1
40:1	2.65	3.55	4.45	3.35	4.4	10.4	27.7	1.8

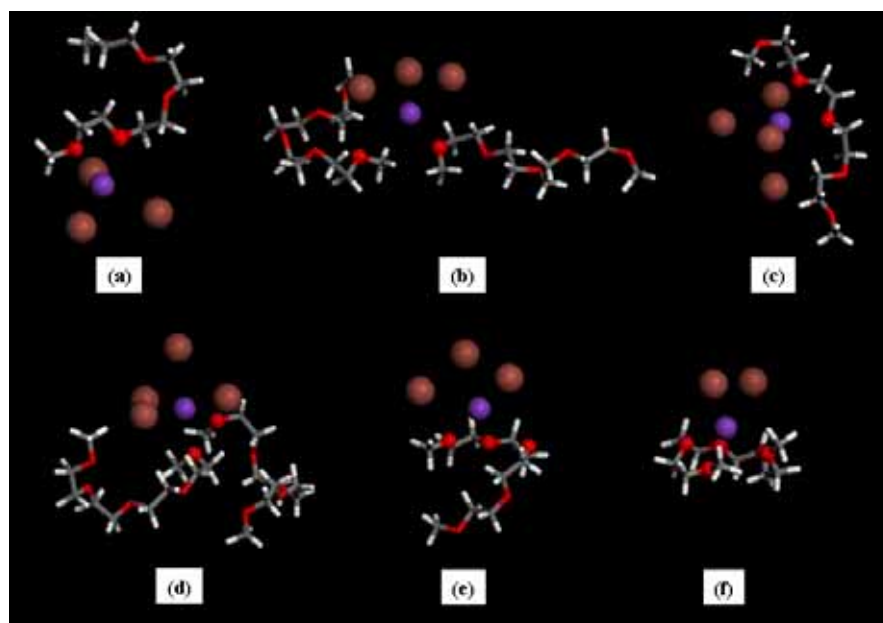


Figure 5.3 The coordination around K^+ (purple balls) of the EO:K = 10:1 system. Iodide and ether oxygens in the first coordination shell are represented by brown and red balls, respectively. Other atoms of tetraglyme not fell within the first shell are shown by sticks. Some structures extracted from MD configurations are exemplified: (a) and (b) show the coordination number (CN) frequently found of five (from two ether oxygens and three iodide anions); (c) to (e) display CN = 6; and (f) shows CN = 7.

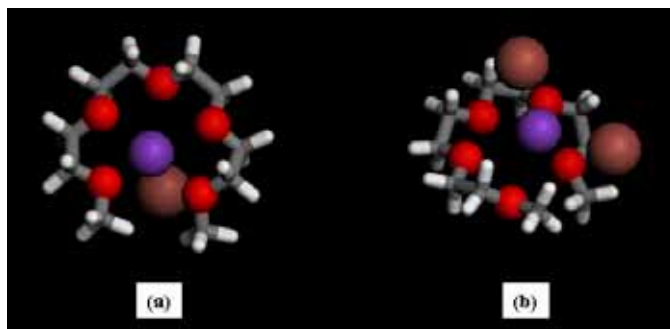


Figure 5.4 The coordination around K^+ of the EO:K = 40:1 system. Mostly, a K^+ cation is wrapped by all five ether oxygens of a tetraglyme chain and (a) one or (b) two iodide anions.

5.3.2 Chain Conformation and Dimension

It has been observed from vibrational spectroscopy and X-ray diffraction studies that the conformation of pure PEO is altered upon complexation of metal salts, as discussed in the Introduction Section. Therefore, K^+ complexation with ether oxygens of tetraglyme chains is expected to alter the conformation of tetraglyme chains. Besides, the dimensions of polymer chains should consequently be changed. The conformation of polymer chains can be characterized by the mean-square radius of gyration $\langle S^2 \rangle$, and the mean-square backbone end-to-end distance $\langle R^2 \rangle$, a measure of the size of the spatial distribution of polymer chains.

To examine the conformations of tetraglyme chains, the time-averaged population density distributions of backbone dihedral angles (φ) around C–O bonds (a C–C–O–C atom sequence) and C–C bonds (an O–C–C–O atom sequence) were calculated from MD simulation results. Comparison of dihedral angles for uncomplexed tetraglyme and tetraglyme:KI is shown in Figure 5.5 (a). The

convention to define the conformation with heavy atoms is eclipsed as $\varphi = 0^\circ$ and called *gauche*⁺ conformations (g^+) if the torsional angle has a value $0^\circ < \varphi < 120^\circ$, *gauche*⁻ conformations (g^-) if $240^\circ < \varphi < 360^\circ$, and *trans* conformations (t) if $120^\circ < \varphi < 240^\circ$ as illustrated in Figure 5.6. For pure tetraglyme, the *trans* conformation of dihedral angles along C–O bonds (*solid diamond*) is predominant while the *gauche* conformation (g^+ and g^-) of dihedral angles along C–C bonds (*solid square*) is favorable. For dihedral angles of tetraglyme:KI along the C–C bonds (*open square*), the g^+ conformation is centered about 64° , while the g^- conformation is centered about 296° , instead of 70° and 290° found in pure tetraglyme as seen in Figure 5.5 (b). This means that the two adjacent oxygen atoms of tetraglyme chain directly interacting with K^+ cation in the tetraglyme:KI system are closer up than those in pure tetraglyme system as illustrated in Figure 5.7. The population of both g^+ and g^- conformations increases ($\sim 2.4\%$) relative to those of pure tetraglyme while the t state vanishes ($\sim 10.7\%$). The distribution along the C–O bonds (*open diamond*) shows a less population of t conformation ($\sim 7.5\%$) and higher of the g^+ and g^- conformations ($\sim 20.1\%$) as compared to pure tetraglyme. This result should be from the interaction of K^+ cations with the polymer oxygens. An increase in *gauche* population causes the structures become more compact as seen in Figure 5.8 where the radius of gyration decreases upon K^+ –O complexation.

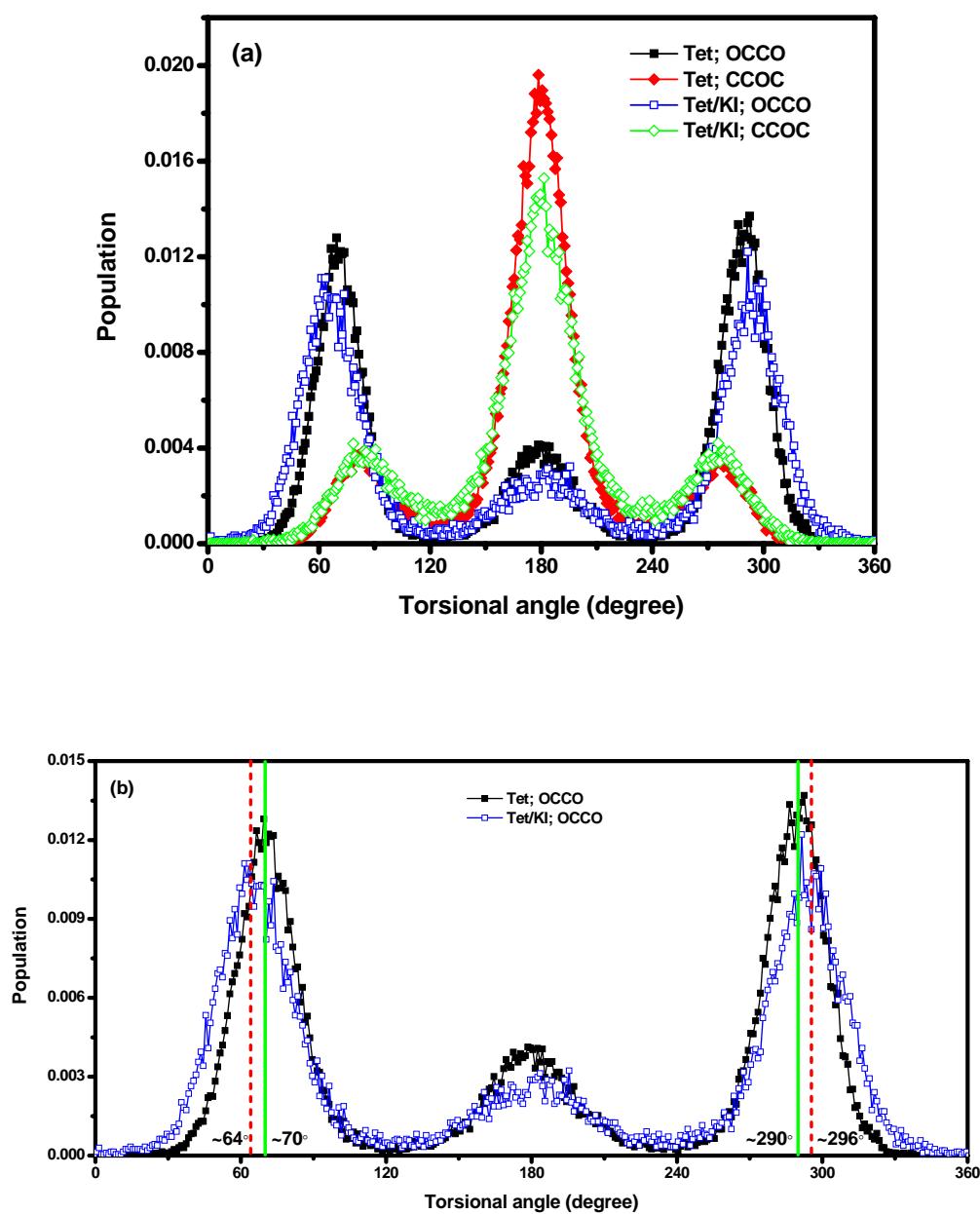


Figure 5.5 Time-average population density distributions of tetraglyme backbone torsions along C–C and C–O bonds in pure tetraglyme and tetraglyme:KI at 300 K ('Tet' = 'Tetraglyme'): (a) total dihedral distribution functions of interest, and (b) shift in dihedral angles along C–C bonds of tetraglyme:KI system from those of pure tetraglyme.

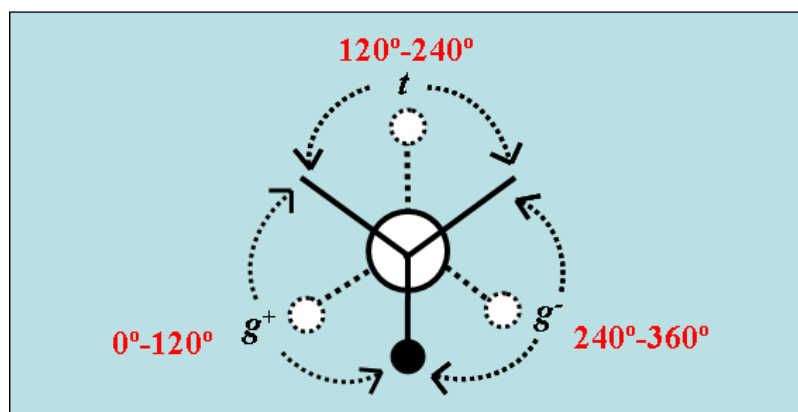


Figure 5.6 The torsional angles (φ) along C–C bonds (one carbon is at the intersection of the solid lines and another carbon is at the intersection of the dotted lines). The convention is to define the conformation with heavy atoms (smaller spheres; solid sphere is forward heavy atom and dotted sphere is backward heavy atom) eclipsed as $\varphi = 0^\circ$ and label g^+ if $0^\circ < \varphi < 120^\circ$, g^- if $240^\circ < \varphi < 360^\circ$, and t if $120^\circ < \varphi < 240^\circ$.

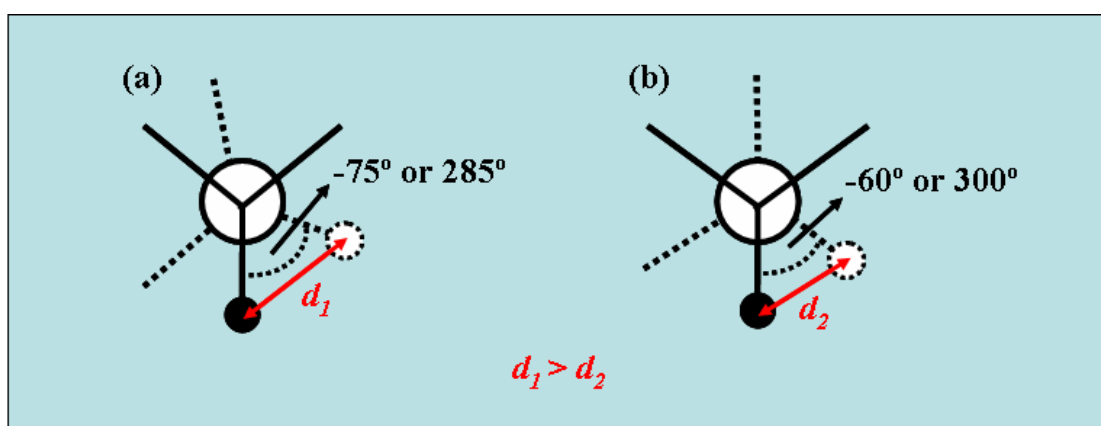


Figure 5.7 The scheme of the torsional angles along C–C bonds for (a) the more stretched chains with the longer distance (d_1) between the adjacent oxygens and (b) the more compacted chains with the shorter distance (d_2) between the adjacent oxygens.

Figure 5.8 shows the distributions of the root-mean-square radius of gyration, $\langle S^2 \rangle^{1/2}$ for pure tetraglyme (*solid line*) and tetraglyme:KI system with EO:K = 10:1 (*dotted line*) at 300 K. The $\langle S^2 \rangle^{1/2}$ distribution gives two dominant peaks: the small first peak occurs at 3.25 Å and the strong second peak occurs at 3.95 Å for pure tetraglyme. For the tetraglyme:KI system, the $\langle S^2 \rangle^{1/2}$ distribution also gives two peaks: the small first peak occurs at 3.15 Å and the strong second peak occurs at 3.85 Å, slightly shifting to the lower values as compared to the pure tetraglyme. The $\langle S^2 \rangle^{1/2}$ value directly relates to the size and the conformation of tetraglyme chains that is the smaller $\langle S^2 \rangle^{1/2}$ value, the more compacted chain. Therefore, for both systems, the first smaller peak in the $\langle S^2 \rangle^{1/2}$ distribution is caused by the more compacted chain as exemplified in Figure 5.9 (b) and the second larger peak is due to the more stretched chain as shown in Figure 5.9 (a). In Figures 5.9 (a) and 5.9 (b), the torsional angles along C–C bonds as well as the radius of gyration for each chain are displayed. From Figures 5.9 (a) and 5.9 (b), it can be noticed that the characteristics of the more stretched tetraglyme chains usually found in pure tetraglyme system and also in the region away from K^+ cations in the tetraglyme:KI system are as follows: (i) there is one (or more) *trans* state (marked by arrow) along C–C bonds, and/or (ii) there is more number of *gauche* (g^+ and g^-) states along C–C bonds than those are present in the compacted chains which means that the adjacent oxygens of tetraglyme chains locate at the positions with longer O–O distances. In Figure 5.8, the higher second peak means that the more stretched chain is more probable than the more compacted chain. Upon adding KI in tetraglyme, the height of the first peak obviously increases whereas that of the second peak decreases. This clearly suggests that the K^+ –O complexation results in the change in the conformation and the dimension of

tetraglyme chains. This change is easy to understand because the strong Coulombic attraction between K^+ cation and ether oxygen tends to pull segments of the chains together, particularly as adjacent oxygens coordinate a K^+ cation. Thus, the overall size of the chains in tetraglyme:KI system becomes smaller.

For the diluted system with EO:K = 40:1, the dihedral distribution functions and the $\langle S^2 \rangle^{1/2}$ distributions (*dashed line* in Figure 5.8) are slightly different from those for pure tetraglyme system (*solid line*). This may result from fewer number of ions, leading to less number of chains involved in the K^+ -O complexation while most of chains remains unchanged similar to the pure tetraglyme system.

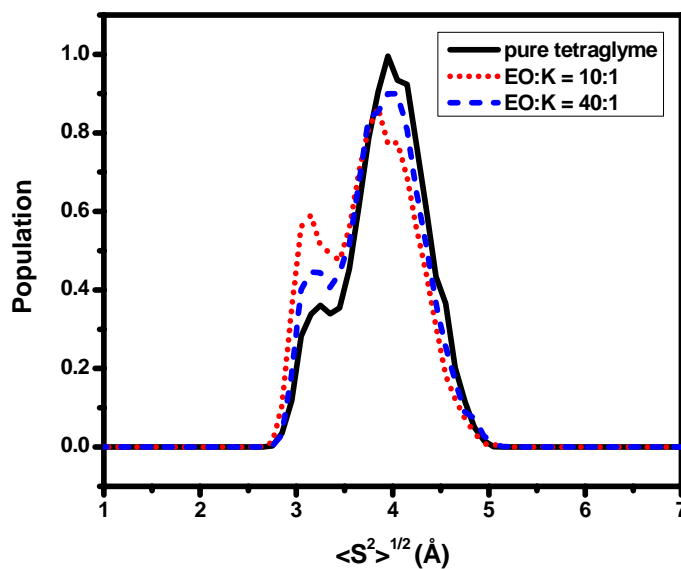


Figure 5.8 The $\langle S^2 \rangle^{1/2}$ distribution of tetraglyme:KI with EO:K = 10:1 (*dotted line*), and EO:K = 40:1 (*dashed line*) compared with that of pure tetraglyme (*solid line*) at 300 K.

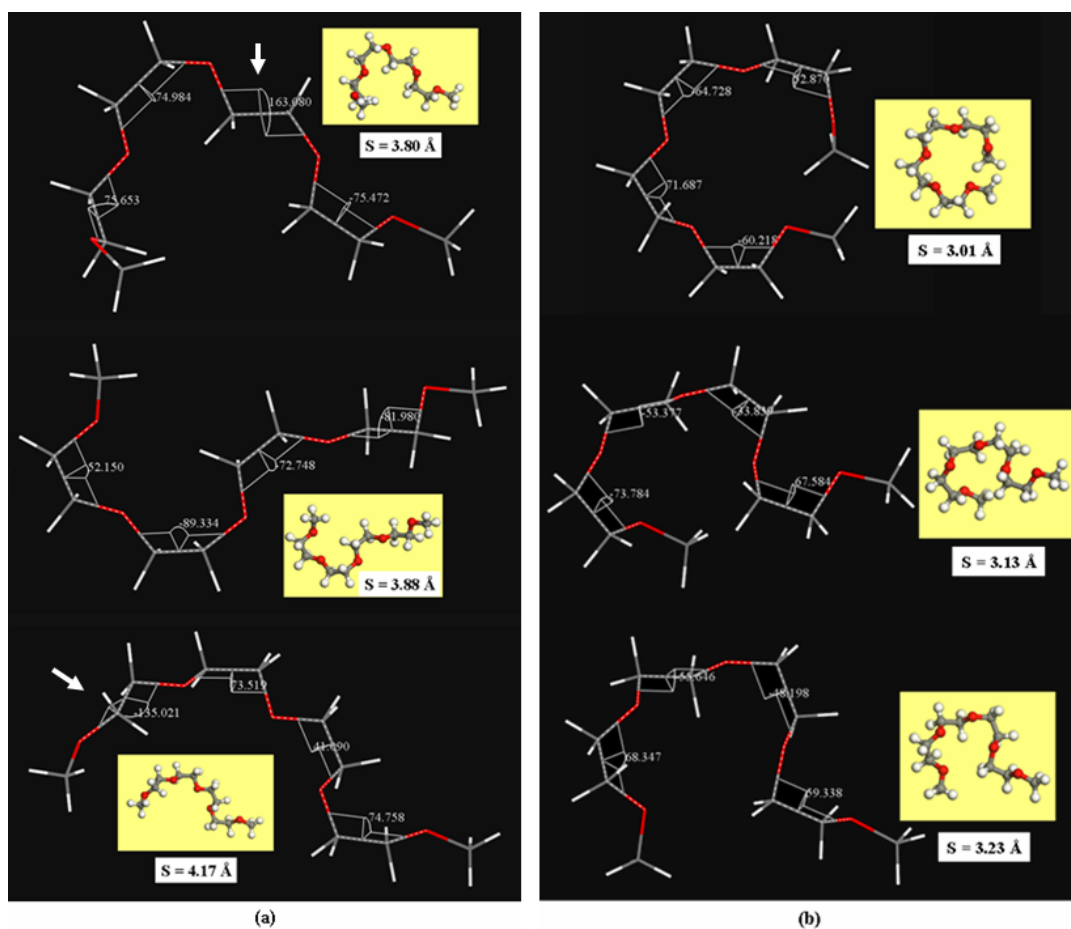


Figure 5.9 Tetraglyme chains from MD simulations of pure tetraglyme and tetraglyme:KI at 300 K. The torsional angles along C–C bonds and the radius of gyration, S for each chain are presented. Here, the positive values (0° to 120°) mean g^+ state while the negative values (0° to -120° , corresponding to the values of 360° to 240° in Figure 5.5) mean g^- state. Figures (a) and (b) show some representative conformations of the stretched and the compacted chains, respectively.

5.3.3 Mean Square Displacement and Diffusion Coefficient

The diffusion coefficient (D) of K^+ and Γ in tetraglyme was calculated from the MD slope of the mean square displacement (MSD) with respect to time, which the normal (Einstein) diffusion is observed. Mean square displacement is a linear function of time: $D = \frac{1}{6} \lim_{t \rightarrow \infty} d \langle r(t) - r(0) \rangle^2 / dt$, the brackets denote an ensemble average. D for K^+ and Γ were found in the same order of magnitude as the reported values (1.3×10^{-6} and $1.6 \times 10^{-6} \text{ cm}^2/\text{s}$, respectively). Interestingly, it was found that K^+ cations diffuse slightly slower than Γ anions. The possible explanations of this finding may be from an additional interaction of K^+ cation with tetraglyme oxygens.

For the diluted system (EO:K = 40:1), MSD of K^+ and Γ ions (not shown) are nearly similar. This suggests that K^+ and Γ ions are not actually separate and move together.

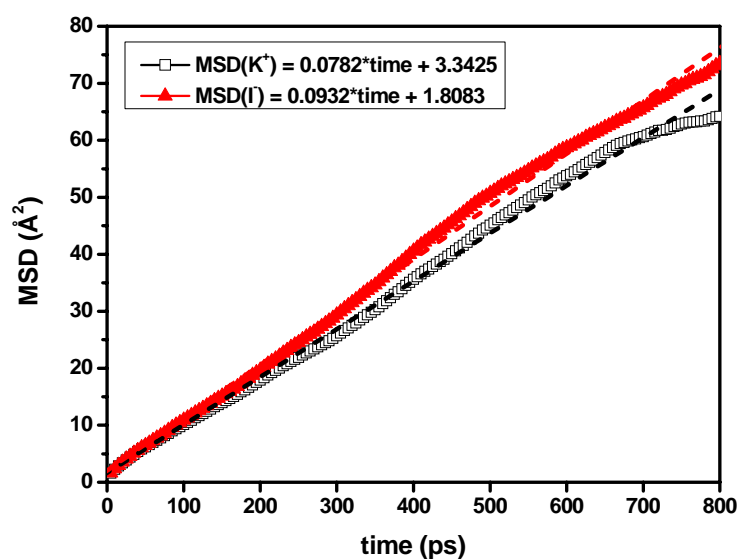


Figure 5.10 Mean square displacement of K^+ and Γ in tetraglyme:KI at 300 K.

5.4 Conclusions

To study the effect of adding KI salt on the properties of PEO-based electrolytes, MD simulations with COMPASS forcefield were performed on the tetraglyme:KI systems with an ether oxygen: K^+ mole ratio of 10:1. The results show that adding KI salt causes some changes in the structural, conformational, and dimensional properties of tetraglyme chains. The dihedral distribution functions show that the *gauche* conformations along both C–C and C–O bonds are increased whereas *trans* conformation is vanished when KI was added. The radius of gyration illustrates that adding KI salt causes the polymer chains become more compact which can be confirmed by an increase in *gauche* conformation. Integrating the K^+ –O and K^+ –I RDFs over the first coordination shells gives an average 2.4 oxygens and 3.1 iodide anions coordinated to each K^+ . This result indicates that there is a competition in complexation of K^+ between ether oxygens and iodide anions, and that the degree of coordination of K^+ by iodide anions is comparable to that by ether oxygens. The diffusion coefficient (D), which can be calculated from the slope of the mean square displacement, of K^+ cations is slightly lower than that of I^- anions which may result from an additional coordination of K^+ by ether oxygens. Thus, the interaction between K^+ cations and ether oxygens causes some changes in the properties of tetraglyme which may serve to enhance the ionic conductivity of longer PEO chain system as mentioned in the experimental results.

CHAPTER VI

MOLECULAR SIMULATIONS OF POLY(ETHYLENE OXIDE)-POTASSIUM IODIDE-TITANIUM DIOXIDE NANOCOMPOSITES

6.1 Introduction

Understanding the interface between polymer melts and solids is of fundamental importance in all practical applications where the properties of polymer-based materials are primarily regulated by the presence of solid components. This is the case, for instance, of industrially important systems such as polymer nanocomposites. Therefore, the polymer/solid interface has been the subject of several simulation studies in recent years. Molecular simulations provide an excellent opportunity to directly study the influence of fillers on structure and dynamics of polymers, since detailed information on the properties near a filler surface is difficult to obtain experimentally. Monte Carlo (MC) and Molecular Dynamics (MD) simulations performed for various polymer models near planar solid surfaces indicate that molecular arrangements, conformations and dynamics of the polymer are strongly perturbed with respect to the isotropic bulk. The strength of polymer-interface interaction and filler specific surface area were the most important factors controlling the properties of the interfacial polymer. The addition of fillers with attractive interactions led to decreased polymer dynamics and increased viscosity, whereas

the addition of fillers with the repulsive, or excluded volume, interactions led to increased polymer dynamics and decreased viscosity (Smith, Bedrov, Li, and Bytner, 2002; Starr, Schröder, and Glotzer, 2002). These effects were found to scale linearly with the specific surface area of the fillers (Smith, Bedrov, Li, and Bytner, 2002).

The addition of ceramic nanoparticles to polymer electrolytes, initially done to enhance mechanical properties, has also been found to improve the anodic stability, cyclability, sometimes conductivity, and cation transfer number of polymer electrolytes without causing any observed degradations. A fundamental understanding of the mechanisms responsible for the dramatic changes in polymer electrolyte properties with the addition of nanoparticles is lacking. In this section, MD simulations with COMPASS forcefield were performed on the PEO/TiO₂ and the more complicated PEO/KI/TiO₂ systems in order to understand the influence of TiO₂ interface and free surface on the structural and dynamical properties of PEO-KI based polymer electrolytes, which are potential candidates for an application in solvent-free dye sensitized solar cells. In addition, MC simulation of coarse-grained polymer nanocomposite model is performed to investigate the structures and dynamics at the longer time and length scale which is beyond the capacity of the current atomistic MD simulation method used in this work.

This chapter is organized in the following order. In Section 6.2, MD simulation methodology is described together with the simulated systems. The MD results are presented and discussed in Sections 6.3 and 6.4. In Section 6.5, the MC simulation of coarse-grained polymer interface models is described. Finally, the conclusions are presented in Section 6.6.

6.2 MD Simulation Methodology and System Description

MD simulation of PEO with one side confined to TiO₂ surface and the other side exposed to vacuum was performed. Ten PEO chains with the structure of H-(CH₂-O-CH₂)₅₄-H were used in the simulations. Each TiO₂ surface is comprised of four atomic planes or layers of 200 Ti and 400 O from the (110) direction of an anatase crystal that is about 10 Å thick and the cross section is 26.7, 27.2 and 170.7 Å in the *x*, *y* and *z* dimensions, respectively. COMPASS forcefield was used to describe PEO-PEO and PEO-TiO₂ interactions. All MD simulations were performed at 300 K using Discover module in Materials Studio 4.2 simulations package provided by National Nanotechnology Center of Thailand. A Nosé-Hoover thermostat was used to control the temperature, and bond lengths were constrained by SHAKE algorithm. The Particle-Mesh Ewald (PME) technique was selected for Coulomb interactions.

For the PEO/KI/TiO₂ system, ten PEO chains with the same structure as presented in the PEO/TiO₂ system plus 54 K⁺ and 54 I⁻ (an ether oxygen:K⁺ mole ratio of 10:1) were used. The simulation methodology was the same as the previous PEO/TiO₂ system. Bulk PEO and PEO/KI mixture without TiO₂ nanofillers were also studied as the reference systems. Figures 6.1 (a) and 6.1 (b) shows the models of the PEO/TiO₂ and the PEO/KI/TiO₂ systems, respectively.

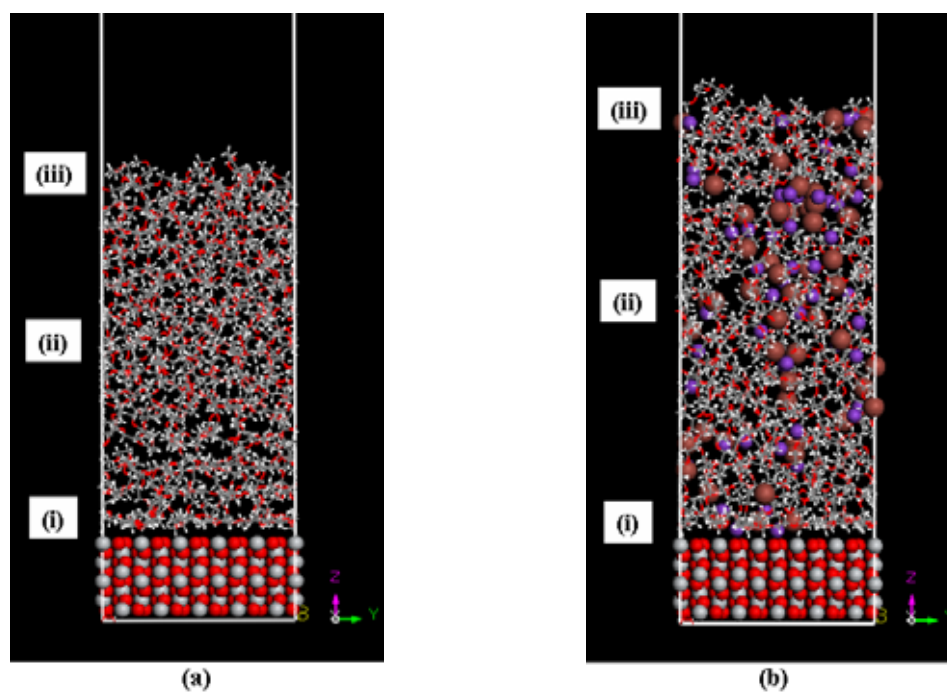


Figure 6.1 Snapshots of (a) PEO and (b) PEO/KI confined one side to TiO₂ surface and the other side to vacuum from NVT-MD simulations at 300 K. There are three regions: (i) PEO/TiO₂ interface, (ii) PEO bulk, and (iii) PEO/vacuum surface (colors: hydrogen atoms–white, oxygen–red, carbon–grey, titanium–grey balls, potassium cations–purple balls, and iodide anions–brown balls).

6.3 Results and Discussion for PEO/TiO₂ Nanocomposites

6.3.1 Structural Properties

The influence of TiO₂ interface and free surface on PEO structure was investigated by analyzing the total density profile of all PEO atoms normal to TiO₂ interface to free surface as shown in Figure 6.2 (a). In Figures 6.2 (b) and 6.2 (c), the PEO density profiles near the TiO₂ interface and near the free surface are plotted, respectively. The PEO density profile near the TiO₂ interface is sharper compared to the free surface. The PEO density is perturbed strongly up to approximately 12-15 Å from TiO₂ interface, with the PEO density further than that becoming flat. Hence, the chain segments in contact with the TiO₂ interface are arranged in densely packed and ordered layers as seen in Figure 6.3. PEO at TiO₂ interface is divided into three interfacial layers based on the minima of the density profile as seen from Figure 6.2 (b) by the dotted lines and also from the simulation snapshot (Figure 6.3). The thickness for each layer is around 4 Å. In the free surface region, PEO density is lower and the interfacial profile become broader (*ca.* 10 Å) as seen in Figure 6.2 (c).

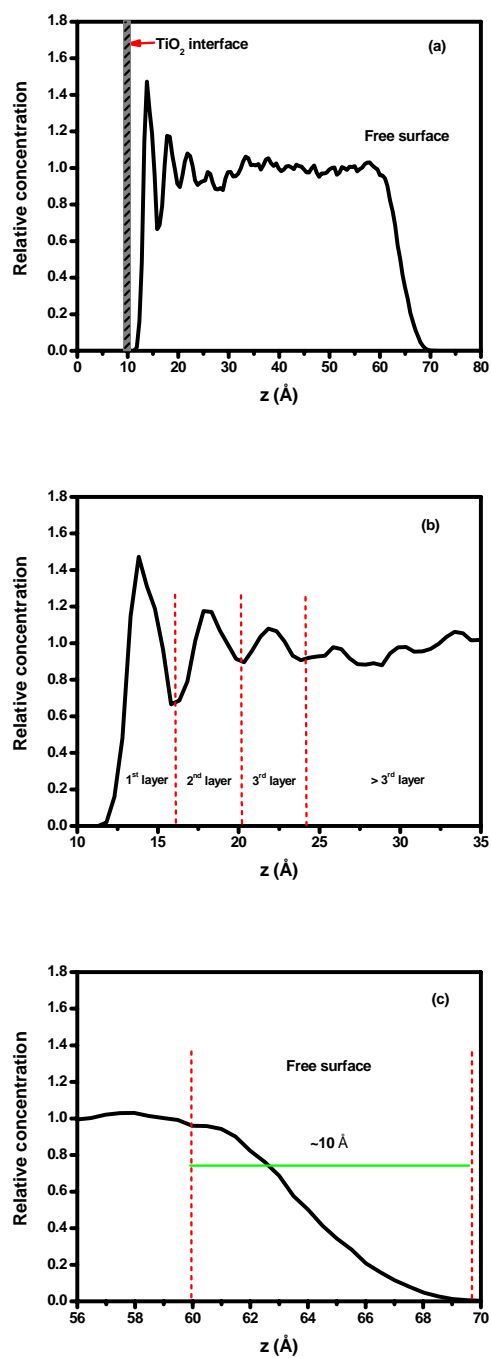


Figure 6.2 The total density profile of all PEO atoms (a) from TiO_2 interface to free surface, (b) near the TiO_2 interface, and (c) near the free surface. Vertical dashed lines in Figure (b) indicate division into interfacial layers.

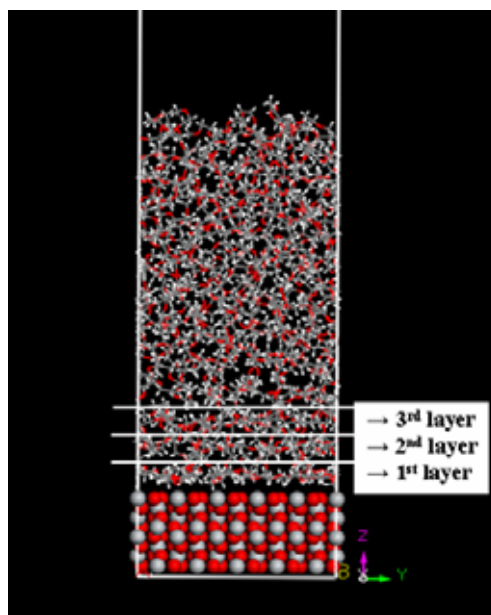


Figure 6.3 The MD snapshot of PEO/TiO₂ system. The PEO at the TiO₂ interface is divided into three interfacial layers with dense packing and ordering.

6.3.2 Interaction Energy

Interaction energy was calculated according to Equation 6.1. At first, the total energy (E_{total}) for the simulation box containing both PEO and TiO₂ surface atoms was calculated and then, the energy of PEO ($E_{polymer}$) was calculated without any contribution from the surface. Finally, the surface atoms were kept and PEO was removed to calculate the energy of surface ($E_{surface}$). The interaction energy ($E_{interaction}$) of PEO and TiO₂ surface was then computed as:

$$E_{interaction} = E_{total} - (E_{surface} + E_{polymer}) \quad (6.1).$$

The calculations gave $E_{Interaction} = -186.69$ kcal/mol. The large negative value of interaction energy indicates that there is a strong attractive interaction between PEO chains and TiO₂ interface.

To investigate the pair interaction between the atoms of TiO₂ interface and those of PEO chains, the radial distribution functions (RDFs) of Ti and PEO atoms *i.e.* C, H, and O_{et} (ether oxygen), as well as O_{ti} (oxygen of TiO₂) and PEO atoms were calculated as shown in Figures 6.4 (a) and 6.4 (b), respectively. Figure 6.4 (a) demonstrates that the RDF between Ti atoms and O_{et} is the sharpest and closest to the interface (the first peak is at 2.77 Å) compared to other atom pairs, whereas Figure 6.4 (b) shows that the RDF peak between O_{ti} and H in PEO is the sharpest and shortest in the pair distance (the first peak is at 2.65 Å). This should be due to the strong electrostatic interactions between atom pairs with the opposite partial charges as listed in Table 6.1.

Table 6.1 Partial charges of atoms in MD simulations of PEO/TiO₂ interface.

Atoms	Partial charges (e)
Ti	1.600
O _{ti}	-0.800
O _{et}	-0.320
H	0.053
C	0.054
K ⁺	1.000
I ⁻	-1.000

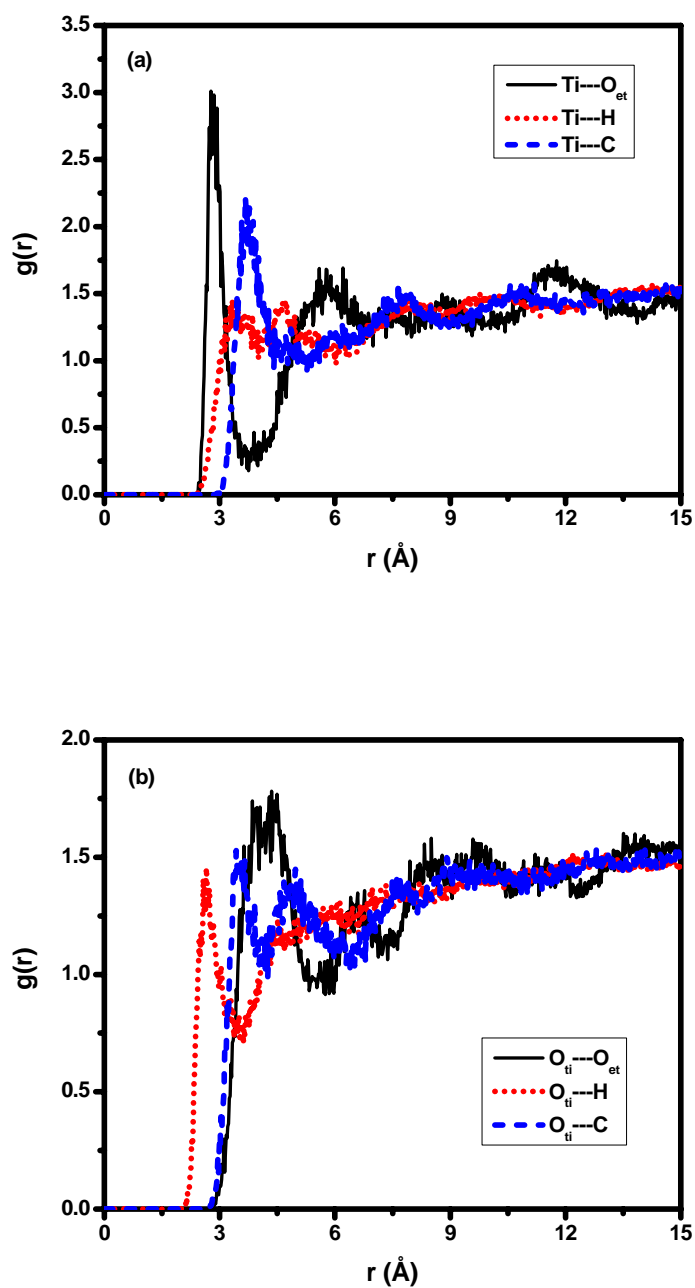


Figure 6.4 RDFs of (a) Ti atoms and PEO atoms with C, H, ether oxygen (O_{et}), and (b) TiO₂ oxygen atoms (O_{ti}) and C, H, O_{et}.

The interaction between TiO₂ and PEO chains revealed by MD simulations should be related to a reduction of PEO crystallinity upon adding TiO₂ nanoparticles as observed from X-ray powder diffraction (XRD) result. PEO (Aldrich, $\overline{M}_w = 4 \times 10^6$ g/mol), TiO₂ nanoparticles (Degussa P25), and acetonitrile (Mallinckrodt, USA) were used to prepare PEO/TiO₂ nanocomposite thin film. These samples were measured by Bruker D5005 power diffractometer (Cu K_α radiation) in the 2θ range of 5°-50°. For example, the XRD patterns of the PEO/TiO₂ nanocomposites with 5 and 10 wt.% TiO₂ compared with the XRD pattern of pure PEO sample are shown in Figure 6.5. For PEO/TiO₂ nanocomposites, the intensity of XRD peaks is obviously lower than that of pure PEO sample. This indicates that adding TiO₂ nanoparticles to PEO can reduce the degree of crystallinity which is consistent with previous MD simulation results. Therefore, TiO₂ should disintegrate the crystalline portion of PEO and the amount of the crystallinity decrease. It is expected that an increase in the ionic conductivity of PEO/KI/TiO₂ as reported in past publications should be related to larger amount of amorphous portion in polymer matrix rather than the change in salt dissociation upon adding TiO₂ nanoparticle. The MD results of PEO/KI/TiO₂ will be presented next in Section 6.4 to verify this assumption.

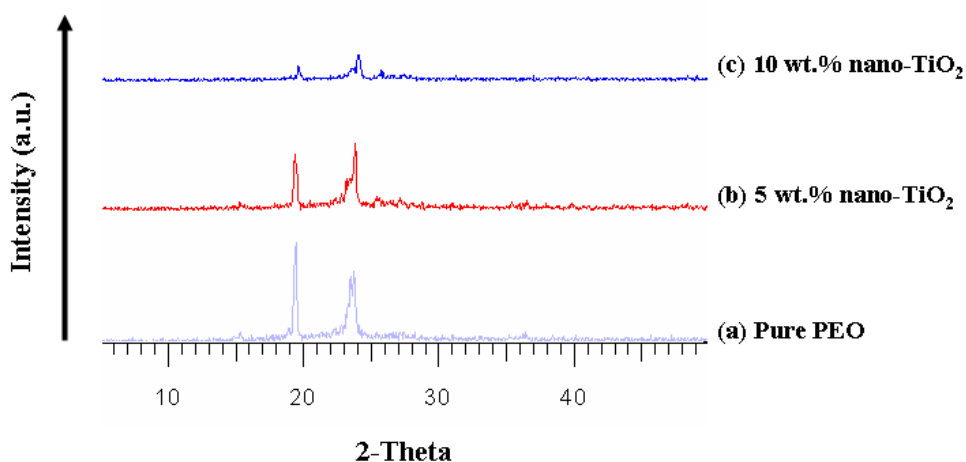


Figure 6.5 XRD patterns of (a) pure PEO, (b) and (c) PEO/TiO₂ nanocomposites with 5 and 10 wt.% TiO₂ nanoparticles, respectively.

The interaction of TiO₂ nanofillers with PEO molecules may induce structural modification of polymer chains which provides favorable conduction path for faster migration of ions (Croce *et al.*, 1998, 1999) and could render the polymer in the amorphous phase even at the moderate temperature (Lin *et al.*, 2005). The restriction of crystallization and an increase in the amorphous phase could be considered as the reason for the higher mobility of charge carriers (Liu, Lee, and Hong, 2003). It was also found that the interaction of TiO₂ with PEO chains promotes a network with improved mechanical stability of the film (Croce *et al.*, 1999), as well as the TiO₂ nanofillers can prevent the re-crystallization in the PEO-based composite polymer electrolyte (Lin *et al.*, 2005).

6.3.3 Dynamical Properties

To examine the influence of TiO_2 interface on PEO translational dynamics, the backbone atom mean-square displacements (MSDs) were calculated for each PEO layer as shown in Figure 6.6. Figure 6.7 illustrates the PEO layers divided for calculating the MSDs. PEO backbone atoms in the first layer (4 Å thick) adjacent to TiO_2 interface moved significantly slower than those in the bulk PEO. The PEO dynamics in the second layer, however, was perturbed less than that in the first layer, whereas the MSDs of PEO atoms in the third layer and beyond were almost the same as in the bulk. For the dynamics in the free surface region, PEO translation was found to increase due to a drop in local density at the free surface region.

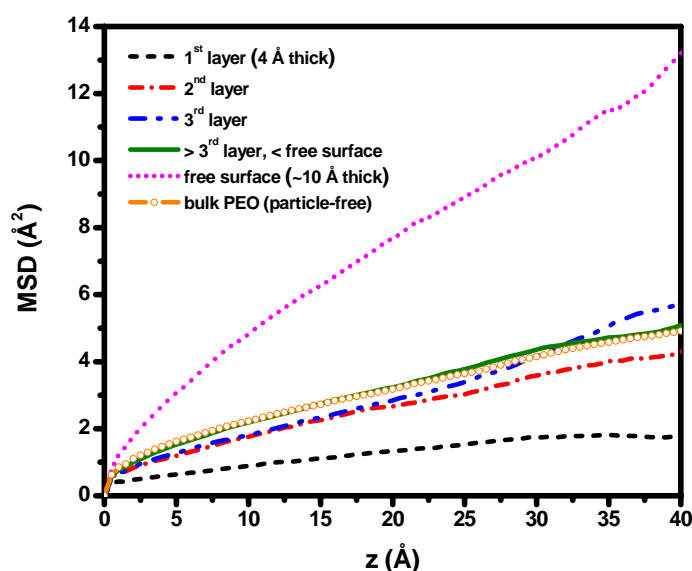


Figure 6.6 Backbone atom MSDs for each PEO layer (*dashed line, dash-dot line, dash-dot-dot line, solid line, and dotted line* for the 1st layer, 2nd layer, 3rd layer, > 3rd layer, and free surface, respectively) and for bulk PEO (*solid line with circle*).

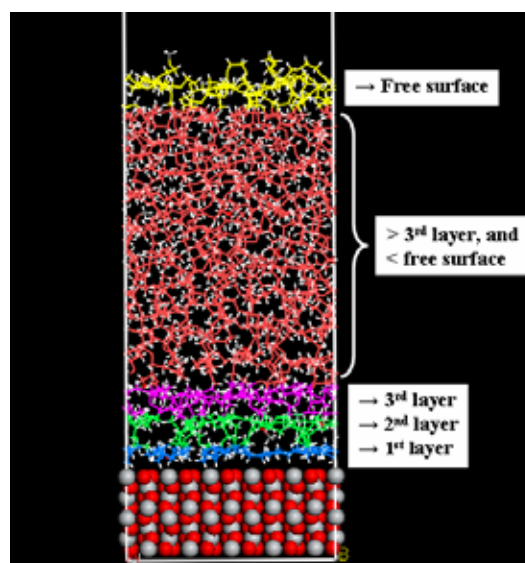


Figure 6.7 The PEO divided into five layers: 1st layer (blue), 2nd layer (green), 3rd layer (pink) with ~ 4 Å thickness for each, more than 3rd layer and less than free surface (red), and free surface (yellow) with ~ 10 Å thickness.

6.4 Results and Discussion for PEO/KI/TiO₂ Nanocomposites

6.4.1 Structural Properties

The effect of TiO₂ nanofiller on the SPEs properties was analyzed by investigating the structure of SPEs near the TiO₂ interface. The density profiles of PEO, K⁺, and I⁻ calculated as a function of the normal distance from the interface are shown in Figure 6.8. The pattern of the PEO density profile is similar to that of the system without added salt *i.e.* (1) the PEO density profile near the TiO₂ interface is sharper compared to the free surface, (2) the PEO density is perturbed strongly up to ~ 15 Å from TiO₂ interface with the PEO density further than that becoming roughly flat, (3) the PEO at the TiO₂ interface is divided into three interfacial layers with ~ 4 Å thickness, as well as (4) the PEO density is lower and the interfacial profile become

broader (*ca.* 10 Å) at the free surface region. However, Figure 6.9 shows that the PEO density in PEO/KI/TiO₂ system is lower than that in the bulk region and the film is thicker than the PEO/TiO₂ system. Figure 6.8 demonstrates that both cations (*dotted line*) and anions (*dash-dot line*) prefer to locate outside the highly structured PEO region (> 15 Å from the interface), especially near the free surface region where the PEO density is dropped. Near TiO₂ interface (< 5 Å from the interface), ions are rarely found especially for K⁺ cations. This is probably due to the large entropic penalty required to change PEO conformations (Borodin and Smith, 1998) and structure from the highly structured interfacial PEO (Borodin, Smith, Bandyopadhyaya, and Buytner, 2003) to PEO complexed by K⁺, whereas the reduced free volume in the first interfacial PEO layer prevented I⁻ accommodation. In addition, also as seen in Figure 6.8, K⁺ and I⁻ ions exhibit strong correlation for their position indicating high ionic association between these ion pairs.

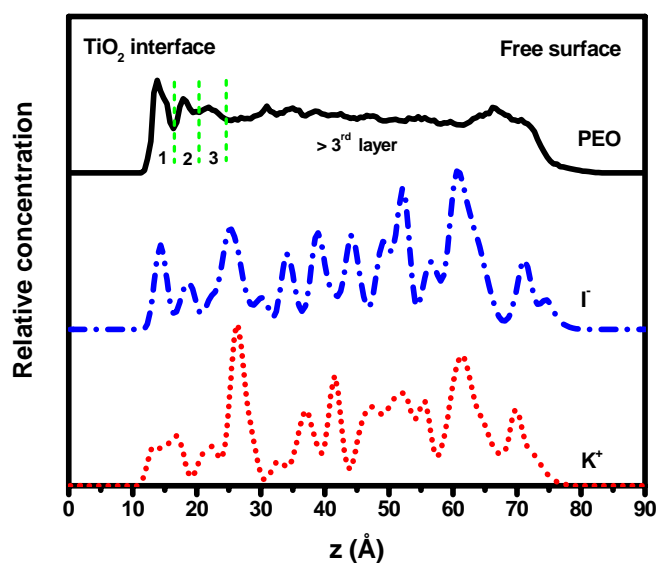


Figure 6.8 The PEO (*solid line*), K^+ (*dotted line*), and Γ (*dash-dot line*) density profiles from TiO_2 interface to free surface of the PEO/KI/ TiO_2 composite at 300 K. Vertical dashed lines indicate the division into three interfacial PEO layers.

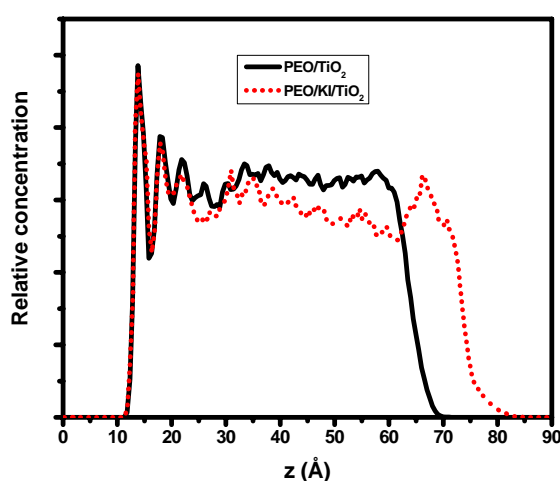


Figure 6.9 The PEO density profile of the PEO/KI/ TiO_2 nanocomposite (*dotted line*) compared with that of the PEO/ TiO_2 nanocomposite (*solid line*).

To investigate the interaction between TiO₂ surface and PEO/KI electrolyte, radial distribution functions (RDFs) between TiO₂ atoms and PEO/KI species *i.e.* C, H, O_{et}, K⁺, and I⁻ were calculated as shown in Figure 6.10. The position of the first RDF peaks for all pair interactions are listed in Table 6.2. Figure 6.10 (a) demonstrates that the RDFs between Ti atoms and O_{et} (*thin solid line*), as well as Ti atoms and I⁻ anions (*strong solid line*) are sharp and close to the interface (the first peaks are at 2.78 Å, and 3.67 Å, respectively). Figure 6.10 (b) illustrates that the RDFs between O_{ti} atoms and K⁺ cations (*strong solid line*) is the sharpest and closest to the interface (the first peak is at 2.73 Å), indicating the strong O_{ti}-K⁺ interaction. This should be due to the electrostatic interactions between atom pairs with the opposite partial charges as listed in Table 6.1. The strong RDFs peaks of O_{ti}-K⁺ and Ti-I⁻ may reduce the dynamics of those ions in the first interfacial layer as shown in calculated MSDs (Figure 6.13). For the PEO/KI/TiO₂ system, the pattern of the RDFs peaks between TiO₂ atoms and PEO atoms (C, H, O_{et}) is similar to that of the PEO/TiO₂ system but the intensities of RDFs peaks are slightly lower as shown in Figure 6.11, implying that there are additional interactions between TiO₂ atoms and ions (K⁺, I⁻) that mediate the interaction between PEO atoms and ions. However, it should be noted that the number of both K⁺ and I⁻ ions is low near the TiO₂ interface which leads to no significant change in the pattern of PEO density profile in the first three interfacial layers ($z < 25$ Å) compared with the PEO/TiO₂ system as seen in Figure 6.9.

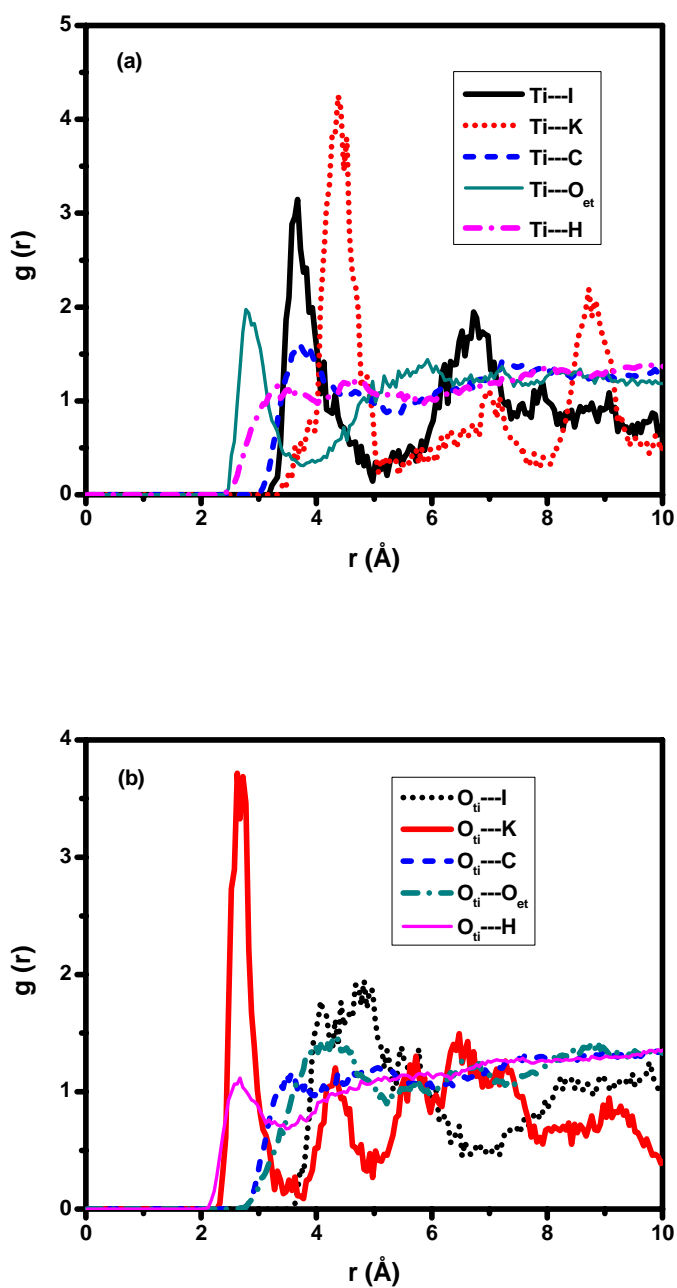


Figure 6.10 RDFs between (a) Ti atoms and PEO/KI species (*i.e.* C, H, O_{et}, K⁺, and Γ), and (b) O_{ti} atoms and PEO/KI species at 300 K.

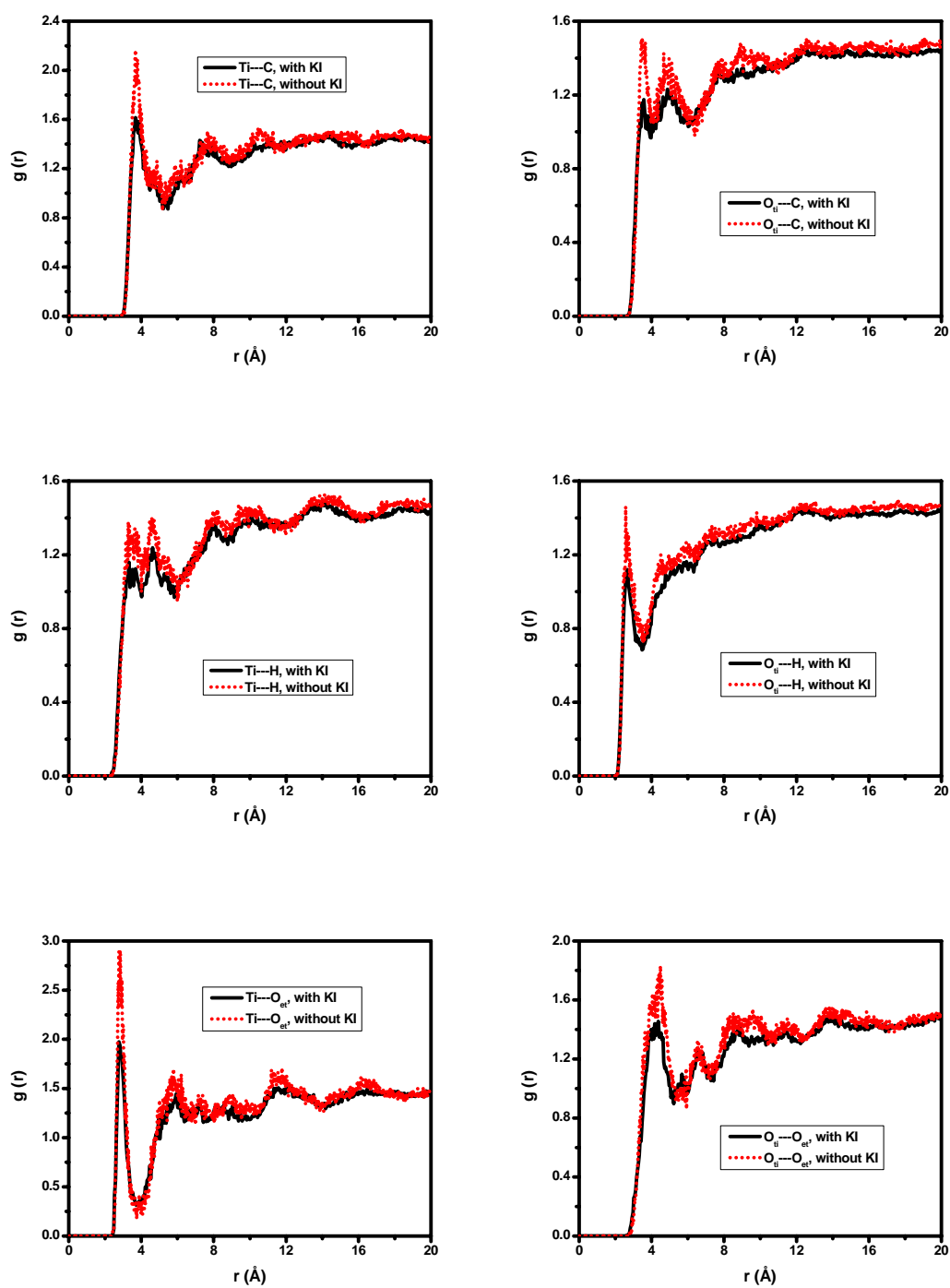


Figure 6.11 Comparison of the RDFs between TiO_2 atoms (Ti, O_{ti}) and PEO atoms (C, H, O_{et}) of PEO/ TiO_2 nanocomposites with added KI (solid lines) and without added KI (dotted lines).

Table 6.2 The first RDFs peak positions for all pair interactions in the PEO/KI/TiO₂ system at 300 K.

Atom pair		The first peak position (Å)
Ti	K ⁺	4.38
	I ⁻	3.67
	C	3.67
	H	3.33
	O _{et}	2.78
O _{ti}	K ⁺	2.73
	I ⁻	4.82
	C	3.58
	H	2.67
	O _{et}	4.38

To determine the effect of TiO₂ slab on the dissociation of KI salt, RDFs between K⁺ and I⁻, as well as coordination number of I⁻ (CN_I) of the PEO/KI electrolytes with and without added TiO₂ nanofiller were calculated as shown in Figure 6.12 (a). The K⁺-I⁻ distance and CN_I for the first coordination shell are listed in Table 6.3. In Figure 6.12 (a) and Table 6.3, the pair distance and the coordination number almost unchanged for both systems, indicating that no significant effect of TiO₂ slab on KI salt dissociation can be observed in this complex. This finding corresponds to the MD simulation result of LiBF₄-PEO system containing Al₂O₃ nanofillers studied by Kasemägi *et al.* (2002). For the LiBF₄-PEO nanocomposites,

ion pairing and clustering occur in the regions away from the surfaces for all three systems *i.e.* LiBF₄-PEO nanocomposites with Al₂O₃ nanoparticles and Al₂O₃ slab, and LiBF₄-PEO system without nanoparticles), but it is the largest for the “slab” system and smallest for the “particle” system. Since less ion clustering is found in the “particle” system than in the “particle-free” system, it can be concluded that nanoparticles serve to dissociate LiBF₄ salt. This effect is not so clear in the “slab” system, where the ion clustering is larger.

Figure 6.12 (b) shows the comparison of the K⁺-O_{et} RDFs for PEO/KI and PEO/KI/TiO₂ systems. From Figure 6.12 (b) and Table 6.3, there are no significant differences in the K⁺-O_{et} distance (R_{K-O}) and the coordination number of ether oxygens (CN_O) for the first coordination shell between the different systems. Beyond the distance after the first peak, less coordination number of K⁺-O_{et} is observed for the PEO/KI/TiO₂ system only in the region 3-5 Å. After 5 Å, the situation seems to reverse. Thus, it may be said that the first coordination shell of K⁺-O_{et} is slightly changed because K⁺ might interact with O_{ti} as well as O_{et} might interact with Ti. As suggested by Figure 6.10, the Ti-O_{et} and O_{ti}-K⁺ distances for the first RDF peaks are around 3 Å.

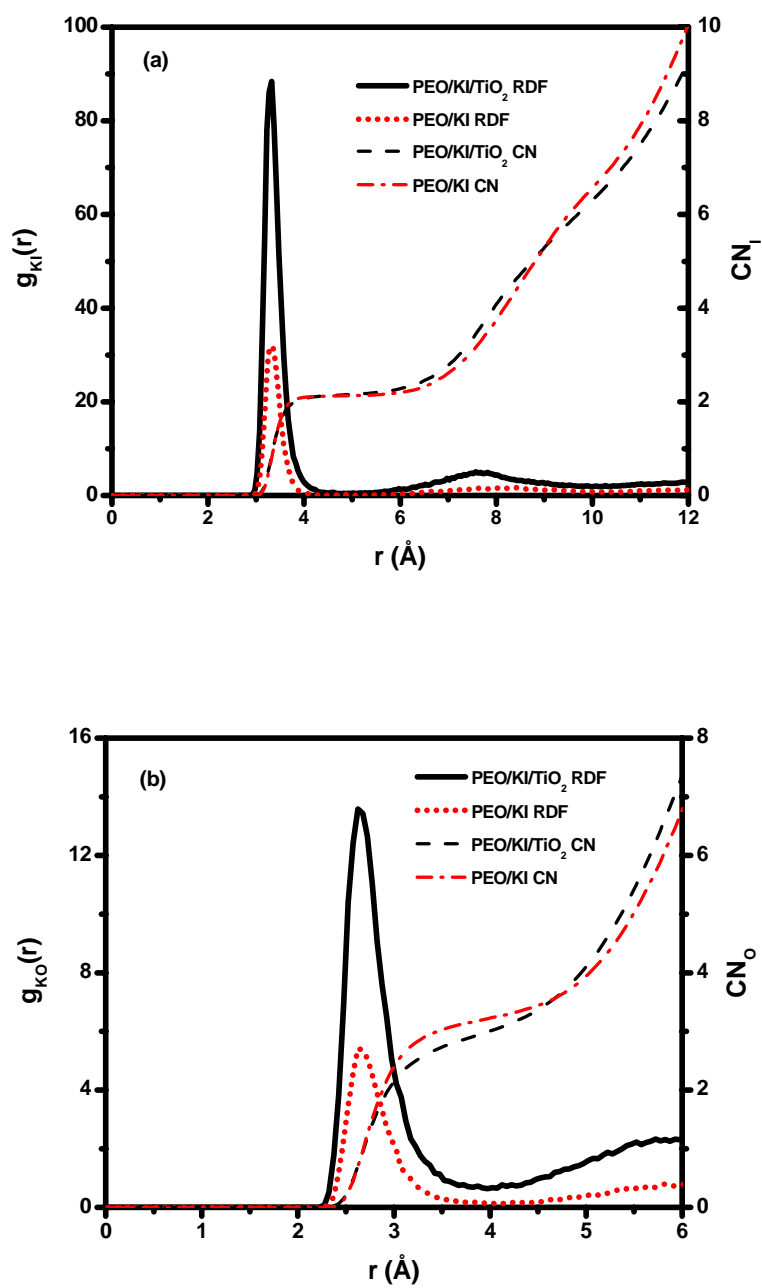


Figure 6.12 RDFs and CN for (a) K^+-I^- , and (b) K^+-O_{et} for PEO/KI with EO:K = 10:1 (filler-free), and TiO₂ slab in PEO/KI with EO:K = 10:1.

Table 6.3 The pair distances (R_{K-I} , R_{K-O}) and the coordination numbers (CN_I , CN_O) for the first coordination shell of the PEO/KI (filler-free) and the PEO/KI/TiO₂ systems at 300 K.

Systems	Pair Distances		Coordination Numbers	
	R_{K-I} (Å)	R_{K-O} (Å)	CN_I	CN_O
PEO/KI/TiO ₂	3.33	2.62	2.1	3.0
PEO/KI	3.33	2.62	2.1	3.2

6.4.2 Dynamical Properties

The effect of the TiO₂ nanofiller on the dynamical properties of SPEs is investigated in this section. The PEO/KI sheet in the slab model was divided into zones parallel to the TiO₂ interface: (1) < 5 Å (“near TiO₂ interface”), (2) > 5 Å (“away from TiO₂ interface”), and (3) free surface with ~ 10 Å thickness. MSDs of K⁺, and I⁻ for each layer were compared with those of bulk SPEs as shown in Figure 6.13. In Figure 6.13 (a), one of the most important effects of TiO₂ interface is observed: the slope of the mean-square displacement (MSD) for K⁺ cations “away from TiO₂ interface” (directly proportional to K⁺ self-diffusion coefficient and conductivity) is at least twice as large as in the system without nanofiller, whereas the motion of K⁺ cations at the free surface region is about one order of magnitude faster than that of the particle-free system. Closer to the TiO₂, the mobility of K⁺ cations decreases greatly. It is remarkable that K⁺ cations have no mobility in the region < 5 Å from the TiO₂ interface. For the mobility of iodide anions as depicted in Figure 6.13 (b): near

the TiO₂ interface, the mobility is very slow. There is still a slight mobility for I⁻ in the region < 5 Å from the slab surface, where K⁺ cations have no mobility at all, indicating that K⁺/TiO₂ interaction is stronger than I⁻/TiO₂ interaction as supported by the O_{ti}-K⁺ and Ti-I⁻ RDFs (Figure 6.10). The MSD of I⁻ anions away from TiO₂ interface is approximately five times larger than that of the bulk SPEs, whereas the motion of I⁻ anions at the free surface region is about one order of magnitude faster than that of the particle-free system. In Figure 6.13 (c), the MSDs of K⁺ cations for each region and for the bulk SPEs are compared to those of I⁻ anions. It is clearly seen that I⁻ anions always move faster than K⁺ cations for all regions. This is probable due to the complexation of K⁺ cations with ether oxygens of PEO chains as seen in the K⁺-O_{et} RDF (Figure 6.12 (b)) that hinders the K⁺ movement. The high mobility of ions beyond the first interfacial layer from TiO₂ interface (> 5 Å) may cause the enhancement of the ionic conductivity of the SPEs/TiO₂ nanocomposites as reported in the literatures (Croce *et al.*, 1999; Capiglia, Mustarelli, Quartarone, Tomasi, and Magistris, 1999; Kumar and Scanlon, 1999; Lin *et al.*, 2005). The MSD plot for the PEO backbone atoms shown in Figure 6.14 indicates that PEO backbone atoms in the first interfacial layer (< 5 Å) are significantly slower than those in the filler-free system and those away from the TiO₂ interface (> 5 Å), which is similar to the result of the PEO/TiO₂ nanocomposite electrolyte.

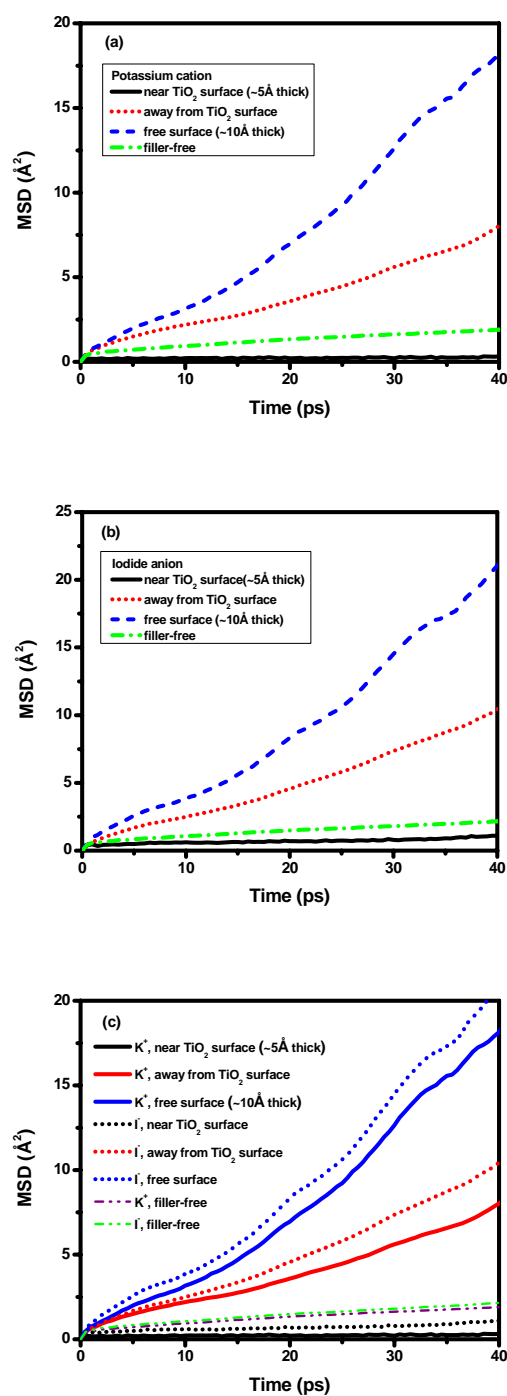


Figure 6.13 MSDs of (a) K^+ , (b) I^- , and (c) both K^+ and I^- for each region (near TiO_2 interface, away from TiO_2 interface, and free surface) compared with those of bulk.

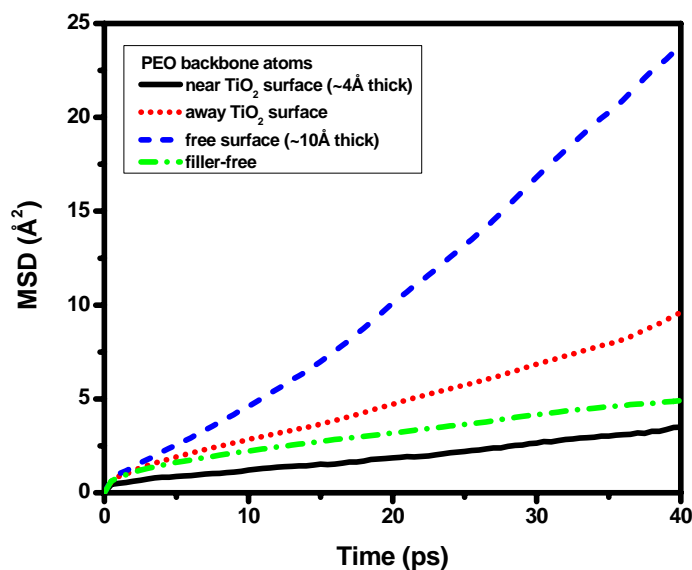


Figure 6.14 MSDs of PEO backbone atoms for each region: near TiO₂, away from TiO₂ interface, and free surface compared with those of bulk.

6.5 Monte Carlo Simulations for Polymer Nanocomposites

In this section, structures, dynamics and crystallization of an amorphous polymer melt model containing nanofillers with flat interface are investigated by MC simulations of coarse-grained polyethylene (PE) model on a high coordination lattice. This PE model was selected because its chemical structure is very similar to PEO and it is very much simpler to simulate this PE model via MC technique.

6.5.1 Materials and Methods

In this study, the simulations performed used a coarse-grained rotational isomeric state (RIS) model for the short PE chains. There are 155 PE chains, and each chain is represented by 20 beads which corresponds to *n*-tetracontane (C₄₀H₈₂). The

chains were represented on a high coordination lattice *i.e.* second-nearest-neighbor diamond (SNND) lattice. The simulations were performed at a temperature of 473 K, which is above the melting point of PE model used in this simulation. The systems represent bulk material with flat interface. The simulation box size is 24×24×29 lattice units (step length 2.5 Å) in the x , y and z dimensions, respectively. Nanofillers with flat interface are 5 lattice units thick located at both sides in the z dimension. This box has PE site occupancy of 22.4% correspond to the density of crystalline PE. The simulation method employed Metropolis Monte Carlo algorithm, which effectively samples the conformational space, for the coarse-grained model of PE chain on a second-nearest-neighbor diamond (SNND) lattice. The RIS model was incorporated into the simulation to calculate the short-range interaction resulting from local conformation of chain. The long-range intramolecular and intermolecular interaction potential energies were calculated using a lattice based approximation of the Lennard-Jones potential between monomers and between monomers and filler surfaces. The RIS model for the unperturbed PE has the values of the first- (E_σ) and second-order (E_ω) short-range interaction energies of 2.1 and 8.4 kJ/mol, respectively (Abe, Jernigan, and Flory, 1966). The long-range interaction is obtained by modification of the classic technique for the description of the second virial coefficient of a nonideal gas using the Mayer f function (Rapold and Mattice, 1996) and the Lennard-Jones potential with the parameters of $\varepsilon/k_B = 185$ K and $\sigma = 4.4$ Å. This set of parameters was used in simulations of PE in the melt, thin films (Doruker and Mattice, 1998, 1999) and nanofibers (Vao-soongnern, Doruker, and Mattice, 2000) above the melting point. Discretization of this Lennard-Jones potential produces the long-range interaction energies at variant temperatures as listed in Table

6.4. The first shell has a strongly repulsive interaction because the distance between two beads on the lattice, 2.5 \AA , is smaller than the value of σ in the Lennard-Jones potential. The third shell has the largest attractive interaction at all temperatures, which leads to the cohesive nature of the thin film. Shells beyond the third have a weaker attraction (Rapold and Mattice, 1996), which plays little effect. Hence, only the first three shells are applied in this simulation. The cutoff radius of the long-range energy was three lattice units (7.5 \AA). The energetic interaction $u(r)$ between polymer beads and nanofillers was defined using the same Lennard-Jones potential as was used for the polymer to polymer interactions except it was multiplied by a prefactor ω . In this study ω was taken to be 0.1, 1.0, and 2.0 in separate simulations, representing repulsive, neutral, and attractive interactions, respectively.

Each system was equilibrated for at least 10 million Monte Carlo steps (MCS); then production runs of 10 million MCS were performed. For crystallization studies, the temperature was instantaneously dropped to 298 K, and the simulation was continued at 298 K. At least 10 million MCS was needed to observe the crystallization.

Table 6.4 Long-range interaction (kJ/mol) of coarse-grained C₂H₄ units at various temperatures

T (K)	1 st shell	2 nd shell	3 rd shell
473	15.048	0.620	- 0.625
460	14.659	0.580	- 0.626
440	14.056	0.517	- 0.627
420	13.448	0.453	- 0.629
400	12.835	0.388	- 0.630
395	12.681	0.371	- 0.631
390	12.527	0.355	- 0.631
380	12.198	0.322	- 0.632
350	11.281	0.220	- 0.635
298	9.625	0.038	- 0.642

6.5.2 Results and Discussion of Polymer-Wall Interface

6.5.2.1 Structures and Dynamics

6.5.2.1.1 Density Profile

The equilibrium structures of PE nanocomposite models with various polymer-filler interactions *i.e.* neutral, attractive, and repulsive at 473 K and 298 K (quenched from 473 K to 298 K) are illustrated in Figures 6.15 (a) and 6.15 (b), respectively. To investigate the influence of nanofiller interfaces on PE structures, density profiles of PE beads normal to nanofiller interfaces were analyzed as shown in Figures 6.16 (a), 6.16 (b), and 6.16 (c) for the melt state (473 K), the crystallization

(298 K), and both temperatures, respectively. Density profiles of PE beads as a function of z distance at 473 K were first discussed (Figure 6.16 (a)). For the neutral interface system, the density of PE beads is low at one interface side (low z) and then it slightly rises up to the highest value at the other interface side (high z). The average density for the neutral interface system is $\sim 1.0 \text{ g/cm}^3$. The higher density at the interface with high z is due to PE chains formed an order region as seen in left Figure 6.15 (a). For the attractive interface, the highest value of PE bead density is observed at both sides of interface and the density profile becomes flat with approximately constant value of 0.9 g/cm^3 (lower than the density of the neutral system) in the bulk region. For the repulsive interface, the density profile is a loop shape where the highest PE density is at the middle of the system and the density is dropped at both interface sides. The magnitude of PE bead density for all systems in the bulk and at interface can be ordered as:

$$\rho_{b, \text{repulsive}} > \rho_{b, \text{neutral}} > \rho_{b, \text{attractive}} \text{ and } \rho_{\text{intf}, \text{attractive}} > \rho_{\text{intf}, \text{neutral}} > \rho_{\text{intf}, \text{repulsive}}$$

where ρ_b is the bulk density and ρ_{intf} is the density at interface. These results are corresponding to the polymer-nanofiller interaction types and are consistent with Figure 6.15 (a).

For the system quenched from 473 K to 298 K (Figure 6.16 (b)), the trend of PE bead density profiles for all interactions is similar to the melt system that is $\rho_{b, \text{repulsive}} > \rho_{b, \text{neutral}} > \rho_{b, \text{attractive}}$ and $\rho_{\text{intf}, \text{attractive}} > \rho_{\text{intf}, \text{neutral}} > \rho_{\text{intf}, \text{repulsive}}$. The density profiles of the neutral interface system for both temperatures are almost unchanged indicating that chains cannot move to adjust themselves to form a more ordered packing. For the attractive interface system at 298 K, however, the density profile is very low (near zero) in the bulk region and very high at interface

(~12 times more than the bulk density) indicating PE chains are strongly pulled down to the interface as seen in Figure 6.15 (b) (center picture). For the repulsive interface system at 298 K, the density profile in the bulk region is quite smooth and the density value is around 1.2 g/cm^3 , slightly higher than the melt system, whereas the density profile becomes broader and drop near zero value at both interface sides. All results correspond to Figure 6.15 (b).

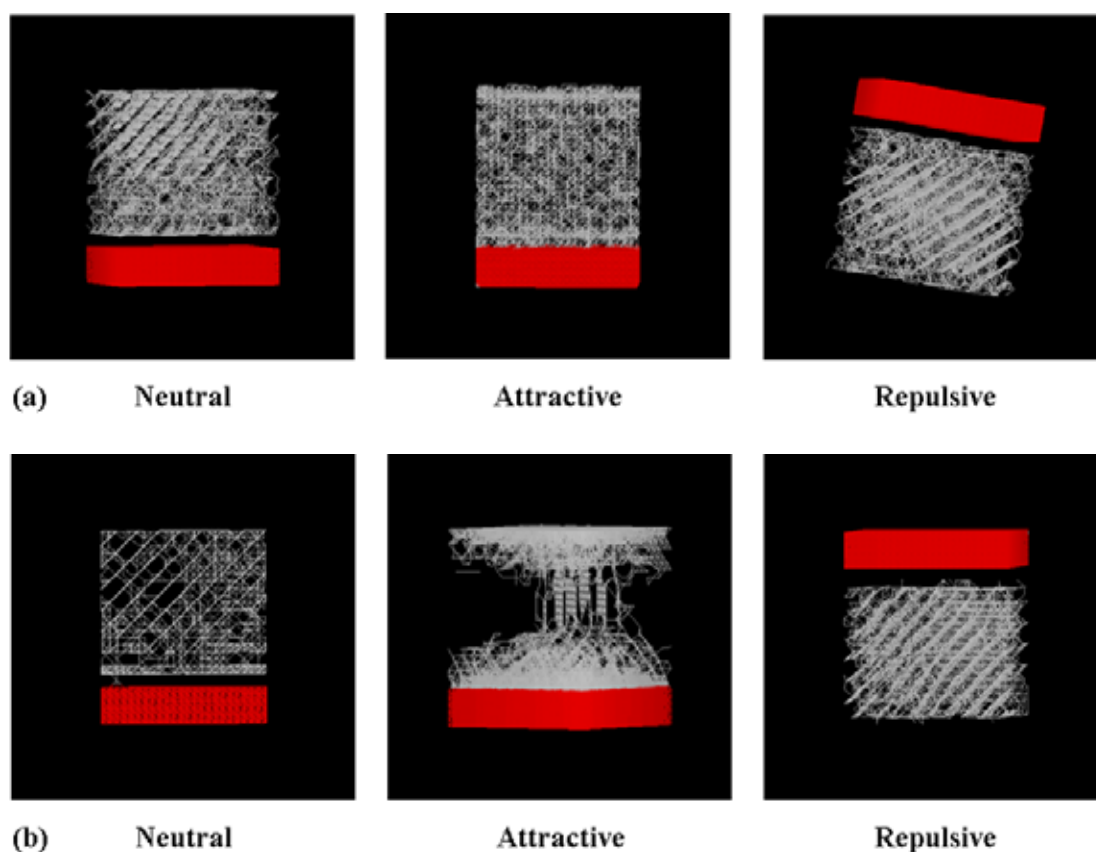


Figure 6.15 Snapshots of the final conformations of nanocomposites with various PE-filler interactions (neutral, attractive, and repulsive) at (a) 473 K, and (b) 298 K. Red color wall and gray wireframe denote the flat nanofiller and PE, respectively.

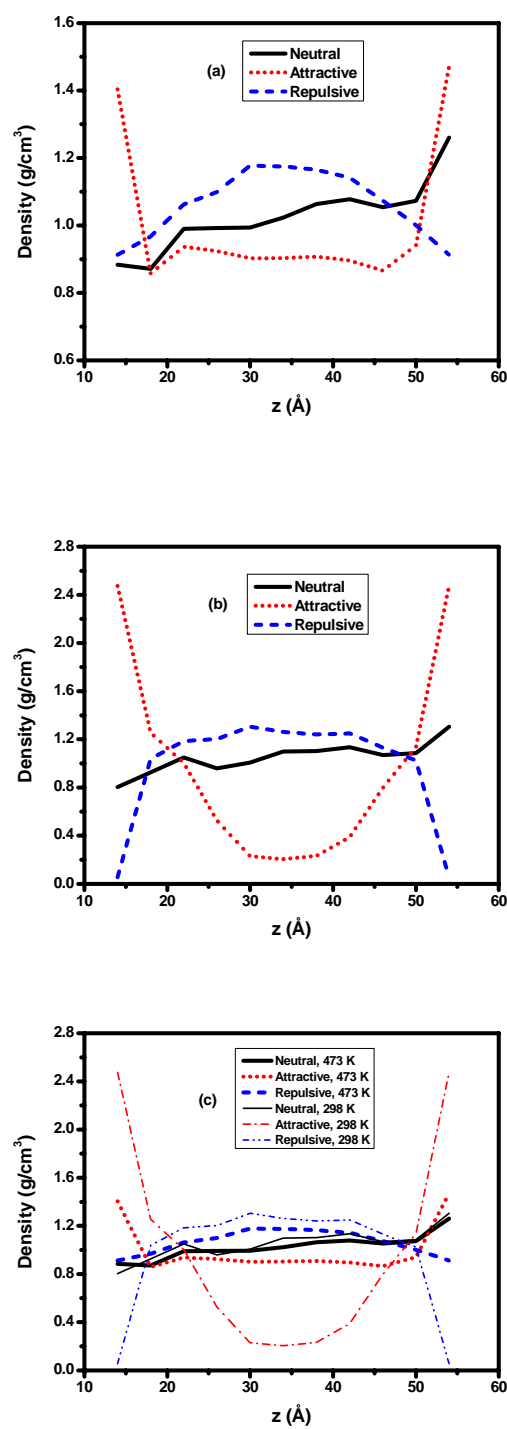


Figure 6.16 Density profiles of PE beads as a function of z distance (a) at 473 K (melt state), (b) 298 K, and (c) both temperatures.

6.5.2.1.2 Rotational Diffusion of Chains

Chain relaxation was monitored using the decay of the orientation of the end-to-end vector:

$$C(t) = \frac{\langle \vec{r}(t) \cdot \vec{r}(0) \rangle}{\langle r^2 \rangle} \quad (6.2)$$

Here $\vec{r}(t)$ is the end-to-end vector of a chain at time t . Relaxation of PE chains is presented in Figure 6.17. The relaxation of PE chains for the attractive interface system is the fastest, whereas it is the slowest for the repulsive one. The strong attractive interaction between PE chains and attractive interface causes PE chains were pulled down to the interface and consequently PE density is much lower at the bulk region as seen in Figure 6.15 (a) (center picture) and Figure 6.16 (a) (*dotted line*). Therefore, the relaxation of chains is more difficult near the interface, but it is enhanced in the bulk region which leads to the fastest chain relaxation. On the contrary, the strong repulsive interaction between PE chains and the repulsive wall causes PE chains to be squeezed in bulk region. Therefore, the relaxation of PE chains is the most difficult for this repulsive wall system.

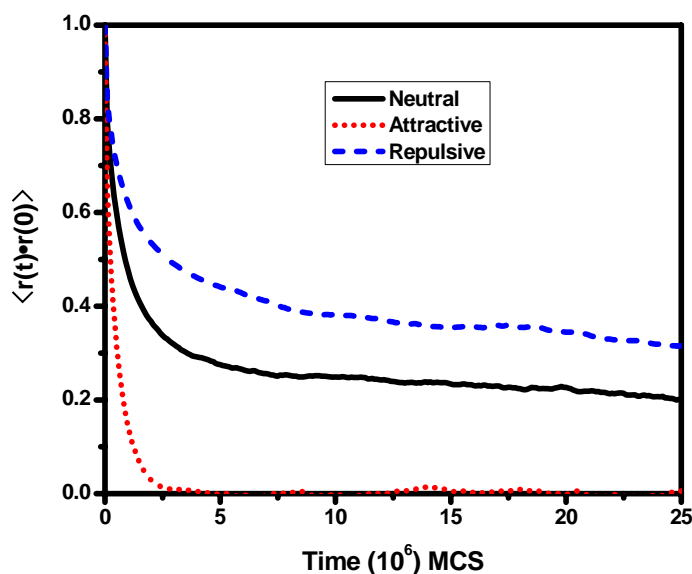


Figure 6.17 Normalized end-to-end vector autocorrelation functions of PE chains as a function of MCS for PE ($C_{40}H_{82}$) nanocomposites with neutral, attractive, and repulsive interactions at 473 K.

6.5.2.2 Bond Conformation for Crystallization

In order to investigate the structure formation process at the molecular level, it was then first examined how the conformational change takes place. Figure 6.18 depicts an evolution of the fraction of bonds in the *trans* state as a function of MCS after an instantaneous quench from 473 K to 298 K. As the simulation of the nanocomposite proceeds, the chains adopt more *trans* conformation. After 10 million MCS, the fraction of the bonds in the *trans* states approaches a limiting value about 73-83%. This value is smaller than that of the crystallization in the bulk (*ca.* 85%) by the same MC method. Therefore, chains adopt more *gauche* conformation for the crystallization in the nanocomposites. The attractive interface causes chain to adopt

more *gauche* conformation compared to the repulsive and neutral surfaces. Repulsive surface was found to enhance the rate of conformation changes to *trans* during the initial stage of structure formation. However, the *trans* fraction is about the same amount as for the neutral interface system.

This result indicates that the polymer-nanofiller interaction types influence on the fraction of the C-C bonds in *trans* state (directly relates to the crystallinity). Adding attractive nanofillers (*e.g.* TiO₂) may cause the lowest fraction of *trans* state compared to adding nanofillers with neutral and repulsive interactions. Hence, attractive nanofiller interfaces should have more effect on polymer conformation and consequently cause polymer chains to pack in a less order phase. Moreover, the fraction of *trans* state (~73%) for the attractive interaction filler is obviously lower than that in the bulk PE (~85%), supporting a reduction of the crystallinity of polymer nanocomposites, such as PEO/TiO₂ system, compared to the bulk as observed by available XRD and DSC data.

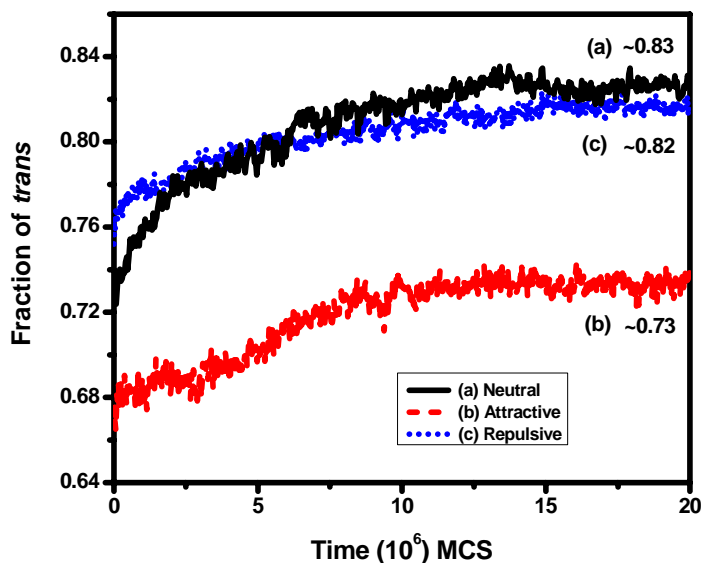


Figure 6.18 Fraction of C-C bonds that are in the *trans* state as a function of MCS after an instantaneous cooling of nanocomposite from 473 to 298 K.

6.5.2.3 Bond Ordering for Crystallization

The order parameter of all coarse-grained bonds, S_b , is defined by Equation 6.3.

$$S_b = \frac{1}{2}[3 \langle \cos^2 \theta \rangle - 1] \quad (6.3)$$

Here, θ denotes the angle between the chords (unit vector in coarse-grained polymer model), and the value of S_b is averaged for all pairs of chords in a given snapshot. S_b would assume a value of -0.5, 0.0 or 1.0, respectively, for chords characterized by perfectly perpendicular, random, and parallel orientation with respect to the reference vector. Figure 6.19 depicts the evolution of this parameter when the structure at 473 K is instantaneously dropped to 298 K. As the simulation proceeds at 298 K, this parameter increases from its value at 473 K and eventually reaches new equilibrium

values at 298 K. For S_b , the final value is in the range from 0.1 to 0.5, indicating the nanocomposite at 298 K has reached a state in which coarse-grained bond vectors are changed from randomly oriented to a more ordered structure. These results are in accord with the stretching of chain as seen in an increase in the fraction of *trans* as shown in Figure 6.18.

S_b increases steadily for the neutral and attractive wall systems while it reaches a plateau for the repulsive wall case. The magnitude of S_b is also different and can be ordered as: $S_{b, \text{repulsive}} \geq S_{b, \text{neutral}} > S_{b, \text{attractive}}$. This result suggests that chain orientation tends to align parallel to the wall interface. The repulsive wall provides the most space for polymer in the interface region. Therefore, polymer chains have more freedom to choose the *trans* conformation and result in the most chain orientation to the interface compared to the neutral and attractive interfaces. For the strong attractive interface, chain segments can rarely move and polymer conformation cannot orient themselves to align in the same direction. Therefore, $S_{b, \text{attractive}}$ gives the lowest value. All results are consistent with the Figure 6.15 (b).

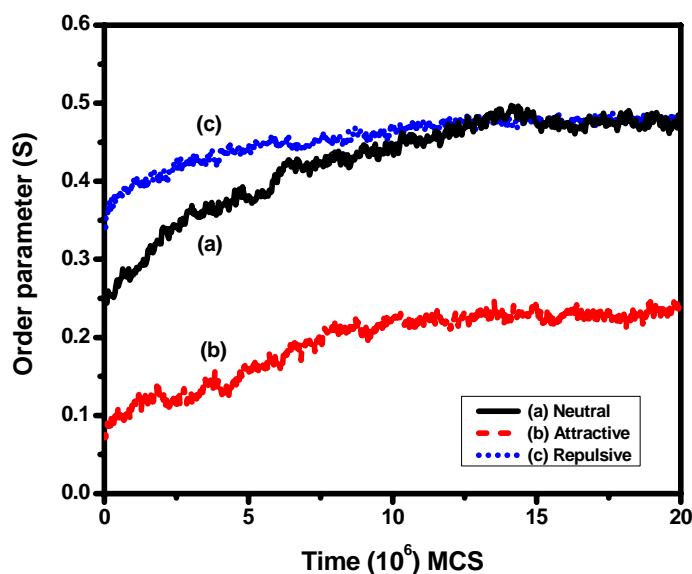


Figure 6.19 The bond orientation order parameter, S_b , as a function of MCS after an instantaneous cooling of the nanocomposites from 473 to 298 K.

6.6 Conclusions

MD simulation studies of the interface between PEO and TiO_2 nanocomposites and the free surface of PEO were performed to gain more understanding about the influence of TiO_2 interface and free surface on structural, and dynamical properties of these materials. MD simulations revealed that PEO density is significantly perturbed by TiO_2 interface and free surface, forming layers of highly dense polymer (compared to the bulk melt) that persisted up to 15 Å from the TiO_2 interface. At the free surface region, PEO density is lower and the interfacial profile is about the polymer size (*ca.* 10 Å). The calculation of interaction energy indicates that there is an attractive interaction between TiO_2 interface and PEO. The interaction

between PEO and TiO₂ causes not only a high of PEO density but also a slow down of chain dynamics at the interface region. This perturbation by TiO₂ may suppress the crystallinity of PEO and enhance the ionic conductivity of PEO-based nanocomposite electrolytes as mentioned in many available experimental results.

Moreover, MD simulations with COMPASS forcefield were applied to study the effect of TiO₂ interface on the structural and dynamical properties of PEO/KI electrolyte system. MD results revealed that the density profile and the dynamics of PEO backbone atoms are similar to the system without added salt. The slow PEO mobility of the highly dense PEO layer near the TiO₂ interface tends to expel most of the ions to the regions away from the TiO₂ interface, causing the relative increase in ionic concentration away from the TiO₂ interface. Moreover, this affects on the remarkably slow mobilities of both K⁺ and I⁻ ions near the TiO₂ interface, whereas the mobilities for the ions away from TiO₂ interface are clearly faster than those of the system without nanofiller. The high mobilities of the ions beyond the first interfacial layer from TiO₂ interface ($> 5 \text{ \AA}$) should be related to the enhancement of ionic conductivity of the SPEs/TiO₂ nanocomposites.

Finally, the structures, dynamics and crystallization of PE nanocomposites composed of *n*-tetracontane (C₄₀H₈₂) mixed with a neutral, attraction and repulsion flat interface nanofiller were investigated by MC method of coarse-grained polymer model on a high coordination lattice. The chain structures and dynamics changed with the polymer-interface interaction. The attractive interaction between PE chains and the attractive wall causes PE density to locate more at the interface than in the bulk region which leads to the fastest chain relaxation compared to other filler types. For the repulsive interface system, the situation was reversed. For crystallization studies,

the temperature was instantaneously dropped from 473 K to 298 K, and the simulation was continued at 298 K. As the simulation proceeds at 298 K, the chains adopt more *trans* conformation. After 10 million MCS, the fraction of the bonds in the *trans* states approaches a limiting value about 73-83% which is smaller than that of the crystallization in the bulk (*ca.* 85%). Therefore, chains adopt more *gauche* conformation for the crystallization in the nanocomposites. The attractive interface causes chain to adopt more *gauche* conformation compared to the repulsive and neutral surfaces.

CHAPTER VII

SUMMARY

In this thesis, computational molecular modeling methods including Molecular Dynamics (MD) for atomistic calculation and Monte Carlo (MC) for mesoscale calculation were employed to study solid polymer electrolytes (SPEs) of the type PEO-KI added TiO₂ nanofiller used in dye-sensitized solar cells (DSSCs). For MD simulations, Materials Studio 4.2 simulation package provided by National Nanotechnology Center of Thailand was used. For MC simulations, in-house software initially developed by Visit Vaosoongnern (Chemistry, Suranaree University of Technology) from the past collaboration with the Department of Polymer Science, University of Akron, USA during 2000-2004 was used.

Firstly, MD simulations with COMPASS forcefield were employed to determine the solvation structures and to predict EXAFS spectra of K⁺ and I⁻ ions in water, as well as K⁺ ion in tetraglyme as model complexes for SPEs used in DSSCs. The structural properties *i.e.* pair distances and coordination numbers obtained from our MD simulations are in very good agreement with other works. Moreover, the simulated EXAFS spectra are consistent with the measured EXAFS spectra for both *k*-space and *R*-space. This indicates that MD method with COMPASS forcefield is a very useful technique to study the local solvation structures of ionic aqueous solution and model compound representing PEO-KI based electrolytes.

Next, MD method with COMPASS forcefield was performed on the tetraglyme:KI systems with an ether oxygen:K⁺ mole ratio of 10:1 to study the effect of adding KI salt on the properties of tetraglyme (a 4-mers model compound for PEO). For tetraglyme:KI complex, the dihedral distribution functions show that *gauche* conformations along both C–C and C–O bonds are increased whereas *trans* conformation is vanished. The radius of gyration demonstrates that adding KI salt causes the polymer chains become more compact. Integrating the K⁺–O and K⁺–I RDFs over the first coordination shells gives an average 2.4 oxygens and 3.1 iodide anions coordinated to each K⁺, indicating that there is a competition in complexation of K⁺ between ether oxygens and iodide anions, and that the degree of coordination of K⁺ by iodide anions is comparable to that by ether oxygens. The diffusion coefficient (D), which can be calculated from the slope of the mean square displacement, of K⁺ cations is slightly lower than that of I⁻ anions which may result from an additional coordination of K⁺ by ether oxygens. Therefore, it can be concluded that the interaction between K⁺ cations and ether oxygens causes some changes in the structural, conformational, and dimensional properties of tetraglyme chains which may infer to a reduction of the crystallinity and an enhancement of the ionic conductivity of longer PEO chain system as mentioned in available experimental results.

Finally, MD simulations with COMPASS forcefield were performed on the PEO/TiO₂ and the more complicated PEO/KI/TiO₂ nanocomposite systems in order to understand the influence of TiO₂ interface and free surface on the structural and dynamical properties of PEO-KI based polymer electrolytes. MD simulations revealed that PEO density is significantly perturbed by TiO₂ interface and free surface, forming

layers of highly dense polymer (compared to the bulk melt) that persisted up to 15 Å from the TiO₂ interface. At the free surface region, PEO density is lower and the interfacial profile is about the polymer size (*ca.* 10 Å). The calculation of interaction energy indicates that there is an attractive interaction between TiO₂ interface and PEO. The interaction between PEO and TiO₂ causes not only a high of PEO density but also a slow down of chain dynamics at the interface region. This perturbation by TiO₂ may suppress the crystallinity of PEO and enhance the ionic conductivity of PEO-based nanocomposite electrolytes as mentioned in many available experimental results. Moreover, MD simulations were applied to study the effect of TiO₂ interface on the structural and dynamical properties of PEO/KI electrolyte system. MD results revealed that the density profile and the dynamics of PEO backbone atoms are similar to the system without added salt. The slow PEO mobility of the highly dense PEO layer near the TiO₂ interface tends to expel most of the ions to the regions away from the TiO₂ interface, causing the relative increase in ionic concentration away from the TiO₂ interface. Moreover, this affects on the remarkably slow mobilities of both K⁺ and I⁻ ions near the TiO₂ interface, whereas the mobilities for the ions away from TiO₂ interface are clearly faster than those of the system without nanofiller. The high mobilities of the ions beyond the first interfacial layer from TiO₂ interface (> 5 Å) may cause the enhancement of the ionic conductivity of the SPEs/TiO₂ nanocomposites.

In addition, the structures and dynamics of polymer nanocomposites at the longer time and length scale which is beyond the capacity of the current atomistic MD simulation method used in this work were investigated by MC simulations. The structures, dynamics and crystallization of PE nanocomposites composed of *n*-

tetracontane ($C_{40}H_{82}$) mixed with a neutral, attraction and repulsion flat interface nanofiller were determined by MC method of coarse-grained polymer model on a high coordination lattice. MC results revealed that the chain structures and dynamics changed with the polymer-interface interaction. The attractive interaction between PE chains and the attractive wall causes PE density to locate more at the interface than in the bulk region which leads to the fastest chain relaxation compared to other filler types. For the repulsive interface system, the situation was reversed. For crystallization studies, the temperature was instantaneously dropped from 473 K to 298 K and the simulation was continued at 298 K. As the simulation proceeds at 298 K, the chains adopt more *trans* conformation. After 10 million MCS, the fraction of the bonds in the *trans* states approaches a limiting value about 73-83% which is smaller than that of the crystallization in the bulk (*ca.* 85%). Therefore, chains adopt more *gauche* conformation for the crystallization in the nanocomposites. The attractive interface causes chain to adopt more *gauche* conformation compared to the repulsive and neutral surfaces.

REFERENCES

REFERENCES

- Abe, A., Jernigan, R. L., and Flory, P. J. (1966). Conformational energies of *n*-alkanes and the random configuration of higher homologs including polymethylene. **J. Am. Chem. Soc.** 88: 631.
- Akhtar, M. S., Chun, J-M., and Yang, O-B. (2007). Advanced composite gel electrolytes prepared with titania nanotube fillers in polyethylene glycol for the solid-state dye-sensitized solar cell. **Electrochemistry Commun.** 9: 2833.
- Albinsson, I., Mellander, B-E., and Stevens, J. R. (1991). Ionic conductivity in poly(ethylene oxide) modified poly(dimethylsiloxane) complexed with lithium salts. **Polymer** 32: 2712.
- Allen, M. P., and Tildesley, D. J. (1989). **Computer simulation of liquids.** Oxford University Press.
- Allen, M. P. (2004). **Introduction to molecular dynamics simulation** [On-line]. Available: <http://www.fz-juelich.de/nic-series/volume23/allen.pdf>
- Appetecchi, G. B., Dautzenberg, G., *et al.* (1998). **J. Electrochem. Soc.** 145: 4126.
- Appetecchi, G. B., Mastragostino, M., *et al.* (1998). **J. Electrochem. Soc.** 145: 4133.
- Armand, M. B., Chabagno, J. M., and Duclot, M. J. (1978). In **Extended Abstract of the Second International Meeting on Solid Electrolytes.** Scotland: St. Andrews University Press.

- Armand, M. B., Chabagno, J. M., and Duclot, M. J. (1979). In Vashishta, P., Mundy, J. N., and Shenoy, G. K. (eds.). **Fast Ion Transport in Solids** (p 131). Amsterdam, New York: North-Holland.
- Ayala, R., Martínez, J. M., Pappalardo, R. R., and Marcos, E. S. (2003). On the halide hydration study: Development of first-principles halide ion-water interaction potential based on a polarizable model. **J. Chem. Phys.** 119: 9538.
- Bach, U., *et al.* (1998). Solid-state dye-sensitized mesoporous TiO₂ solar cells with high photon-to-electron conversion efficiencies. **Nature** 395: 583.
- Balijepalli, S., and Rutledge, G. C. (1998). Molecular simulation of the intercrystalline phase of chain molecules. **J. Chem. Phys.** 109: 6523.
- Baschnagel, J., and Binder, K. (1995). On the influence of hard walls on structural properties in polymer glass simulation. **Macromolecules** 28: 6808.
- Baschnagel, J., Paul, W., Tries, V., and Binder, K. (1998). Statics and dynamics of bidisperse polymer melts: A Monte Carlo study of the bond-fluctuation model. **Macromolecules** 31: 3856.
- Berthier, C., *et al.* (1983). Microscopic investigation of ionic conductivity in alkali metal salts-poly(ethylene oxide) adducts. **Solid State Ionics** 11: 91.
- Bishop, A. G., MacFarlane, D. R., McNaughton, D., and Forsyth, M. (1996). FT-IR investigation of ion association in plasticized solid polymer electrolytes. **J. Phys. Chem.** 100: 2237.
- Bitsanis, I., and Hadziioaou, G. (1990). Molecular dynamics simulations of the structure and dynamics of confined polymer melts. **J. Chem. Phys.** 92: 3827.

- Borodin, O., and Smith, G. D. (1998). Molecular dynamics simulations of poly(ethylene oxide)/LiI melts. 1. Structural and conformational properties. **Macromolecules** 31: 8396.
- Borodin, O., and Smith, G. (2000). Molecular dynamics simulations of poly(ethylene oxide)/LiI melts. 2. Dynamic properties. **Macromolecules** 33: 2273.
- Borodin, O., Smith, G. D., Bandyopadhyaya, R., and Buytner, O. (2003). Molecular dynamics study of the influence of solid interfaces on poly(ethylene oxide) structure and dynamics. **Macromolecules** 36: 7873.
- Brodskaya, E., Lyubartsev, A. P., and Laaksonen, A. (2002). Molecular dynamics simulations of water clusters with ions at atmospheric conditions. **J. Chem. Phys.** 116: 7879.
- Bruce, P. G., and Vincent, C. A. (1993). Polymer electrolytes. **J. Chem. Soc., Faraday Trans.** 89: 3187.
- Cao, F., Oskam, G., and Searson, P.C. (1995). A solid state, dye sensitized photoelectrochemical cell. **J. Phys. Chem.** 99: 17071.
- Capiglia, C., Mustarelli, P., Quartarone, E., Tomasi, C., and Magistris, A. (1999). Effects of nanoscale SiO₂ on the thermal and transport properties of solvent-free, poly(ethylene oxide) (PEO)-based polymer electrolytes. **Solid State Ionics** 118: 73.
- Catlow, C. R. A., and Mills, G. E. (1995). Computer simulation of ionically conducting polymers. **Electrochim. Acta.** 40: 2057.
- Chapin, D. M., Fuller, C. S., and Pearson, G. L. (1954). A new silicon *p-n* junction photocell for converting solar radiation into electrical power. **J. Appl. Phys.** 25: 676.

- Chatzivasiloglou, E., *et al.* (2007). The influence of the metal cation and the filler on the performance of dye-sensitized solar cells using polymer-gel redox electrolytes. **J. Photochem. Photobiol. A: Chem.** 192: 49.
- Chen, H. W., Chiu, C. Y., Wu, H. D., Shen, I. W., and Chang, F. C. (2002). Solid state electrolyte nanocomposites based on poly(ethylene oxide), poly(oxypropylene) diamine, mineral clay and lithium perchlorate. **Polymer** 43: 5011.
- Chintapalli, S., and Frech, R. (1995). Ionic association and conductivity in poly(ethylene oxide) and poly(propylene oxide) metal salt systems. **Electrochim. Acta.** 40: 2093.
- Chintapalli, S. (1996). **Structural characterization of polymer – salt complexes and the role of plasticizers in ionic transport.** Ph. D. Dissertation, University of Oklahoma Graduate College, USA.
- Chintapalli, S., Frech, R., and Grady, B. (1997). An investigation of the high molecular weight poly(ethylene oxide)-zinc bromide complexes. **Polymer** 38: 6189.
- Chintapalli, S., Quinton, C., Frech, R., and Vincent, C. A. (1997). Compound formation and ionic association in the poly(ethylene oxide)-potassium triflate system. **Macromolecules** 30: 7472.
- Cho, J., and Mattice, W. L. (1997). Estimation of long-range interaction in coarse-grained rotational isomeric state polyethylene chains on a high coordination lattice. **Macromolecules** 30: 637.
- Colbourn, E. A. (1994). **Computer simulation of polymers.** Longman Scientific & Technical.

- Computational chemistry list. (1996). **Molecular Dynamics and Monte Carlo** [On-line]. Available: <http://www.ccl.net/cca/documents/molecular-modeling/node9.html>
- Croce, F., Appetecchi, G. B., Persi, L., and Scrosati, B. (1998). Nanocomposite polymer electrolytes for lithium batteries. **Nature** 394: 456.
- Croce, F., *et al.* (1999). Physical and chemical properties of nanocomposite polymer electrolytes. **J. Phys. Chem. B** 103: 10632.
- Curtiss, L. A., and Gordon, M. S. (eds.). (2004). **Computational materials chemistry: Methods and applications**. London: Kluwer.
- Dai, Y., Greenbaum, S., *et al.* (1998). Lithium-7 NMR studies of concentrated LiI/PEO-based solid electrolytes. **Solid State Ionics** 106: 25.
- Dai, Y., Wang, Y., *et al.* (1998). Electrical, thermal and NMR investigation of composite solid electrolytes based on PEO, LiI and high surface area inorganic oxides. **Electrochim. Acta**. 43: 1557.
- Deutsch, H. P., and Binder, K. (1991). Interdiffusion and self-diffusion in polymer mixtures: A Monte Carlo study. **J. Chem. Phys.** 94: 2294.
- Dominey, L. A. (1994). In Pistoia, G. (ed.). **Lithium batteries: New materials, developments and perspectives**. Amsterdam: Elsevier.
- Dong, H., Hyun, J-K., Rhodes, C. P., Frech, R., and Wheeler, R. A. (2002). Molecular dynamics simulations and vibrational spectroscopic studies of local structure in tetraglyme:sodium triflate ($\text{CH}_3\text{O}(\text{CH}_2\text{CH}_2\text{O})_4\text{CH}_3:\text{NaCF}_3\text{SO}_3$) solutions. **J. Phys. Chem. B** 106: 4878.

- Doruker, P., Rapold, R. F., and Mattice, W. L. (1996). Rotational isomeric state models for polyoxyethylene and polythiaethylene on a high coordination lattice. **J. Chem. Phys.** 104: 8742.
- Doruker, P., and Mattice, W. L. (1997). Reverse mapping of coarse-grained polyethylene chains from the second nearest neighbor diamond lattice to an atomistic model in continuous space. **Macromolecules** 30: 5520.
- Doruker, P., and Mattice, W. L. (1998). Simulation of polyethylene thin films on a high coordination lattice. **Macromolecules** 31: 1418.
- Doruker, P., and Mattice, W. L. (1999). Mobility of the surface and interior of thin films composed of amorphous polyethylene. **Macromolecules** 32: 194.
- Doruker, P., and Mattice, W. L. (1999). Segregation of chain ends is a weak contributor to increased mobility at free polymer surfaces. **J. Phys. Chem. B** 103: 178.
- Ennari, J., Neelov, I., and Sundholm, F. (2000). Molecular dynamics simulation of the structure of PEO based solid polymer electrolytes. **Polymer** 41: 4057.
- Faucher, J. A., *et al.* (1966). Glass transitions of ethylene oxide polymers. **J. Appl. Phys.** 37: 3962.
- Ferlat, G., *et al.* (2001). Hydration of the bromine ion in a supercritical 1:1 aqueous electrolyte. **Phys. Rev. B** 63: 134202.
- Ferlat, G., Soetens, J-C., Miguel, A. S., and Bopp, P. A. (2005). Combining extended X-ray absorption fine structure with numerical simulations for disordered systems. **J. Phys.: Condens. Matter** 17: S145.

- Fodi, B., and Hentschke, R. (1998). Molecular dynamics simulation of a binary hydrocarbon mixture near an adsorbing wall: Benzene/*n*-heptane on graphite. **Langmuir** 14: 429.
- Forsyth, M., *et al.* (2002). The effect of nano-particle TiO₂ fillers on structure and transport in polymer electrolytes. **Solid State Ionics** 147: 203.
- Fried, H., and Binder, K. (1991). The microphase separation transition in symmetric diblock copolymer melts: A Monte Carlo study. **J. Chem. Phys.** 94: 8349.
- Fulton, J. L., Hoffmann, M. M., Darab, J. G., Palmer, B. J., and Stern, E. A. (2000). Copper(I) and copper(II) coordination structure under hydrothermal conditions at 325 °C: An X-ray absorption fine structure and molecular dynamics study. **J. Phys. Chem. A** 104: 11651.
- Fulton, J. L., Heald, S. M., Badyal, Y. S., and Simonson, J. M. (2003). Understanding the effects of concentration on the solvation structure of Ca²⁺ in aqueous solution. I: The perspective on local structure from EXAFS and XANES. **J. Phys. Chem. A** 107: 4688.
- Gadjourova, Z., Andreev, Y. G., Tunstall, D. P., and Bruce, P. G. (2001). Ionic conductivity in crystalline polymer electrolytes. **Nature** 412: 520.
- Gebeyehu, D., Brabec, C. J., and Sariciftci, N. S. (2002). Solid-state organic/inorganic hybrid solar cells based on conjugated polymers and dye-sensitized TiO₂ electrodes. **Thin Solid Films** 403: 271.
- Gebeyehu, D., *et al.* (2002). Hybrid solar cells based on dye-sensitized nanoporous TiO₂ electrodes and conjugated polymers as hole transport materials. **Synth. Met.** 125: 279.

- Glezakou, V. A., Chen, Y., Fulton, J. L., Schenter, G. K., and Dang, L. X. (2006). Electronic structure, statistical mechanical simulations, and EXAFS spectroscopy of aqueous potassium. **Theor. Chem. Acc.** 115: 86.
- Grant, C. D., *et al.* (2002). Characterization of nanocrystalline and thin film TiO₂ solar cells with poly(3-undecyl-2,2'-bithiophene) as a sensitizer and hole conductor. **J. Electroanal. Chem.** 522: 40.
- Grätzel, M. (1999). Mesoporous oxide junctions and nanostructured solar cells. **Curr. Opin. Colloid Interface Sci.** 4: 314.
- Grätzel, M. (2000). Perspectives for dye-sensitized nanocrystalline solar cells. **Prog. Photovolt. Res. Appl.** 8: 171.
- Grätzel, M. (2001). Photoelectrochemical cells. **Nature** 414: 338.
- Grätzel, M. (n.d.). Measured under standard air mass 1.5 reporting conditions, PV calibration Laboratory of the National Energy Research Laboratory (NREL), Golden, CO, USA.
- Gray, F. M. (1991). **Solid polymer electrolytes: Fundamentals and technological applications.** New York: VCH.
- Gray, F. M. (1997). **Polymer electrolytes.** Cambridge, UK: The Royal Society of Chemistry.
- Hagen, J., *et al.* (1997). Novel hybrid solar cells consisting of inorganic nanoparticles and an organic hole transport material. **Synth. Met.** 89: 215.
- Hagfeldt, A., and Grätzel, M. (1995). Light-induced redox reactions in nanocrystalline systems. **Chem. Rev.** 95: 49.
- Haile, J. M. (1997). **Molecular dynamics simulation.** Wiley.

- Hara, K., *et al.* (2003). Molecular design of coumarin dyes for efficient dye-sensitized solar cells. **J. Phys. Chem. B** 107: 597.
- Hentschke, R., Schürmann, B. L., and Rabe, J. P. (1992). Molecular dynamics simulations of ordered alkane chains physisorbed on graphite. **J. Chem. Phys.** 96: 6213.
- Heuft, J. M., and Meijer, E. J. (2005). Density functional theory based molecular-dynamics study of aqueous iodide solvation. **J. Chem. Phys.** 123: 094506.
- Hinsch, A., *et al.* (2000). Long-term stability of dye sensitized solar cells for large area power applications (LOTS-DSC). In **Proceedings of 16th European Photovoltaic Solar Energy Conference and Exhibition**. Glasgow, Great Britain.
- Hoffmann, M. M., Darab, J. G., Palmer, B. J., and Fulton, J. L. (1999). A transition in the Ni²⁺ complex structure from six- to four-coordinate upon formation of ion pair species in supercritical water: An X-ray absorption fine structure, near-infrared, and molecular dynamics study. **J. Phys. Chem. A** 103: 8471.
- Hribar, B., Southall, N. T., Vlachy, V., and Dill, K. A. (2002). How ions affect the structure of water. **J. Am. Chem. Soc.** 124: 12302.
- Huang, W., Frech, R., Johansson, P., and Lindgren, J. (1995). Cation-polymer interaction and ionic association in diglyme-LiCF₃SO₃ and diglyme-propylene carbonate-LiCF₃SO₃ complexes. **Electrochim. Acta.** 40: 2147.
- Hug, R., Farrington, G. C., Koksang, R., and Tonder, P. E. (1992). Influence of plasticizers on the electrochemical and chemical stability of a Li⁺ polymer electrolyte. **Solid State Ionics** 57: 277.

- Hyun, J.-K., Dong, H., Rhodes, C. P., Frech, R., and Wheeler, R. A. (2001). Molecular dynamics simulations and spectroscopic studies of amorphous tetraglyme ($\text{CH}_3\text{O}(\text{CH}_2\text{CH}_2\text{O})_4\text{CH}_3$) and tetraglyme: LiCF_3SO_3 structures. **J. Phys. Chem. B** 105: 3329.
- Ignaczak, A., Gomes, J. A. N. F., and Cordeiro, M. N. D. S. (1999). Quantum and simulation studies of $\text{X}^-(\text{H}_2\text{O})_n$ systems. **Electrochim. Acta.** 45: 659.
- Intarakamhang, S. (2005). **Preparation, characterization and molecular modeling of poly(ethylene oxide)/poly(vinyl pyrrolidone) montmorillonite nanocomposite solid electrolytes.** M. Sc. Dissertation, Suranaree University of Technology, Thailand.
- Iverson, M. T., B. L. D. (1962). In Davidson, R. L., and Sittig, M. (eds.). **Water soluble resins.** New York: Van Nostrand Reinhold.
- Jaffe, R. L., Smith, G. D., and Yoon, D. Y. (1993). Conformations of 1,2-dimethoxyethane from *ab initio* electronic-structure calculations. **J. Phys. Chem.** 97: 12745.
- Kalaignan, G. P., Kang, M. S., and Kang, Y. S. (2006). Effects of compositions on properties of PEO–KI–I₂ salts polymer electrolytes for DSSC. **Solid State Ionics** 177: 1091.
- Kasemägi, H., Klintonberg, M., Aabloo, A., and Thomas, J. O. (2002). Molecular dynamics simulation of the LiBF_4 –PEO system containing Al_2O_3 nanoparticles. **Solid State Ionics** 147: 367.
- Khare, R., de Pablo, J. J., and Yethiraj, A. (1996). Rheology of confined polymer melts. **Macromolecules** 29: 7910.

- Kim, J. H., Min, B. R., Lee, K. B., Won, J., and Kang, Y. S. (2002). Coordination structure of various ligands in crosslinked PVA to silver ions for facilitated olefin transport. **Chem. Commun.** 2732.
- Koneshan, S., Rasaiah, J. C., Lynden-Bell, R. M., and Lee, S. H. (1998). Solvent structure, dynamics, and ion mobility in aqueous solutions at 25 °C. **J. Phys. Chem. B** 102: 4193.
- Krishnan, M., and Balasubramanian, S. (2004). Order-disorder transitions and melting in a helical polymer crystal: Molecular dynamics calculations of model poly(ethylene oxide). **Chem. Phys. Lett.** 385: 351.
- Kubo, W., *et al.* (2001). Quasi-solid-state dye-sensitized TiO₂ solar cells: effective charge transport in mesoporous space filled with gel electrolytes containing iodide and iodine. **J. Phys. Chem. B** 105: 12809.
- Kubo, W., Kitamura, T., Hanabusa, K., Wada, Y., and Yanagida, S. (2002). Quasi-solid-state dye-sensitized solar cells using room temperature molten salts and a low molecular weight gelator. **Chem. Commun.** 374.
- Kumar, S. K., Vacatello, M., and Yoon, D. Y. (1990). Off-lattice Monte Carlo simulations of polymer melts confined between two plates. **2.** Effects of chain length and plate separation. **Macromolecules** 23: 2189.
- Kumar, B., and Scanlon, L. G. (1999). Polymer-ceramic composite electrolytes: conductivity and thermal history effects. **Solid State Ionics** 124: 239.
- Kumar, B., Scanlon, L. G., and Spry, R. J. (2001). On the origin of conductivity enhancement in polymer-ceramic composite electrolytes. **J. Power Sources** 96: 337.

- Lai, P-Y. (1995). Statics and dynamics of adsorbed polymer chains: A Monte Carlo simulation. **J. Chem. Phys.** 103: 5742.
- Lee, S. H., and Rasaiah, J. C. (1996). Molecular dynamics simulation of ion mobility. 2. Alkali metal and halide ions using the SPC/E model for water at 25 °C. **J. Phys. Chem.** 100: 1420.
- Lennard-Jones, J. E. (1931). Cohesion. **Proceeding of the Physical Society.** 43: 461.
- Li, J., and Khan, M. (1993). Highly conductive solid polymer electrolytes prepared by blending high molecular weight poly(ethylene oxide), poly(2- or 4-vinylpyridine), and lithium perchlorate. **Macromolecules** 26: 4544.
- Li, B., Wang, L., Kang, B., Wang, P., and Qiu, Y. (2006). Review of recent progress in solid-state dye-sensitized solar cells. **Sol. Energy Mater. Sol. Cells** 90: 549.
- Licht, S. (1995). Electrolyte modified photoelectrochemical solar cells. **Sol. Energy Mater. Sol. Cells** 38: 305.
- Lin, B., Boinske, P. T., and Halley, J. W. (1996). A molecular dynamics model of the amorphous regions of polyethylene oxide. **J. Chem. Phys.** 105: 1668.
- Lin, C. W., *et al.* (2005). Influence of TiO₂ nano-particles on the transport properties of composite polymer electrolyte for lithium-ion batteries. **J. of Power Sources** 146: 397.
- Liu, Y., Lee, J. Y., and Hong, L. (2003). Morphology, crystallinity, and electrochemical properties of *in situ* formed poly(ethylene oxide)/TiO₂ nanocomposite polymer electrolytes. **J. Appl. Polym. Sci.** 89: 2815.
- Londono, *et al.* (1997). Cation environment in molten lithium iodide doped poly(ethylene oxide). **Macromolecules** 30: 7151.

- Longo, C., Nogueira, A. F., De Paoli, M. A., and Cachet, H. (2002). Solid-state and flexible dye-sensitized TiO₂ solar cells: a study by electrochemical impedance spectroscopy. **J. Phys. Chem. B** 106: 5925.
- MacCallum, J. R., and Vincent, C. A. (eds.). (1987). **Polymer electrolyte reviews** (Vol. 1). London: Elsevier.
- MacCallum, J. R., and Vincent, C. A. (eds.). (1989). **Polymer electrolyte reviews** (Vol. 2). London: Elsevier.
- Madden, W. G. (1987). Monte Carlo studies of the melt–vacuum interface of a lattice polymer. **J. Chem. Phys.** 87: 1405.
- Mansfield, K. F., and Theodorou, D. N. (1989). Interfacial structure and dynamics of macromolecular liquids: A Monte Carlo simulation approach. **Macromolecules** 22: 3143.
- Mansfield, K. F., and Theodorou, D. N. (1990). Atomistic simulation of a glassy polymer surface. **Macromolecules** 23: 4430.
- Mao, G., Perea, R. F., Howells, W. S., Price, D. L., and Sabounji, M. L. (2000). Relaxation in polymer electrolytes on the nanosecond timescale. **Nature** 405: 163.
- Maple, J. R., Thacher, T. S., Dinur, U., and Hagler, A. T. (1990). Biosym forcefield research results in new techniques for the extraction of inter- and intramolecular forces. **Chem. Des. Autom. News** 5: 5.
- Marcinek, M., *et al.* (2000). Effect of filler surface group on ionic interactions in PEG-LiClO₄-Al₂O₃ composite polyether electrolytes. **J. Phys. Chem. B** 104: 11088.
- Marcus, Y. (1988). Ionic radii in aqueous solutions. **Chem Rev** 88: 1475.

- Mathiowetz, A. M. (1994). **Introduction** [On-line]. Available: http://www.wag.caltech.edu/publications/theses/alan/section1_6_0_1.html
- Mattice, W. L., and Suter, U. W. (1994). **Conformational theory of large molecules: The rotational isomeric state model in macromolecular systems**. New York: Wiley.
- McCarthy, M. I., Schenter, G. K., Chacon-Taylor, M. R., Rehr, J. J., and Brown, G. E. (1997). Prediction of extended X-ray-absorption fine-structure spectra from molecular interaction models: $\text{Na}^+(\text{H}_2\text{O})_n\text{-MgO}$ (100) interface. **Phys. Rev. B** 56: 9925.
- Merkling, P. J., Ayala, R., Martínez, J. M., Pappalardo, R. R., and Marcos, E. S. (2003). Interplay of computer simulations and X-ray absorption spectra in the study of the bromide hydration structure **J. Chem. Phys.** 119: 6647.
- Metropolis, N, Rosenbluth, A. W., Rosenbluth, M. N., Teller, A. H., and Teller, E. (1953). Equation of state calculations by fast computing machines. **J. Chem. Phys.** 21: 1087.
- Minoura Laboratory. (2008). **Electrochemical self-assembly of semiconductor/dye hybrid thin films and their application to dye-sensitized solar cells** [On-line]. Available: http://apchem.gifu-u.ac.jp/~pcl/minourahp/research/research_e.htm#esa
- Morgan, G. T., and Drew, H. D. K. (1920). Researches on residual affinity and coordination. Part II. Acetylacetones of selenium and tellurium. **J. chem. Soc. Trans.** 117: 1456.

- Muhuri, P. K., Das, B., and Hazra, D. K. (1997). Ionic association of some lithium salts in 1,2-dimethoxyethane. A Raman spectroscopic and conductivity study. **J. Phys. Chem. B** 101: 3329.
- Muller-Plathe, F., and van Gunsteren, W. F. (1995). **J. Chem. Phys.** 103: 4745.
- Mustarelli, P., *et al.* (1999). Cation dynamics and relaxation in nanoscale polymer electrolytes: A ^7Li NMR study. **Phys. Rev. B** 60: 7228.
- Nazeeruddin, M. K., *et al.* (1993). Conversion of light to electricity by cis- $\text{X}_2\text{bis}(2,2'$ -bipyridyl-4,4'-dicarboxylate)ruthenium(II) charge-transfer sensitizers ($\text{X} = \text{Cl}^-$, Br^- , I^- , CN^- , and SCN^-) on nanocrystalline TiO_2 electrodes. **J. Am. Chem. Soc.** 115: 6382.
- Neyertz, S., Brown, D., and Thomas, J. O. (1995). Molecular dynamics simulation of the crystalline phase of poly(ethylene oxide)-sodium iodide, PEO_3NaI . **Electrochim. Acta.** 40: 2063.
- Neyertz, S., and Brown, D. (1995). **J. Chem. Phys.** 102: 9275.
- Neyertz, S., and Brown, D. (1996). **J. Chem. Phys.** 104: 3797.
- Nogueira, A. F., Durrant, J. R., and De Paoli, M. A. (2001). Dye-sensitized nanocrystalline solar cells employing a polymer electrolyte. **Adv. Mater.** 13: 826.
- Nogueira, A. F., Longo, C., and De Paoli, M. A. (2004). Polymers in dye sensitized solar cells: overview and perspectives. **Coord. Chem. Rev.** 248: 1455.
- Okamoto, Y. (2004). XAFS simulation of highly disordered materials. **Nucl. Instrum. Methods Phys. Res. A** 526: 572.
- Oregan, B., and Grätzel, M. (1991). A low-cost, high-efficiency solar cell based on dye-sensitized colloidal TiO_2 films. **Nature** 353: 737.

- Ozisik, R., Doruker, P., Mattice, W. L., and von Meerwall, E. D. (2000). Translational diffusion in Monte Carlo simulations of polymer melts: Center of mass displacement vs. integrated velocity autocorrelation function. **Comput. Theor. Polymer Sci.** 10: 411.
- Palmer, B. J., Pfund, D. M., and Fulton, J. L. (1996). Direct modeling of EXAFS spectra from molecular dynamics simulations. **J. Phys. Chem.** 100: 13393.
- Pant, P. V. K., and Theodorou, D. N. (1995). Variable connectivity method for the atomistic Monte Carlo simulation of polydisperse polymer melts. **Macromolecules** 28: 7224.
- Paul, W., Binder, K., Kremer, K., and Heerman, D. W. (1991). Structure-property correlation of polymers, a Monte Carlo approach. **Macromolecules** 24: 6332.
- Paulsson, H., Hagfeldt, A., and Kloo, L. (2003). Molten and solid trialkylsulfonium iodides and their polyiodides as electrolytes in dye-sensitized nanocrystalline solar cells. **J. Phys. Chem. B** 107: 13665.
- Payne, V. A., *et al.* (1995). Ion clustering in molecular dynamics simulations of sodium iodide solutions. **Electrochim. Acta.** 40: 2087.
- Przyluski, J., and Wieczorek, W. (1992). Copolymer electrolytes. **Solid State Ionics** 53-56: 1071.
- Rapaport, D. C. (1995). **The art of molecular dynamics simulation.** Cambridge University Press.
- Rapold, R. F., and Mattice, W. L. (1995). New high-coordination lattice model for rotational isomeric state polymer chains. **J. Chem. Soc. Faraday Trans.** 91: 2435.

- Rapold, R. F., and Mattice, W. L. (1996). Introduction of short and long range energies to simulate real chains on the *2nnd* lattice. **Macromolecules** 29: 2457.
- Rehr, J. J., and Albers, R. C. (1990). Scattering-matrix formulation of curved-wave multiple-scattering theory: Application to X-ray-absorption fine structure. **Phys. Rev. B** 41: 8139.
- Rehr, J. J., de Leon, J. M., Zabinsky, S. I., and Albers, R. C. (1991). Theoretical X-ray absorption fine structure standards. **J. Am. Chem. Soc.** 113: 5135.
- Rehr, J. J., Albers, R. C., and Zabinsky, S. I. (1992). High-order multiple-scattering calculations of X-ray-absorption fine structure. **Phys. Rev. Lett.** 69: 3397.
- Rempe, S. B., Asthagiri, D., and Pratt, L. R. (2004). Inner shell definition and absolute hydration free energy of $K^+(aq)$ on the basis of quasi-chemical theory and *ab initio* molecular dynamics. **Phys. Chem. Chem. Phys.** 6: 1966.
- Ribarsky, M. W., and Landman, U. (1992). Structure and dynamics of *n*-alkanes confined by solid surfaces. I. Stationary crystalline boundaries. **J. Chem. Phys.** 97: 1937.
- Ruiz, E., and Aranda, P. (2000). **Electroactive polymers intercalated in clay and related solids: Polymer-clay nanocomposites**. John Wiley & Sons.
- Sanchez, I. C. (ed.). (1992). **Physics of polymer surfaces and interfaces**. Boston: Butterworth Heinemann.
- Scrosati, B., Croce, F., and Persi, L. (2000). **J. Electrochem. Soc.** 147: 1718.
- Sinke, W. C., and Wienk, M. M. (1998). Photochemistry: Solid-state organic solar cells. **Nature** 395: 544.

- Smith, G. D., Jaffe, R. L., and Yoon, D. Y. (1993). A force-field for simulations of 1,2-dimethoxyethane and poly(oxyethylene) based upon *ab initio* electronic structure calculations on model molecules. **J. Phys. Chem.** 97: 12752.
- Smith, G. D., *et al.* (1996). Conformations and structures of poly(oxyethylene) melts from molecular dynamics simulations and small-angle neutron scattering experiments. **Macromolecules** 29: 3462.
- Smith, G. D., Bedrov, D., Li, L., and Bytner, O. (2002). A molecular dynamics simulation study of the viscoelastic properties of polymer nanocomposites. **J. Chem. Phys.** 117: 9478.
- Sorkin, V. (2003). **Local density profile** [On-line]. Available: <http://phycomp.technion.ac.il/~phsorkin/thesis/node34.html>
- Spångberg, D., *et al.* (2000). Model extended X-ray absorption fine structure (EXAFS) spectra from molecular dynamics data for Ca²⁺ and Al³⁺ aqueous solutions. **J. Phys. Chem. B** 104: 10467.
- Starr, F. W., Schröder, T. B., and Glotzer, S. C. (2002). Molecular dynamics simulation of a polymer melt with a nanoscopic particle. **Macromolecules** 35: 4481.
- Stathatos, E., Lianos, P., Lavrencic-Stangar, U., and Orel, B. (2002). A high-performance solid-state dye-sensitized photoelectrochemical cell employing a nanocomposite gel electrolyte made by the sol-gel route. **Adv. Mater.** 14: 354.
- Stathatos, E., Lianos, R., Zakeeruddin, S. M., Liska, P., and Grätzel, M. (2003). A quasi-solid-state dye-sensitized solar cell based on a sol-gel nanocomposite electrolyte containing ionic liquid. **Chem. Mat.** 15: 1825.

- Stephan, A. M. (2006). Review on gel polymer electrolytes for lithium batteries. **European Polymer J.** 42: 21.
- Stergiopoulos, T., Arabatzis, I. M., Katsaros, G., and Falaras, P. (2002). Binary polyethylene oxide/titania solid-state redox electrolyte for highly efficient nanocrystalline TiO₂ photoelectrochemical cells. **Nano Lett.** 2: 1259.
- Sun, H. (1998). COMPASS: an *ab initio* force-field optimized for condensed-phase applications—overview with details on alkane and benzene compounds. **J. Phys. Chem. B** 102: 7338.
- Takahashi, Y., and Tadokoro, H. (1973). Structural studies of polyethers, $-(\text{CH}_2)_m\text{O}-$. X. Crystal structure of poly(ethylene oxide). **Macromolecules** 6: 672.
- Tóth, G. (1996). *Ab initio* pair potential parameter set for the interaction of a rigid and a flexible water model and the complete series of the halides and alkali cations. **J. Chem. Phys.** 105: 5518.
- Vao-soongnern, V., Doruker, P., and Mattice, W. L. (2000). Simulation of an amorphous polyethylene nanofiber on a high coordination lattice. **Macromol. Theory Simul.** 9: 1.
- Verdier, P. H., and Stockmayer, W. H. (1962). Monte Carlo calculations on the dynamics of polymers in dilute solution. **J. Chem. Phys.** 36: 227.
- Vincent, C. A. (1995). Ion transport in polymer electrolytes. **Electrochim. Acta.** 40: 2035.
- Wallen, S. L., *et al.* (1997). Hydration of bromide ion in supercritical water: An X-ray absorption fine structure and molecular dynamics study. **J. Phys. Chem. A** 101: 9632.

- Wang, P., Zakeeruddin, S. M., Exnar, I., and Grätzel, M. (2002). High efficiency dye-sensitized nanocrystalline solar cells based on ionic liquid polymer gel electrolyte. **Chem. Commun.** 2972.
- Werner, A., Müller, M., Schmid, F., and Binder, K. (1999). Effect of long-range forces on the interfacial profiles in thin binary polymer films. **J. Chem. Phys.** 110: 1221.
- Weston, J. E., and Steele, B. C. H. (1982). Effects of inert fillers on the mechanical and electrochemical properties of lithium salt-poly(ethylene oxide) polymer electrolytes. **Solid State Ionics** 7: 75.
- Wieczorek, W., Raducha, D., Zalewska, A., and Stevens, J. R. (1998). Effect of salt concentration on the conductivity of PEO-based composite polymeric electrolytes. **J. Phys. Chem. B** 102: 8725.
- Wikipedia. (2008). **Molecular Dynamics** [On-line]. Available: http://en.wikipedia.org/wiki/Molecular_dynamics
- Williamson, M. J., Southall, J. P., Hubbard, H. V. St. A., Davies, G. R., and Ward, I. M. (1999). Pulsed field gradient n.m.r. diffusion measurements on electrolyte solutions containing LiCF₃SO₃. **Polymer** 40: 3945.
- Wilson, E. B., Decius, J. C., and Cross, P. C. (1980). **Molecular Vibrations**. Dover, New York.
- Winkler, R. G., Schmid, R. H., Gerstmair, A., and Reineker, P. (1996). Molecular dynamics simulation study of the dynamics of fluids in thin films. **J. Chem. Phys.** 104: 8103.

- Wright, P. V. (1975). **Br. Polymer J.** 7: 319. Quoted in Puatrakul, T. (2000). **Studies of ionic conductivity of uniaxially stretched polymer electrolytes films**. Ph. D. Thesis, University of Arkron, USA.
- Zabinsky, S. I., Rehr, J. J., Ankudinov, A., Albers, R. C., and Eller, M. J. (1995). Multiple-scattering calculations of X-ray-absorption spectra. **Phys. Rev. B** 52: 2995.
- Zhan, Y., and Mattice, W. L. (1994). Molecular Dynamics simulation of the collapse of poly(1,4-*trans*-butadiene) to a globule and to a thin film. **Macromolecules** 27: 7056.

APPENDICES

การจำลองโมเลกุลาร์ไดนามิกส์อิเล็กโทรไลต์ระบบพอลิเอทิลีนออกไซด์:โพแทสเซียมไอโอไดด์
MOLECULAR DYNAMICS SIMULATION OF POLYETHYLENE
OXIDE:POTASSIUM IODIDE ELECTROLYTES

พรทิพย์ สีมา^{1,2}, ศุภกร รักใหม่^{3,4}, วันทนา คล้ายสุบรรณ⁴, วิศิษฐ์ แววสูงเนิน^{1,2*}
Porntip Seema^{1,2}, Supagorn Rugmai^{3,4}, Wantana Klysubun⁴, Visit Vao-soongnern^{1,2*}

Laboratory of Computational and Applied Polymer Science (LCAPS)¹, School of Chemistry² and School of Physics³, Institute of Science, Suranaree University of Technology, National Synchrotron Research Center⁴, Nakhon Ratchasima, Thailand.
E-mail: visit@sut.ac.th, Fax: 04-4224-185

บทคัดย่อ: ได้นำเทคนิคโมเลกุลาร์ไดนามิกส์มาใช้เพื่อศึกษาระบบ tetraglyme แทน PEO และระบบเติมเกลือ KI ในอัตราส่วน O:K = 10:1 ที่อุณหภูมิ 400 K จากนั้นวิเคราะห์โครงสร้างของพอลิเมอร์และการจับกันกับไอออนเกลือพบว่ารัศมีโคออร์ดิเนชันมีค่าน้อยลงในระบบที่มีเกลือ โดยในตอนแรกพันธะ C-O และ C-C จะชอบเกิดเป็นโครงสร้างแบบ *trans* และ *gauche* ก่อนการเติมเกลือ จากนั้นการกระจายของมุมบิดที่พันธะทั้งสองจะพบเป็นแบบ *trans* น้อยลงซึ่งเกิดจากการจับกันระหว่าง O และ K⁺ สัมประสิทธิ์การแพร่สำหรับ K⁺ และ I⁻ หาได้จากระยะเคลื่อนที่ยกกำลังสองเฉลี่ยซึ่งพบว่า K⁺ แพร่ใน PEO ได้ช้ากว่า I⁻ เล็กน้อย

Abstract: Molecular Dynamics (MD) simulations of pure tetraglyme, a model for amorphous PEO, and tetraglyme:potassium iodide (KI) complexes with an ether oxygen:K⁺ ratio of 10:1 were performed at 400 K. Structural analyses were done to investigate PEO conformations, I⁻ and oxygens coordination by K⁺. The mean-square radius of gyration shows that PEO chains become more compact upon complexation with salt. Dihedral angle population density distributions for PEO chains show that the *trans* conformation is favored for C-O bonds while the more compact *gauche* conformation is favored for C-C bonds. Both bonds prefer less *trans* conformation enforced by coordination of adjacent oxygens to K⁺. Diffusion coefficient for both K⁺ and I⁻ were estimated from the mean square displacement. K⁺ was found to diffuse slightly slower than I⁻ in PEO.

Introduction: Solid polymer electrolytes (SPEs), usually comprised of alkali salts dissolved in a polymer matrix, are subjected to intense study because they are vital components of modern electronic devices, including high energy-density batteries, fuel cells, and electrochromic displays. Poly(ethylene oxide) or "PEO" is one of the most widely studied host polymer matrix. It is now well-known that ion transport occurs primarily through amorphous regions of PEO:salt complexes. Understanding each of these aspects and their interrelations in amorphous PEO is necessary to

engineer PEO-based SPE with higher ionic conductivity. Computer simulations provide a direct way to analyze polymer conformations, polymer-ion interactions, and ionic association at the molecular level and have been applied to PEO:salts complexes. In this work, we illustrate an application of MD simulation to study the PEO:KI model with a 10:1 ether oxygen: K^+ ratio. The results will be later compared with experiment.

Methodology: MD simulations of pure tetraglyme (a 4-mers model compound for PEO) and tetraglyme:KI were performed using the Lucretius MD code. The simulated systems contained 50 tetraglyme chains (pure tetraglyme) and 50 tetraglyme chains plus 25 K^+ and 25 I^- ions. Initially, a box of 50 tetraglyme was equilibrated to obtain amorphous phases at 400 K. An initial crystalline configuration of 50 tetraglyme molecules was generated from the known crystal structure for PEO (7/2 helix). Periodic boundary conditions were applied and the equations of motion were integrated with a time step of 1 fs. NVT-MD was performed for 1 ns to attain the equilibrium. Next, 25 K^+ and I^- ions were randomly distributed in the box of equilibrated amorphous tetraglyme to create amorphous tetraglyme:KI at an ether oxygen: K^+ ratio of 10:1. Simulations were initially performed in the NPT ensemble for 1 ns at 400 K, and a new density of 1.04 g/cm³ was obtained. Further equilibrations of approximately 1 ns were performed in the NVT ensemble. Finally, atomic trajectories were collected for another 1 ns, for data analysis.

Results, Discussion, and Conclusion:

Chain conformation and dimension: In Figure 1(a), the influence of K^+ -O complexation on the distribution of torsional angles and chain dimension was examined. The *trans* conformation (*t*) of dihedral angles along the C-O bond of tetraglyme chains is predominant while the *gauche* conformation (g^+ and g^-) of dihedral angles along the C-C bond is favorable. For the K^+ -O complex system, the *gauche* conformation along both C-C and C-O bonds become larger resulting from the interaction of K^+ ion with the polymer oxygens. A decrease in *trans* population causes the structure become more compacted as seen in Figure 1(b) where the radius of gyration decreases upon K^+ -O complexation.

Radial distribution function: In Figure 2(a), radial distribution functions between K^+ and oxygen were calculated to investigate coordination of K^+ by polymer backbone. Integrating the K^+ -O radial distribution function over the first coordination shell (the first peak and minimum occurs at 2.65 and 4.05 Å, respectively) gives an average 2.4 oxygen atoms coordinated to each K^+ . In Figure 2(b), radial distribution function between K^+ and the I^- was plotted. The first peak (3.35 Å) and the first minima (4.45 Å) occur at the longer distance than that of K^+ -O in PEO. The coordination number is substantially larger. This result confirms that I^- is more competitive than oxygens in PEO in complexing with K^+ .

Mean-square displacement and diffusion coefficient: The diffusion coefficient (D) of K^+ and Γ in PEO was calculated from the MD slope of the mean-square displacement for long times, at these times normal (Einstein) diffusion is observed, and the mean-square displacement is a linear function of time: $D = \frac{1}{6} \lim_{t \rightarrow \infty} d \langle r(t) - r(0) \rangle^2 / dt$, the brackets denote an ensemble average. D for K^+ and Γ were found in the same order of magnitude of the reported values (5.0×10^{-7} and 7.5×10^{-7} cm^2/s , respectively). Interestingly, it was found that K^+ diffuses slightly slower than Γ . The possible explanations of this finding may be from an additional interaction of K^+ with polymer backbone.

Acknowledgements: This work is supported by National Synchrotron Research Center (2-2548/PS02).

References:

Hyun, J. K., Frech, R., and Wheeler, R.A. (2001). **J. Phys. Chem. B** 105: 3329-3337

Keywords: Poly(ethylene oxide) (PEO), Polymer electrolytes, Molecular Simulation

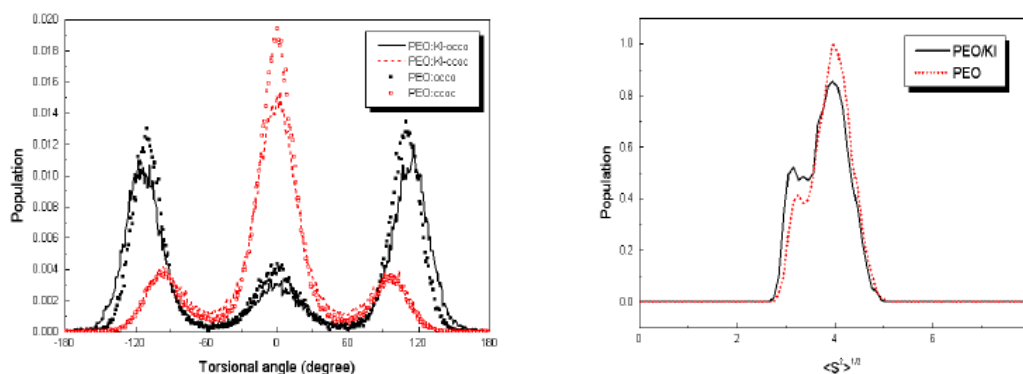


Figure 1 (a) Time-average population density distributions of tetraglyme backbone torsions around C-C and C-O bonds and (b) square radius of gyration in pure PEO and PEO/KI complex at 400 K.

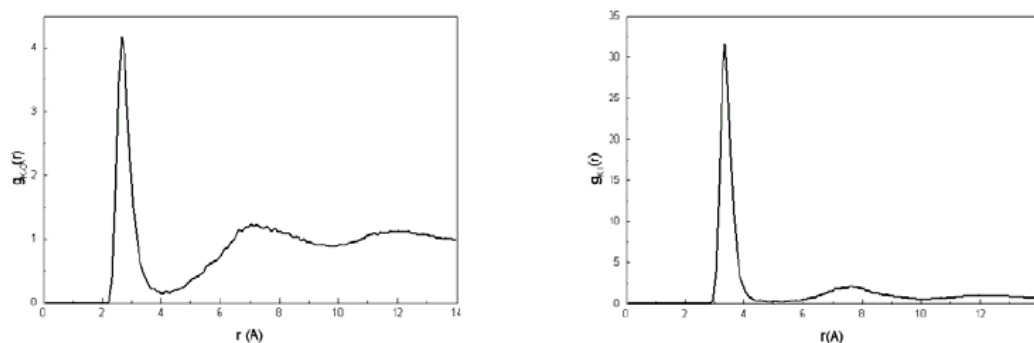


Figure 2 (a) Radial distribution function between K^+ and all oxygen atoms in a PEO:KI at 400 K. (b) Radial distribution functions between K^+ and I at 400 K.

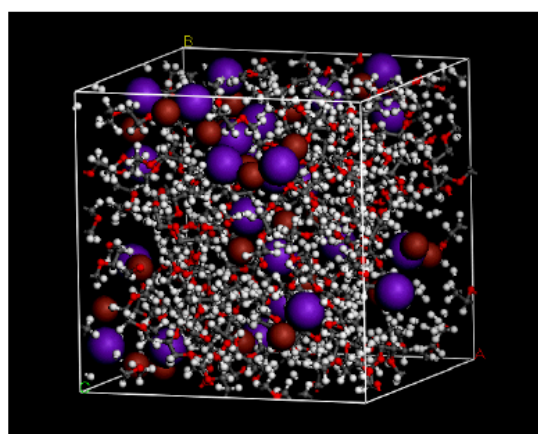


Figure 3 Atomistic model of PEO/KI structure (K: smaller ball, I: larger ball, stick: PEO).

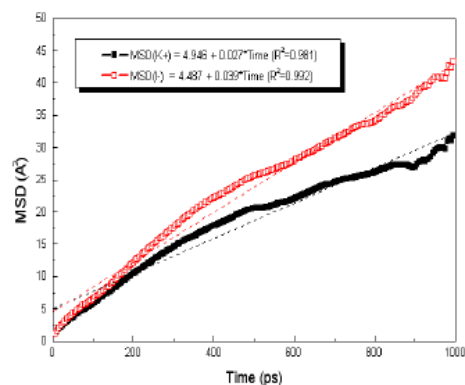


Figure 4 Mean square displacements of K^+ and I in PEO matrix.

MONTE CARLO SIMULATION OF STRUCTURE, DYNAMICS AND CRYSTALLIZATION OF POLYMER NANOCOMPOSITES

Porntip Seema, Visit Vao-soongnern*

* School of Chemistry, Institute of Science, Suranaree University of Technology, Nakhon Ratchasima, 30000. Email: visit@sut.ac.th

Abstract: The structure, dynamics and crystallization of linear monodisperse polyethylene (PE) melts containing homogeneously distributed spherical nanoparticles were investigated. The polymer chains were simulated using a coarse-grained model and a Monte Carlo algorithm. The influence of different interaction energy between monomers and particles (neutral, attractive and repulsive interaction) was investigated. The various chain structures changed slightly with the monomer-particle interaction. Crystallization was simulated by quenching the structure from the melt state to 298 K. Structure formation was investigated by the occupancy of *trans* state and orientation correlation function. The dynamics and crystallization were found to change according to energetic (monomer particle energetic interaction) effects.

Introduction: There has been much attention paid recently to the enhanced properties of polymers containing nanosized filler particles. Many experimental studies have shown improved material properties of polymer nanocomposites over those of the neat polymer. When a small volume fraction of spherical nanoparticles was added to a semicrystalline polyethylene (PE), for example, the tensile strength increased up to 30%, and the tensile modulus nearly doubled in comparison to a structurally similar semicrystalline neat PE. The range of volume fractions of nanosized filler particles giving rise to reinforcement was found to be from less than 1% to ~10% much smaller than normally used in traditional polymer composites, where the fillers have dimensions on the order of micrometers. The nature of the polymer-filler particle interface defines to a large extent the reinforcement and the viscoelastic properties of the nanocomposites. The interface can be controlled by adjusting the chemistry of the filler surface.

This paper investigates the structure, dynamics and crystallization of an amorphous PE melt containing spherical nanoparticles. Several questions are addressed: (i) Is the static chain structure different in the nanocomposite compared to the neat, and on what length scale is the difference seen? (ii) How does the monomer-particle interaction control the dynamics and crystallization of PE chains? (iii) To what extent do the results obtained with this polymer specific model differ from those obtained with bead-spring models?

Materials and Methods: The simulations performed in this study used a coarse-grained rotational isomeric state (RIS) model for the PE chains composed of *n*-tetracontane (C₄₀H₈₂) where the chains were represented on a high coordination lattice. The simulations were performed at a temperature of 473 K, which is above the melting point of PE used in this simulation. The systems represent bulk material with nanosized fillers homogeneously dispersed. In most simulations, one filler particle per

simulation cell was considered. The filler structure represented a close packing of spherical fillers in space. The space occupied by the polymer was filled to a density of $\sim 0.76 \text{ g/cm}^3$, as appropriate for PE melt at 473 K. The simulation method employed the Metropolis Monte Carlo algorithm, which effectively samples the conformational space, for the coarse-grained model of PE chain on a second-nearest-neighbor diamond (SNND) lattice. The RIS model was incorporated into the simulation to calculate the short-range intramolecular conformational potential energy of the chain. The long-range intramolecular and intermolecular interaction potential energies were calculated using a lattice based approximation of the Lennard-Jones potential between monomers and between monomers and filler particle beads. The cutoff radius of the long-range energy was three lattice units (each lattice unit is $\sim 0.25 \text{ nm}$). Spherical nanoparticles were added to the system by creating a volume of beads on the SNND lattice structure that were uniquely specified as being of filler type. These sites were not accessible to the polymers. The fillers were fixed in space during simulation. The wall-to-wall distance, d , which was defined as the smallest distance between two points located on the surface of two neighboring fillers, was fixed at $1.83R_g$. The energetic interaction $u(r)$ between polymer beads and particle beads was defined using the same Lennard-Jones potential as was used for the polymer to polymer interactions except it was multiplied by a prefactor ω . In this study ω was taken to be 0.1, 1.0, and 2.0 in separate simulations, representing repulsive, neutral, and attractive interactions, respectively. Each system was equilibrated for at least 10 million Monte Carlo steps (MCS); then production runs of 10 million MCS were performed. For crystallization studies, the temperature was instantaneously dropped to 298 K, and the simulation was continued at 298 K. At least 10 million MCS was needed to observe the crystallization.

Results and Discussion:

Structures and dynamics: The equilibrium structure of PE nanocomposite model is illustrated in Figure 1. The static chain structure of PE nanocomposites was investigated by examining the following three chain measures-average size, average shape, and average chain orientation-between the composite systems and the comparable neat system. For all three measures no significant variation was observed between values found for the composite systems and those found for the neat system. In addition, no significant variations were found in these measures as a function of distance from the particle for all composite systems investigated. However, when the structure of bridge segments was examined in detail, it was found that they became more stretched relative to the neat chain segments containing the same number of monomers. The system with the largest wall-to-wall distance between particles had bridge chain segments that were $\sim 40\%$ more stretched when compared to chain segments that contain the same number of monomers in the neat system. The amount of stretch in a bridge segment appeared to decrease as the wall-to-wall distance decreased. The dynamics of the PE chain was found to be different in the composite systems compared to the neat PE. The Rouse relaxation time, τ_p , of the entire chain increased rather suddenly as the separation decreased below $\sim 1.5R_g$. In addition, τ_p also increased for systems with attractive monomer-particle interaction energy compared to the systems with neutral and repulsive interactions. The most notable observation was the slowing down in the Rouse dynamics seen on all subsections of

the chain no matter how small the subsections were, meaning that on average every monomer feels the confinement of the neighboring particles, slowing the relaxation of every chain subsection.

Bond Conformation: In order to investigate the structure formation process on the molecular level, we first examine how the conformational change takes place. The RIS model for the unperturbed PE chain predicts that 58 % and 64 % of the bonds are in the *trans* state at 473 and 298 K, respectively. Figure 2 depicts an evolution of the fraction of the bonds in *trans* states as a function of MCS after an instantaneous quench from 473 to 298 K. As the simulation of the nanocomposite proceeds, the chains adopt more *trans* conformation. After 10 million MCS, the fraction of the bonds in the *trans* states approaches a limiting value about 70-80 %. This value is smaller than that of the crystallization in the bulk (ca. 85 %) by the same MC method. Therefore, chains adopt more *gauche* conformation for the crystallization in the nanocomposite. The attractive surface causes chain to adopt more *gauche* conformation compared to the repulsive and neutral surface. Repulsive surface was found to enhance the rate of conformation changes to *trans* during the initial stage of structure formation. However, the *trans* fraction is about the same amount as from the neutral system.

Chain Ordering: A PE chain has zigzag *trans* conformation (torsion angle 180° at the internal C–C bonds) when it crystallizes. In a perfect crystalline domain, bonds have high correlation even at long distance. In order to investigate the growth process of an intermolecular orientational order, we calculate the global orientation correlation function, S_G , which is defined by Equation (1).

$$S_G = \frac{1}{2} [3 \langle \cos^2 \psi \rangle - 1] \quad (1)$$

Here, ψ denotes the angle between the main axes of two chains, and the value of S_G is averaged for all pairs of chains in a given snapshot. The main axis of a chain is the longest principal axis of the radius of gyration tensor. This parameter, S_G , has a value of 1.0 when all chains are parallel and that of 0.0 when all chains are randomly oriented. Figure 3 depicts the global orientation order parameter, S_G , as a function of MCS. S_G increases steadily at the beginning of the crystallization, except the case for the attractive wall, followed by an almost constant value in the late stage. The chains finally achieve $S_G \sim 0.1$ which is substantially smaller than the crystallization in the bulk simulation without nanofiller ($S_G \sim 0.8$). This result suggests that chains in the nanocomposite are less ordered compared to the crystallization in the bulk. By comparing Figure 3 with Figure 2, it is concluded that the ordering of molecules correlates with the chain stretching. These results are slightly different from the previous simulation for the bulk system in which the ordering of chains starts after the chains are stretched to a certain extent. The difference might be induced by the crystallization in different domains with various orientations in the present case.

Bond ordering: The order parameter of all coarse-grained bonds, S_b , are defined in a similar manner of the chain ordering by changing the angle between the main axes of two chains (ψ) in Equation 1 to the angle between the chords (θ). Figure 4 depicts the evolution of this parameter when the structure at 473 K is instantaneously dropped to 298 K. As the simulation proceeds at 298 K, this parameter increases from its value at 473 K and eventually reaches new equilibrium values at 298 K. For S_b , the final value is in the range from 0.1 to 0.3, indicating the nanocomposite at 298 K has reached a state in which coarse-grained bond vectors are changed from randomly oriented to a more ordered structure. These results are in accord with the stretching of chain as seen in an increase in the fraction of *trans* shown in Figure 2. S_b increases steadily for the neutral and attractive wall system while it reaches a plateau for the repulsive wall case. The magnitude of S_b is also different and can be ordered as:

$$S_{b, \text{repulsive}} > S_{b, \text{neutral}} > S_{b, \text{attractive}}.$$

Conclusions: The structures, dynamics and crystallization of PE nanocomposites composed of *n*-tetracontane ($C_{40}H_{82}$) mixed with a neutral, attraction and repulsion spherical nanofiller has been investigated by a dynamic Monte Carlo method on a high coordination lattice. The various chain structures and dynamics changed slightly with the monomer-particle interaction. After a deep quench to lower temperature from the melt, the nanocomposite adopts a configuration dominated by extended chains. The packing and ordering of chains in the vicinity of the surface can be increase or decrease than portions of the nanocomposite located further from the surface depending on the nature of interfacial interaction.

Acknowledgements: This project was supported by National Synchrotron Research Center (2-2548/PS02), National Nanotechnology Center (NN-B-22-m1-20-47-06) and Suranaree University of Technology.

References:

1. DIONNE, P. J., OZISIK, R., and PICU, C. R. (2005). **Macromolecules** 38: 9351-9358.
2. DIONNE, P. J., OZISIK, R., and PICU, C. R. (2006). **Macromolecules** 39: 3089-3092.
3. VAO-SOONGNERN, V., OZISIK, R., and MATTICE, W. L. (2001). **Macromol. Theory. Simul.** 10: 553-653.
4. VAO-SOONGNERN, V., XU, G., and MATTICE, W. L. (2004). **Macromol. Theory. Simul.** 13: 539-549.

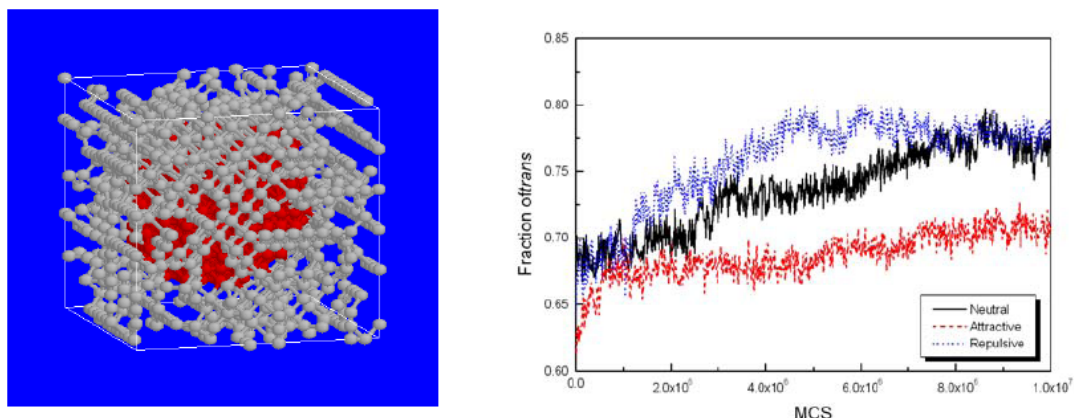


Figure 1 Snapshot of the final conformation of a typical nanocomposite at 298 K depicted using all carbon atoms. Red color particle denotes the spherical nanofiller used in this simulation.

Figure 2 Fraction of C-C bonds that are in the *trans* state as a function of MCS after an instantaneous cooling of nanocomposite from 473 to 298 K.

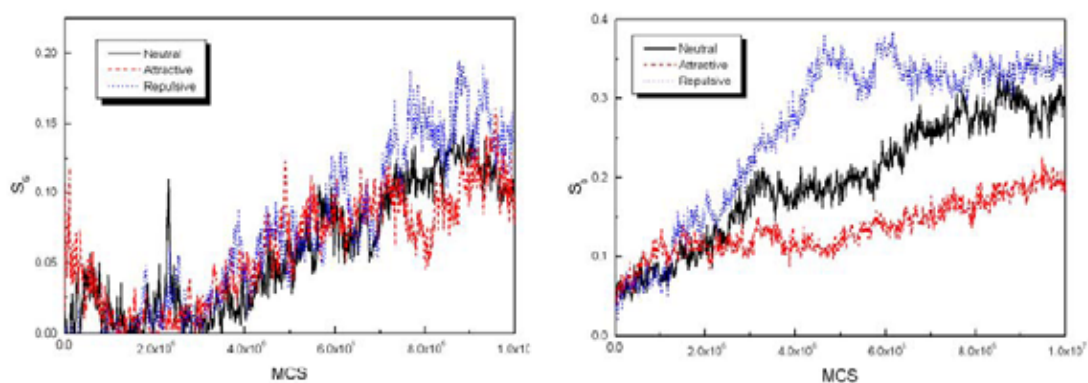


Figure 3 The global orientation order parameter, S_G , as a function of MCS after an instantaneous cooling of the nanocomposites from 473 to 298 K.

Figure 4 The bond orientation order parameter, S_b , as a function of MCS after an instantaneous cooling of the nanocomposites from 473 to 298 K.

การจำลองพลีเอทรีนออกไซด์-ไทเทเนียมไดออกไซด์นาโนคอมโพสิตโดยเทคนิค

โมเลกูลาร์ไดนามิกส์

MOLECULAR DYNAMICS SIMULATION OF POLY(ETHYLENE OXIDE)- TITANIUM DIOXIDE NANOCOMPOSITE

พรทิพย์ สีมา, วิศิษฐ์ แวสูงเนิน*

Porntip Seema, Visit Vao-soongnern*

* School of Chemistry, Institute of Science, Suranaree University of Technology,
Nakhon Ratchasima, 30000. Email: visit@sut.ac.th

บทคัดย่อ: ได้นำเทคนิคโมเลกูลาร์ไดนามิกส์ (MD) มาศึกษาระบบนาโนคอมโพสิตซึ่งประกอบด้วยพอลิเอทรีนออกไซด์ (PEO) และไทเทเนียมไดออกไซด์ (TiO_2) ที่ 300 เคลวินโดยใช้ Universal forcefield ระบบพื้นผิว PEO/ TiO_2 ที่สร้างจากระนาบ (110) anatase TiO_2 นี้จะนำเป็นแบบจำลองของระบบพอลิเมอร์อิเล็กโทรไลต์แบบของแข็งที่ใช้ในเซลล์แสงอาทิตย์แบบไวต่อสีข้อม จากการจำลอง MD พบว่าพื้นผิวอิสระและ TiO_2 มีผลต่อความหนาแน่นของ PEO โดยเกิดการเรียงตัวโมเลกุลเป็นชั้นจากพื้นผิว TiO_2 ประมาณ 15 Å สำหรับพื้นผิวอิสระนั้นจะมีความหนาแน่นของ PEO ต่ำกว่าและมีความหนาแน่นของพื้นผิวมากกว่า (ประมาณ 20 Å) สมบัติพลวัตเชิงโครงสร้างและโครงสร้างที่บริเวณรอยต่อกับ TiO_2 พบว่าช้าลงเมื่อเทียบกับ PEO ปกติ แต่จะมีการเคลื่อนที่เร็วมากขึ้นหากเป็นพื้นผิวอิสระ

Abstract: Molecular Dynamics (MD) simulation studies of the free surface of poly(ethylene oxide) (PEO) and the interface between PEO and TiO_2 nanocomposites have been performed at 300 K using Universal forcefield. The PEO/ TiO_2 interface with (110) anatase TiO_2 surface was chosen as a model for solid polymer electrolytes used in dyed-sensitized solar cells. MD simulations revealed that the PEO density is significantly perturbed by TiO_2 interface and free surface, forming layers of highly dense polymer (compared to the bulk melt) that persisted up to 15 Å from the TiO_2 interface. At the free surface region, the PEO density is lower and the interfacial profile becomes broader (*ca.* 20 Å). Conformational and structural relaxations of the interfacial PEO were found to be dramatically slower than those of bulk PEO. In contrast, these relaxations were found to be enhanced at the free surface region.

Introduction: Understanding the interface between polymer melts and solids is of fundamental importance in all practical applications where the properties of interest of polymer-based materials are primarily regulated by the presence of solid components. This is the case, for instance, of industrially important systems such as polymer nanocomposites. Therefore, the polymer/solid interface has been the subject of several simulation studies in recent years. Molecular simulations provide an excellent opportunity to directly study the influence of nanoparticles on structure and dynamics

of polymers, since detailed information on the properties near a nanoparticle surface is difficult to obtain experimentally. Monte Carlo (MC) and Molecular Dynamics (MD) simulations performed for various model polymers near planar solid surfaces indicate that molecular arrangements, conformations and dynamics of the polymer are strongly perturbed with respect to the isotropic bulk. The strength of the nanoparticle-polymer interaction and the nanoparticle specific surface area were found to be the most important factors controlling the properties of the interfacial polymer. The addition of nanoparticles with attractive interactions led to decreased polymer dynamics and increased viscosity, whereas the addition of nanoparticles with the repulsive, or excluded volume, interactions led to increased polymer dynamics and decreased viscosity. These effects were found to scale linearly with the specific surface area of nanoparticles.

In this work, we are interested in understanding the influence of the effect of the TiO₂ interface and free surface on PEO structural, conformational, and dynamic properties. The PEO/TiO₂ system has been chosen because PEO is a major component of PEO-based solid polymer electrolytes, which are potential candidates for use in solvent-free dye sensitized solar cell. The addition of ceramic nanoparticles to polymer electrolytes, initially done to enhance mechanical properties, has also been found to improve the anodic stability, cyclability, sometimes conductivity, and cation transfer number of polymer electrolytes without causing any observed degradations. A fundamental understanding of the mechanisms responsible for the dramatic changes in polymer electrolyte properties with the addition of nanoparticles is lacking. This MD simulation study of the PEO/TiO₂ system is the initial step toward understanding more complicated PEO/TiO₂/KI/I₂ systems.

Simulation Method: MD simulations of pure PEO and PEO attached TiO₂ surface, as shown in Figure 1, have been performed. Ten PEO chains with the structure of H-(CH₂-O-CH₂)₅₄-H were used in the simulations. A Universal force field was used to describe PEO-PEO and PEO-TiO₂ interactions. Each TiO₂ surface comprises four atomic planes or layers of 240 Ti and 480 O from the (110) direction of an anatase crystal that is about 10 Å thick and 28.5, 26.7 and 127.0 Å in the *x*, *y* and *z* dimensions, respectively. The TiO₂ surfaces were placed symmetrically with respect to the bottom of the box as shown in Figure 1. All MD simulations were performed at 300 K using a Forcite module in Materials Studio 4.1 simulations package. A Nose-Hoover thermostat were used to control the temperature, and bond lengths were constrained using the Shake algorithm. The particle-mesh Ewald (PME) technique was used to treat Coulomb interactions.

Results, Discussion, and Conclusion:

Structure and Conformation: Figure 1 shows the atomistic molecular model of PEO/TiO₂ interface and PEO free surface. Figure 2 represents the total density profiles of all atoms in the model. TiO₂ layer is on the left hand side. The density profile near TiO₂ surface is sharper compared to the free surface. Layering of PEO is clearly seen in the first 1.5 nm where the density profile becomes oscillating pattern. Hence, the chain segments in contact with the surfaces are arranged in densely packed and ordered layers, and this perturbation of density and order extends into the liquid two or three times the transverse diameter of the chains. The width of PEO density

profile at the free surface region extends almost 2 nm. The chain conformation is perturbed to a scale length on the order of the root-mean-square (rms) radius of gyration of the polymer, and chains with center of mass at a distance from the surface less than the unperturbed rms radius of gyration are flattened against the planar surfaces like pancakes and present a substantial fraction of trains of units running in the first densely packed layer.

Interaction energy: The interaction energy can be calculated by using the following equation.

$$E_{\text{Interaction}} = E_{\text{total}} - (E_{\text{surface}} + E_{\text{polymer}})$$

Where E_{total} is the energy of the surface and the polymer, E_{surface} is the energy of the surface without the polymer and E_{polymer} is the energy of the polymer without the surface. To get the value for E_{polymer} and E_{surface} , the single point energy of the polymer and TiO_2 surface in the 3D lattice but without contributions from the surface are calculated. $E_{\text{total}} = -652.80$ kcal/mol, $E_{\text{surface}} = -4412.26$ kcal/mol and $E_{\text{polymer}} = 3819.86$ kcal/mol, gives $E_{\text{Interaction}} = -60.39$ kcal/mol which indicate strong interaction between PEO and TiO_2 surface.

Dynamics: To examine the influence of TiO_2 surfaces on PEO translational dynamics, the mean-square displacements (MSD) of the PEO backbone atoms in a plane parallel to the TiO_2 surfaces were calculated. PEO backbone atoms in the layer adjacent to TiO_2 surfaces were significantly slower than those in bulk PEO. The component of MSD perpendicular to the surfaces is also substantially smaller for chains in contact with the surfaces than for bulk chains indicating that interaction between PEO and TiO_2 cause a slow down of chain dynamics at the interface region. In stead, for free surface, the PEO dynamics are found to increase due to a drop in local density at the surface region.

Acknowledgements: This project is supported by National Synchrotron Research Center (2-2548/PS02) and Computational Nanotechnology Consortium (CNC).

References:

- (1) Porntip Seema, Supagorn Rugmai, Wantana Klysubun, V. Vao-soongnern, STT32, (2006)
- (2) Porntip Seema, Rahmi Ozisik, V. Vao-soongnern, ICMAT, (2007)
- (3) Porntip Seema, Rahmi Ozisik, V. Vao-soongnern, AWPP, (2006)
- (4) Borodin, O., Smith, G. D., Bandyopadhyaya, R., and Bytner, O. (2003). *Macromolecules* 36: 7873-7883.

Keywords: Poly(ethylene oxide) (PEO), Titanium dioxide, polymer nanocomposites, Molecular Dynamic simulation.

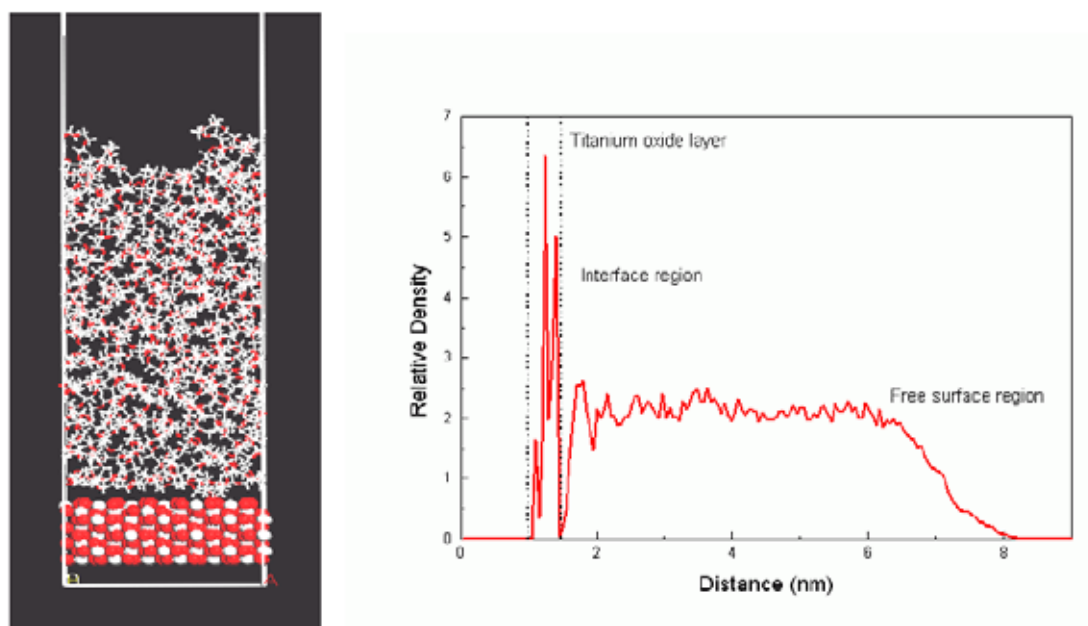


Figure 1 Snapshots of PEO attached one side to TiO₂ surfaces and another side to vacuum from NVT-MD simulations at 300 K.

Figure 2 PEO density profile from TiO₂ interface to free surface. Vertical dashed lines indicate the position of TiO₂ interfacial layers.

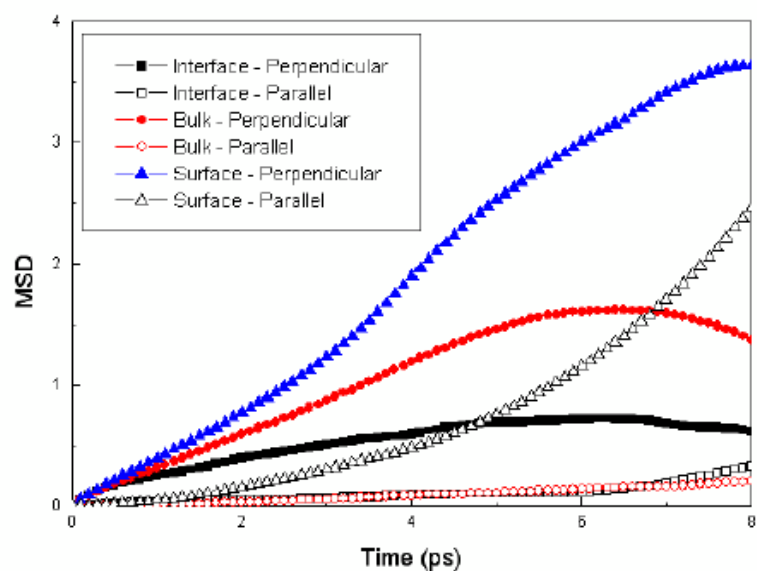


Figure 3 Mean square displacement (MSD) of PEO in parallel and perpendicular direction for three regions *i.e.* interface, bulk and free surface.

การจำลองระดับโมเลกุลและการวัดการดูดกลืนรังสีเอ็กซ์ของไอออนโพแทสเซียมและ
ไอออนไอโอดีนในน้ำ

MOLECULAR SIMULATION ANALYSIS AND X-RAY ABSORPTION
MEASUREMENT OF K^+ AND I^- IONS IN AQUEOUS SOLUTION

พรทิพย์ สีมา, วิศิษฐ์ แวสูงเนิน*

Porntip Seema, Visit Vao-soongnern*

* School of Chemistry, Institute of Science, Suranaree University of Technology,
Nakhon Ratchasima, 30000. Email: visit@sut.ac.th

บทคัดย่อ: ได้นำเทคนิคโมเลกุลาร์ไดนามิกส์ (MD) และ EXAFS มาศึกษาไอออนโพแทสเซียมและไอออนไอโอดีนที่มีโมเลกุลน้ำล้อมรอบ ระบบไอออนในน้ำ (K^+/H_2O , I^-/H_2O) นี้ใช้เป็นระบบอย่างง่ายของระบบไอออนในพอลิเมอร์ที่ใช้เป็นพอลิเมอร์อิเล็กโทรไลต์แบบของแข็งในเซลล์แสงอาทิตย์แบบไวต่อสีข้อม Radial distribution functions ที่คำนวณได้จาก MD ที่ 300 เคลวินโดยใช้ COMPASS forcefield ให้ข้อมูลเชิงโครงสร้างได้แก่ ระยะเฉลี่ยระหว่างไอออนและอะตอมของน้ำ จำนวนอะตอมของน้ำ (N_O , N_H แทนจำนวนออกซิเจนและไฮโดรเจนตามลำดับ) ในชั้นแรกที่ล้อมรอบไอออน สำหรับระบบ K^+/H_2O พบว่าระยะเฉลี่ย K^+-O และ N_O คือ 2.65Å และ 6.4 ตามลำดับ สำหรับระบบ I^-/H_2O พบว่าระยะเฉลี่ย I^-O , I^-H , N_O และ N_H คือ 3.55Å, 2.55Å, 6.9 และ 6.4 ตามลำดับ ผลลัพธ์ที่ได้นี้สอดคล้องกับผลที่มีรายงานไว้แล้ว ใช้วิธีของอะตอมใน MD (MD trajectories) รวมกับการจำลองการกระเจิงของอิเล็กตรอน (electron scattering simulation) สร้างสเปกตรัม EXAFS สเปกตรัมที่ได้จาก MD สอดคล้องกับสเปกตรัมที่ได้จากการทดลอง อย่างไรก็ตามมีข้อสังเกตว่าอะตอมไฮโดรเจนมีผลต่อสัญญาณ EXAFS นั่นคือการคำนวณสเปกตรัม EXAFS โดยไม่รวมไฮโดรเจนเข้าไปในระบบ K^+/H_2O แต่รวมไฮโดรเจนเข้าไปในระบบ I^-/H_2O จะให้สเปกตรัม EXAFS ที่ใกล้เคียงกับการทดลองมากกว่า

Abstract: Molecular Dynamics (MD) simulation and extended X-ray absorption fine structure (EXAFS) spectroscopy were combined to determine the solvation structures of K^+/H_2O and Γ/H_2O systems which are the simplified models of ion/polymer systems for solid polymer electrolytes used in dye-sensitized solar cells. The radial distribution functions (RDFs) calculated from MD simulations with COMPASS forcefield at 300 K provided the structural parameters: the ion–water atom distances and the coordination numbers of neighboring water atoms (N_O and N_H are the numbers of oxygen atoms and hydrogen atoms, respectively). For the K^+/H_2O system, the average $K^+–O$ distance and N_O for the first coordination shell are 2.65 Å and 6.4, respectively. For the Γ/H_2O system, the average $\Gamma–O$ and $\Gamma–H$ distances, N_O , and N_H are 3.55 Å, 2.55 Å, 6.9, and 6.4, respectively. These results are in very good agreement with the literature data. MD trajectories were coupled to electron scattering simulations to generate MD-EXAFS spectra which were then compared with the measured spectra. Comparison shows the consistence between the EXAFS spectra from MD simulations and those from the experiments. However, it should be noted that hydrogen atoms can affect on the MD-EXAFS signals. Excluding all hydrogen atoms in the calculations for the K^+/H_2O system whereas including them in the calculations for the Γ/H_2O system gave the better MD-EXAFS spectra as compared to the measured spectra.

CURRICULUM VITAE

PORNTIP SEEMA

Born: April 15, 1983, Roi-Et

Citizenship: Thailand

Education:

2002 – 2005 B. Sc. Chemistry (First Class Honors)

Khon Kaen University, Khon Kaen, Thailand

Presentation:

1. Poster presentation at 32nd Congress on Science and Technology of Thailand, 10 – 12 October 2006, Queen Sirikit National Convention Center, Bangkok, Thailand.
2. Poster presentation at Asian Workshop on Polymer Processing (AWPP), 6 – 8 December 2006, Rama Gardens Hotel, Bangkok, Thailand.
3. Oral presentation at 33rd Congress on Science and Technology of Thailand, 18 – 20 October 2007, Walailak University, Nakhon Si Thammarat, Thailand.
4. Oral presentation at 34th Congress on Science and Technology of Thailand, 31 October – 2 November 2008, Queen Sirikit National Convention Center, Bangkok, Thailand.